Electromigration in Bamboo Aluminum Interconnects

Von der Fakultät Chemie der Universität Stuttgart
zur Erlangung der Würde eines Doktors der Naturwissenschaften
(Dr. rer. nat.) genehmigte Abhandlung

vorgelegt von

Christian Witt

aus Hamburg

Hauptberichter: Prof. Dr. phil. E. Arzt
Mitberichter: Prof. Dr. rer. nat. F. Aldinger
Tag der mündlichen Prüfung: 20. Dezember 2000

Max-Planck-Institut für Metallforschung und
Institut für Metallkunde der Universität Stuttgart

2000

Christian Witt

Electromigration in Bamboo Aluminum Interconnects

144 pages, 92 figures, 6 tables

Abstract

Electromigration is a serious threat to the reliability of metallic interconnects in microelectronic circuits. It can create damage in the form of voids and hillocks. The addition of a small percentage (0.5-4.0 wt%) of copper to Al interconnects, and the encapsulation with a dielectric passivation layer improve the electromigration lifetime. However, the mechanisms by which these improvements occur are not entirely understood. The focus of this work is to better understand the passivation and the Cu effect on electromigration in Al interconnects with a bamboo microstructure. For this purpose, experimental investigations are performed on 0.5 μm wide Al segments of various lengths made from pure Al and Al(0.5 wt% Cu), both passivated and unpassivated.

The results show that the addition of Cu increases the threshold product of segment length and current density above which damage occurs. Whereas hillocks form directly at the anode end in pure Al segments, they form some distance from the end in Al(Cu) segments. In contrast to pure Al segments, the electromigration-induced Al displacement in Al(Cu) segments shows an increasing rate (drift velocity). These observations are consistent with the idea that the Al mobility is substantially reduced if the Cu concentration is large enough. The electromigration-induced motion of Cu is studied in detail in undamaged segments. The dissolution of Al_2Cu precipitates is consistent with the picture that Cu is transported rapidly along the interfaces, such that diffusion into the Al lattice becomes rate controlling. In addition, it is shown that the formation of precipitates requires a supersaturation of roughly two times the equilibrium solubility.

The statistical distribution of threshold products is investigated as a function of segment length. For the first time, it is shown that the mean value is roughly constant, whereas the deviation increases with decreasing segment length. This is explained by the idea that the threshold stress for damage formation does not have a single value, but depends on the local microstructure and thus scatters around a mean value along the length of the interconnect. The comparison of passivated and unpassivated segments shows that the passivation increases the threshold product, but that the stress required to form a void is roughly the same. The drift velocity in passivated and unpassivated Al is also the same. This suggests that the increase in reliability by passivation of interconnects is due to the suppression of hillocks.

Max-Planck-Institut für Metallforschung, Institut für Metallforschung, Stuttgart 2000

Als Manuskript gedruckt. Printed in Germany.

Elektromigration in Bambus - Aluminium Leiterbahnen

Kurzzusammenfassung

Elektromigration in miniaturisierten Leiterbahnen stellt eine ernstzunehmende Bedrohung für die Zuverlässigkeit integrierter Schaltkreise dar. Sie kann zur Schädigung der Bahnen durch die Bildung von Poren und Hügeln führen. Die Lebensdauer von Aluminiumbahnen wird erheblich durch den Zusatz von Kupfer, und durch die Abdeckung mit einer Passivierungsschicht gesteigert. Die genauen Mechanismen dieser Effekte sind jedoch noch nicht vollständig verstanden. Um diese Effekte in Leiterbahnen mit einer Bambusstruktur zu untersuchen, wurden Elektromirationsexperimente an sub-Mikrometer schmalen Leiterbahnsegmenten verschiedener Länge aus Al und Al(0.5 gew% Cu), jeweils mit und ohne Passivierung durchgeführt.

Der Zusatz von Kupfer führt zu einer Erhöhung des kritischen Produkts von Segmentlänge und Stromdichte, oberhalb dessen eine Schädigung eintritt. Im Gegensatz zu Segmenten aus reinem Al, bilden sich die Hügel etwas entfernt vom Anodenende der Leiterbahnsegmente, und der Materialabtrag des Al als Funktion der Zeit (Driftgeschwindigkeit) nimmt in den Al(Cu) Bahnen zu. Diese Beobachtungen sind konsistent mit der Vorstellung, daß die Mobilität des Al erheblich reduziert wird, wenn die Kupferkonzentration genügend groß ist. Die Untersuchung der elektromigrationsinduzierten Umverteilung des Kupfers in unbeschädigten Segmenten zeigt, daß der Kupfertransport entlang der Grenzflächen der Leiterbahnen sehr schnell ist, so daß die Auflösung von Al_2Cu Ausscheidungen durch die Diffusion von Cu in das Al Gitter kontrolliert wird. Außerdem wird gezeigt, daß für die Bildung von Ausscheidungen eine Kupferübersättigung von etwa der zweifachen Löslichkeitskonzentration erforderlich ist.

Die statistische Verteilung des kritischen Produkts wird als Funktion der Segmentlänge untersucht. Erstmalig wird demonstriert, daß die Streuung mit abnehmender Länge ansteigt. Um dieses Verhalten zu erklären, wird ein Modell vorgestellt, das davon ausgeht, daß die kritische mechanische Spannung ab der sich eine Schädigung bildet, von der Mikrostruktur der Bahn abhängig ist. Der Vergleich von passiviertem und unpassiviertem Al zeigt, daß die kritischen Spannung zur Bildung von Poren und die Driftgeschwindigkeit in etwa gleich sind. Das kritische Produkt ist jedoch bei den passivierten Bahnen deutlich größer, was durch die Unterdrückung der Hügelbildung erklärt wird.

Preface

This work was conducted between June 1997 and December 2000 at the Institut für Metallforschung, University of Stuttgart, and the Max-Planck-Institut für Metallforschung in Stuttgart.

First, I would like to thank my adviser, Professor Eduard Arzt, for the opportunity to be one of his team. It has been a pleasure to work with him over the years.

I thank Professor Fritz Aldinger for refereeing the thesis.

This work would have been impossible without the strength, the experience, and the creativity of my supervisor, Dr. Cynthia A. Volkert.

I thank Dave Barr and Walter Brown from Bell Labs, Lucent Technol., Murray Hill NJ, for providing the pure Al samples.

Finally, I would like to thank the department members. The group has been a constant source of advice, encouragement, and fun.

Contents

1

Introduction

Modern integrated circuits are extraordinarily complex devices, containing millions of transistors. These are the active units in electronic circuits utilized to perform signal amplification, logic operations and the like. In order to function properly or to communicate with the outside world, these devices must be connected in the appropriate fashion. This is accomplished with metal wires which are called interconnects. Recent devices contain interconnects with cross-sections of dimensions smaller than a few tenths of a micron and with a total length of roughly one kilometer in a total area not larger than a postage stamp. The successful fabrication of a modern microprocessor requires several hundred processing steps with a placement precision greater than a micrometer. For these devices to be commercially feasible, they must be manufactured in a manner which gives a high yield and operate for years without failure. Because it is not practical to repair such a monolithic microelectronic circuit, failure of such a device imposes a loss equal to the cost of the unit. Malfunction of the entire device is caused by failure of a relatively small number of interconnects. Therefore, high standards of reliability are required for each individual metal line.

In order to improve and insure the reliability of integrated circuits, the behavior and failure mechanisms of the constituent materials must be understood. The behavior of materials with dimensions typical in microelectronic devices generally differs from that which is observed in bulk form. As an example, the mechanical stresses present in thin metal films can be substantially higher than in bulk metals. Consequently, interconnect reliability has become a field of study in itself. This dissertation focuses on a particular failure mechanism in interconnects which is known as electromigration.

1.1 The interconnect

Interconnects are made by deposition and lithographic patterning of thin metal films, and are separated by insulating dielectric material. This dielectric layer is often called the *passivation*. In most modern interconnect designs, the conductor metal is surrounded by *barrier layers* which are typically made of Ti, TiN or Ta. These layers act as barriers to diffusion between the interconnect and the dielectric and are also able to shunt current in case the interconnect metal is interrupted, for example by voids. In order to allow dense packing of the electronic devices on the surface of the silicon substrate, several layers of interconnects must be fabricated. Advanced chips have evolved over the last 15 years from a single level of Al-based metallization to as many as six or seven levels. The vertical connections between the layers are achieved by so-called *vias*, created by etching small holes through the dielectric to the interconnect layer below and filling them with metal. When the next thin metal film is deposited, electrical contact is made through the via to the underlying metal layer. Figure 1.1 shows the cross-section of a recent microprocessor, the Advanced Micro Device's K6, where six layers of interconnects have been used.

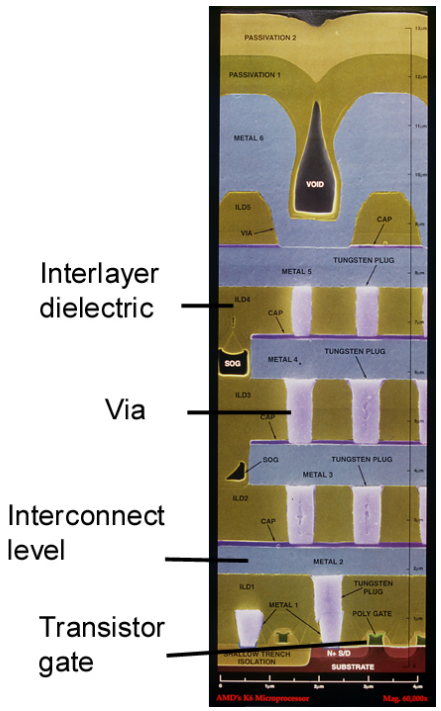

Figure 1.1: SEM cross-section of Advanced Micro Device's K6 microprocessor.

For the last 20-30 years, the metal of choice for interconnects was Al alloyed with a small percentage (0.5-4.0 wt%) of copper. Nowadays, metallization schemes are moving to copper as the conducting material. This is mainly due to lower production costs as well as to higher performance in terms of clock speed of the devices. The improved performance is attributed to the lower resistivity of copper, which reduces signal delay in the interconnects. However, Al and Al alloys offer good patternability, high conductivity, strong resistance to corrosion and good adherence to the substrate [Pramanik and Saxena, 1983], and are expected to be continued to be used in many applications.

1.2 Electromigration

Conduction electrons in a metal are scattered by lattice inhomogeneities, such as vacancies or displaced atoms. Atom displacement occurs during solid state diffusion by jump processes. In the process of making a diffusive jump, an atom must move between two lattice sites and scatters conduction electrons. Thermally activated atomic motion is usually a random process. There is no preference in the direction of atomic jumps, and a jump forward is equally probable as a jump backwards, regardless of how these directions are defined. This random walk is represented by the standard diffusion equation, Fick's law. However, when an electric current flows, scattering of electrons by the diffusing atom causes the diffusive jump to be biased in the direction of the electron flow. In this process, the conduction electrons transfer a part of their momentum to the jumping atom. This process exerts a driving force for diffusing atoms. This force is often called *electron wind force*. The wind force is very small compared to the energy barrier for the diffusive jump between lattice sites, but it becomes significant when many electron-ion interactions take place such as at high current densities. In an accurate treatment the electron scattering needs to be described quantum-mechanically [Sorbello et al., 1982].

The electric field also exerts a direct force on the positive metal ions in the conductor, counteracting the electron wind force. This force results from the electrostatic interaction between the ions and the external field. Theoretical attempts to calculate the direct force have not been very successful [van Eck and Lodder, 1994, Todorov et al., 2000]. It is generally believed that in most metals the atoms are screened by the electrons from the conduction band so that the direct force is quite small. The total driving force, the sum of the direct and wind forces, can be described

by an effective valence Z^*. Often, Z^* is called the effective charge number. The driving force for electromigration is given by

$$F = Z^* e \rho j \ , \tag{1.1}$$

where e, ρ, and j are the electron charge, the metal resistivity, and the current density. Using the Einstein relation for diffusion in a potential field, the flux of atoms due to the electromigration force is expressed as [Fiks, 1959, Huntington and Grone, 1961]

$$J = c\frac{D}{kT}Z^* e \rho j = cv \ , \tag{1.2}$$

where D is the effective diffusivity, kT is the product of Boltzmann's constant and the absolute temperature, c is the concentration of the migrating species. v is called the electromigration drift velocity.

1.3 Interconnect Reliability

To generate a perspective, the American National Technology Roadmap for Semiconductors (NTRS) for 1998 indicates that between 1998 and 2006, the minimum feature size in microelectronic devices will decrease from 250 nm to 50 nm. Over the same period, the total length of wiring on chips is expected to increase from 1 to over 5 km. To maintain the present level of interconnect reliability at the chip level, the number of failures in time (FIT) per meter of wiring will have to decrease by a factor of five. Achieving this goal is a challenging task for processing specialists as well as for reliability engineers. One of the major concerns for interconnect reliability is electromigration. High current densities on the order of 0.1 MA/cm^2 will be used in conductor lines in advanced microchips. Such high current densities are rarely used in conventional electrical appliances. A typical automotive fuse fails at a current density of 0.001 MA/cm^2.

It has been shown that damage occurs only if the electromigration-induced mass flux is locally disturbed by flux divergencies [Hummel, 1977]. Divergencies may be attributed to microstructural inhomogeneities, temperature gradients or changes in material such as at the end of interconnect segments. Flux divergencies can cause atom depletion and eventually void formation, or atom accumulation leading to the formation of extrusions, called hillocks. These processes often lead to resistance increases or short circuits between adjacent lines, imposing a threat to the reliability of the interconnects.

Traditionally, electromigration performance is characterized by measuring a median lifetime t_{50} of a population of similar interconnects. The lifetime is defined as the time to reach an intolerable resistance increase which compromises the performance of the interconnect. Since lifetimes are on the order of years, testing at conditions where devices are actually used, e.g. 100°C and current densities in the range of 10^5 A/cm^2, is impractical. Hence, testing is usually performed at highly accelerated conditions such as elevated temperatures and high current densities, typically 200-300 °C and 1-10 MA/cm^2. In order to use the measured lifetime to predict the lifetime at service conditions, extrapolation has to be used. In 1967, James Black published one of the first studies of accelerated electromigration failure in Al lines [Black, 1967]. In his work, he examined the time to failure as a function of temperature and current density. Black found that the median time to failure t_{50} of these lines could be fit with a function of the form:

$$t_{50} = \frac{A}{j^n} \exp\left(E_a/kT\right) \ , \tag{1.3}$$

where A is a constant, n is the current density exponent, and E_a is an activation energy. The equation is known as *Black's law*, and remains an important means of extrapolating lifetime data to service conditions. Experimentally, Black found the current density exponent to be $n = 2$. Other experiments have found n to range from 1 to more than 3, and the interpretation of this number is subject of continued debate [Shatzkes and Lloyd, 1986]. Exponents higher than 3 are usually attributed to effects of Joule heating.

Black's law provides a simple means of extrapolating t_{50} and is widely used by interconnect manufacturers. However, using this equation is problematic if there are changes in mechanism over the temperature range of extrapolation. Consequently, a single activation energy may not be appropriate to describe the process. The need for more accurate, physically based lifetime models has resulted in a large number of investigations over the last two decades. For example, additional terms to Black's equation have been proposed to include the effect of a critical current density below which no damage occurs [Arzt and Nix, 1991]. This effect will be discussed in more detail later in this thesis.

Lifetime tests on large populations of interconnects yield the statistical distribution of the time to failure. Given the large total number of interconnect segments in a device (on the order of 10^6), it is clear that the deviation of lifetimes has significant impact on the reliability of a device. In interconnects without barrier or shunt layer, failure

of the interconnect occurs as soon as a void forms which spans the line and causes an electrical open. For a given population of lines as in a device, the device fails as early as the *first* interconnect is damaged. Failure of lines with barrier layers must be defined by a certain resistance increase. In this case, the device fails by the interconnect with the *worst* damage. Since shunt material like TiN is not prone to electromigration damage, shunt layers effectively improve on electromigration reliability. TiN has a high resistivity compared to Al decreasing the performance of the interconnect for a given cross-section. Hence, a sandwich of TiN and Al represents the best compromise. In both cases, interconnects with and without barrier layers, it is important to measure the distribution of lifetimes.

1.4 Outline of this dissertation

Electromigration is not only a technologically relevant problem for interconnects in microelectronic circuits, it is also a challenging problem in materials science, because it depends on the diffusional transport properties, and the electrical and mechanical properties of the constituent materials. The presence of impurities complicates the problem tremendously. The combination of different metals for the interconnects and barrier layers with dielectric materials generates further complication. It is desirable to better understand the physical processes, which are important for damage formation and evolution during electromigration. While lifetime measurements are useful to assess the reliability of interconnects, direct observations provide more insight in the physical processes. In this dissertation, the electromigration-induced damage in narrow Al interconnects is studied quantitatively by direct observations. The purpose of this work is to elucidate the effect of Cu and of passivation.

The dissertation is divided into 6 chapters: in chapter 2, the literature relevant for this work is briefly reviewed. It is divided into a discussion of the electromigration transport mechanism in bamboo interconnects, the evolution of electromigration-induced stresses, and two sections on the effect of passivation layers and the effect of Cu. In chapter 3, the experimental details of sample fabrication, characterization methods, and electromigration testing are described. Finally, the different methods that were used to quantify electromigration-induced drift are discussed. In chapter 4 and 5, the experimental results are described and discussed in detail. Both chapters are divided into measurements of the electromigration threshold, measurements below the threshold, and a discussion of electromigration-induced damage above the threshold. A brief summary is given in chapter 6.

2

Review of literature

2.1 Electromigration transport mechanisms

This work is focused on electromigration in sub-micron wide interconnects. Sub-micron interconnects typically have a "bamboo" microstructure, where no continuous grain boundary paths lie along the length of the interconnect. Since grain boundaries are the dominant mass transport path in polycrystalline films of Al at the temperatures of interest [Frost and Ashby, 1982, p. 26], the exact microstructure of the interconnects has an impact on the effective transport properties.

2.1.1 Miniaturization

It has been observed that increasing the grain size leads to increased lifetimes [Black, 1967]. This effect was attributed to the elimination of grain boundary diffusion paths. Various studies have shown the importance of grain boundaries as fast paths for atomic diffusion and thus for electromigration [Attardo et al., 1971]. Electromigration testing of single crystal lines shows a greatly increased time to failure and activation energy of the failure process [d'Heurle and Ames, 1970, Joo and Thompson, 1997]. While fabricating single crystal lines is not practical in a production process, the continued shrinkage of interconnect width produces a natural reduction in the number of grain boundaries lying along the length of the line. Because line thicknesses and grain sizes change little during miniaturization, decreasing the linewidth causes a transition from a polycrystalline to a "bamboo" microstructure [Walton et al., 1992]. Figure 2.1 shows how this transition occurs.

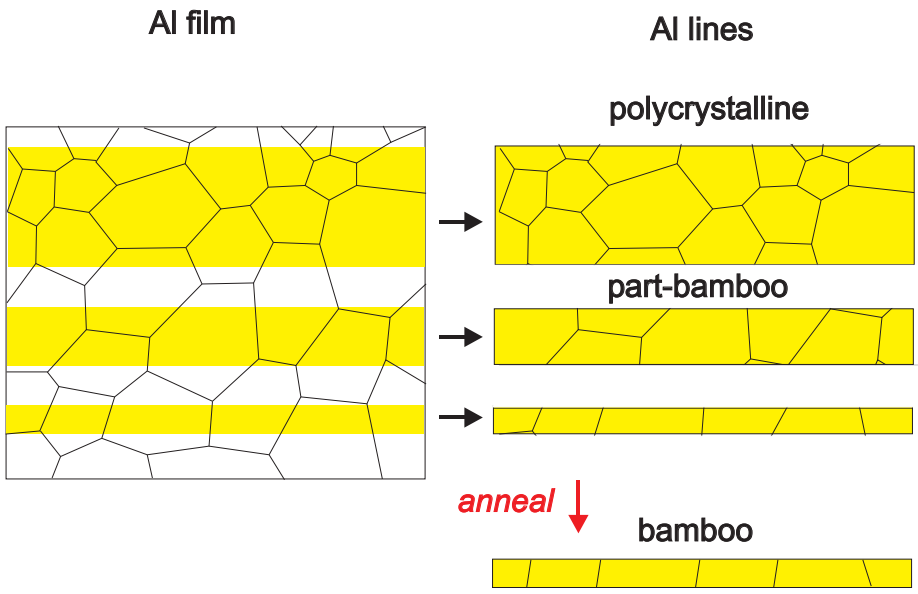

Figure 2.1: Microstructure of Al interconnects: due to continued miniaturization the microstructure of interconnects converts to a bamboo structure when the linewidth becomes smaller than the grain size.

To show the effect of the microstructure, a number of drift velocities was compiled from the literature, as shown in Figure 2.2. The electromigration-induced drift velocity (equation 1.2) is a measure of the transport properties of an interconnect. It can be determined from measurements of the displacement of the cathode edge of a metal segment placed on a barrier layer such as TiN [Blech and Kinsbron, 1975]. This method is described in more detail below. Figure 2.2 includes thin-film data for Al and Al alloys with near-bamboo and polycrystalline microstructures as well as bulk data. Although the drift velocities vary widely, they indicate that particularly at low temperatures, drift in polycrystalline interconnects is much more rapid than in bamboo interconnects. The polycrystalline data shows more scatter, probably due to differences in grain size. The dominant mode of electromigration in bamboo microstructures is contentious. While Oates presented experimental data which indicates that transport occurs via the Al lattice [Oates, 1996a], Hu and co-workers suggested that the interface between the Al and the surrounding dielectric is the primary pathway for transport [Hu et al., 1993a]. The latter authors investigated Al(0.3 wt%Pd 0.3 wt%Nb) lines with linewidths ranging from 0.85 to 2.4 μm. They discovered by SEM observation that material is depleted at the edges of the lines. Their conclusion was that the failure is dominated by interfacial diffusion along the edges. It is worth mentioning that all measurements on the bamboo lines shown in Figure 2.2 were performed on lines containing Cu. The addition of alloying elements such as Cu can lead to a significant change in the drift velocity [Spolenak et al., 1998b].

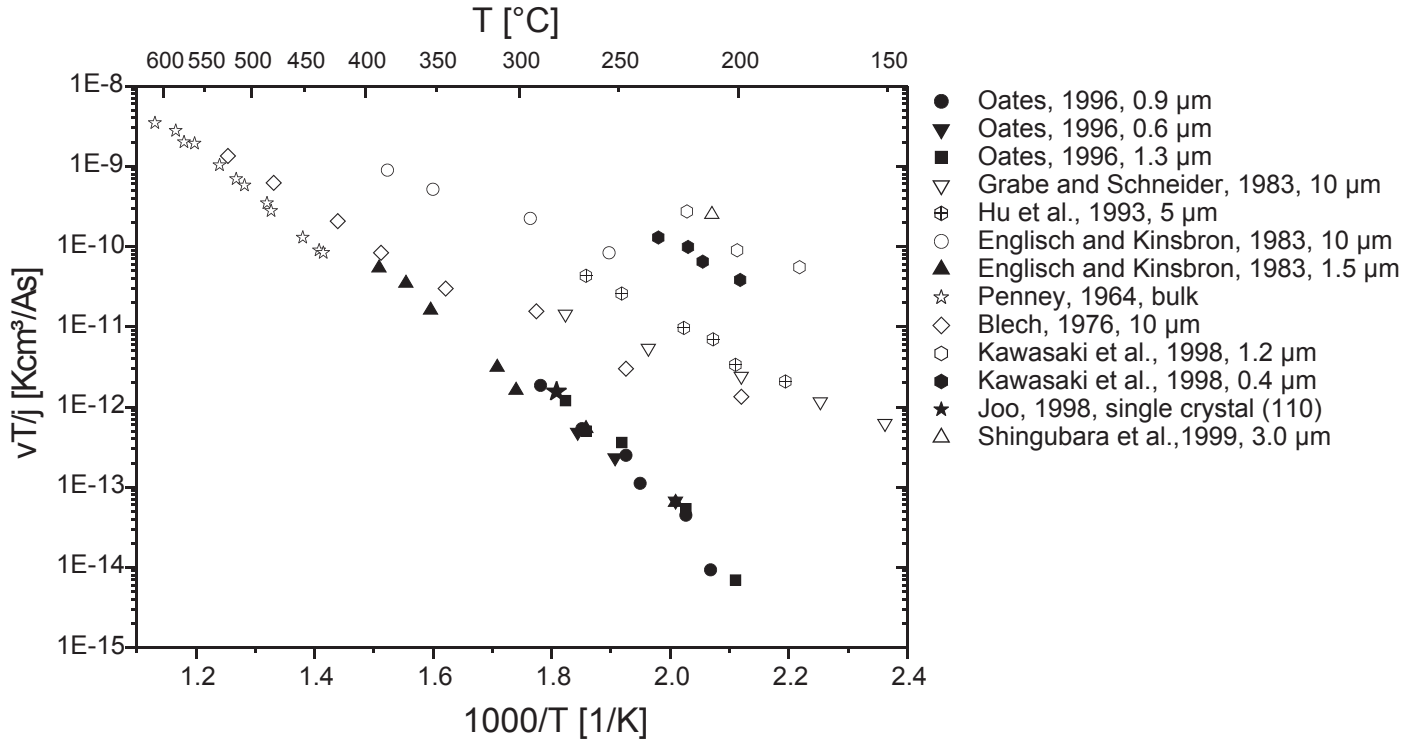

Figure 2.2: Compilation of normalized drift velocities from the literature after [Oates, 1996a]. Filled symbols refer to bamboo, open symbols to polycrystalline lines. Linewidths are listed in the legend. The alloys used are listed in table 2.1.

Reference	Alloy	Linewidth [μm]	E_a [eV]
[Grabe and Schreiber, 1983]	Al/TiN	10	0.49
[Hu et al., 1993a]	Al-3%Si-2%Cu/W	5	0.68
[English and Kinsbron, 1983]	Al-0.5%Cu/TiN	10	0.53
[Blech, 1976]	Al/TiN	10	0.55
[Penney, 1964]	Al	bulk	1.16
[English and Kinsbron, 1983]	Al-0.5%Cu/TiN	1.5	1.17
[Oates, 1996b]	Al-0.75%Si-0.5%Cu/TiN	0.6, 0.9, 1.3	1.26
[Kawasaki et al., 1998]	Ti/TiN/Al-1%Cu/TiN	0.4, 1.2	0.73
[Joo et al., 1998]	Al(110)/SiO_2	1.9	-

Table 2.1: Details and references for the thin film and bulk Al drift velocities shown in Figure 2.2.

2.1.2 Transport mechanisms in bamboo interconnects

In interconnects with a bamboo microstructure other transport paths than grain boundaries must be operating. Besides grain boundaries and the lattice, diffusion can occur via dislocation cores (pipe diffusion), or along the interfaces of the conductor. In typical Al interconnects, the Al has interfaces to the barrier layer metal, such as TiN, above and below, and interfaces with an insulator, such as SiO_2, at the sides. Interface diffusion is of considerable technological interest, since miniaturization increases the area of interconnect interfaces relative to the volume. To account for the various diffusion paths, an effective diffusion coefficient can be used which is expressed by

$$\bar{D} = D_l + \frac{2\delta_i D_s}{w} + \frac{2\delta_i D_i}{t} + A_d \rho_d D_d \ , \tag{2.1}$$

where D_l is the lattice diffusivity, D_s is the diffusivity along the interface between the Al and the surrounding dielectric (or sidewalls) [Oates, 1996b]. D_i is the diffusivity along the Al/barrier layer interface, with w and t being the conductor width and thickness. δ_i is the width of the interfacial diffusion path ($\approx 10\,\text{Å}$), A_d is the cross-sectional area of dislocations, and ρ_d is the density of dislocations aligned in the current direction. D_d is the diffusivity along dislocation cores. From equation 2.1 it can be seen that $\bar{D}$ and hence the electromigration flux (equation 1.2) depends on the conductor geometry if a significant proportion of the flux occurs by interfacial diffusion.

Diffusion data is available for the lattice diffusivity in pure Al, although there is some dispute about the precise value of D_l. A widely cited value measured by Peterson and Rothman, 1970, is $D_l = 0.11 \cdot 10^{-4} \exp(-1.26\,\text{eV}/kT)\,\text{m}^2/\text{s}$ over the range of 85-600°C. Other activation energies for Al lattice diffusion at high temperatures (> 480°C) such as 1.4-1.5 eV have also been reported [Volin and Balluffi, 1968].

Dislocation pipe diffusion is significant only if the dislocation density is on the order of $10^{15}/\text{m}^2$ [Hu et al., 1995, Kaur and Gust, 1990]. High dislocation densities were artificially generated by introducing plastically deformed regions (indentations) into single crystal lines [Joo et al., 1998]. These regions were shown to be fast diffusion paths. The dislocation density in typical Al alloy lines is estimated to be on the order of $10^{13} - 10^{14}/\text{m}^2$ [Alexander and Slifkin, 1970][Rose et al., 1991], or lower than $2{\cdot}10^{12}/\text{m}^2$ [Hu et al., 1995][Hu et al., 1996]. Under typical experimental conditions, the contribution of dislocations to diffusion is therefore expected to be negligible [Oates, 1996b] based on a value for $D_d A_d$ of $7 \cdot 10^{-25} \exp(-0.85eV/kT)\,\text{m}^4/\text{s}$ [Volin and Balluffi, 1968].

Interfacial diffusivities for Al interconnects have not been reported. From the drift velocities for bamboo lines, using equation 1.2 and assuming a value for Z^* between -1 and -10, the effective diffusivities can be estimated to range between 10^{-15} and $10^{-12}\,m^2/s$ at 250°C. For comparison, values for grain boundary diffusion are on the order of 10^{-10} to $10^{-14}\,m^2/s$ at 250°C, depending on the activation energy and pre-exponential factor used [Frost and Ashby, 1982, Korhonen et al., 1993b, Kaur et al., 1989]. Thus, if interface diffusion is important in the bamboo lines, it can be comparable to grain boundary diffusion.

2.2 Stresses during electromigration

Important for the formation of damage are flux divergencies, which lead to depletion or accumulation of atoms during electromigration. The effect of flux divergencies can be understood in terms of stresses: depletion of atoms generates tensile stresses, and accumulation of atoms leads to compressive stresses. The structures first suggested by Blech allow the investigation of the mechanisms of electromigration in geometrically isolated segments [Blech, 1976].

2.2.1 The Blech effect

In his electromigration experiments, Blech discovered some important facts [Blech, 1976]. In these experiments, a current was passed through Al stripes (referred to as *segments* hereafter) of various lengths which were deposited on a continuous TiN line. Such segments are sometimes called Blech-type segments. Because the resistivity of TiN is roughly 20 times that of Al, most of the current is carried by the Al. The current causes the Al to migrate (drift) in the electron flow direction, generating an area of metal depletion near the negative end of the segment and accumulation near the positive end. Some basic observations were made in this pioneering work:

- Longer segments showed a higher drift velocity than shorter ones.
- At a given current density, segments below a critical length did not drift at all.
- In a given segment length, no drift was observed below a critical current density.

The last two points are called the threshold effect or *Blech effect*.

In order to explain the threshold effect, it is proposed that electromigrating atoms create a stress gradient between the segment ends, causing a back-flux that counteracts the electromigration-induced flux. The existence of a stress gradient can be qualitatively explained by the following picture: if the segment is constrained, the motion of an atom from the cathode end to the anode end of the segment leads to a compressive stress at the anode end, and a tensile stress at the cathode end. The back-flux due to the stress gradient is given by [Herring, 1950]

$$J_b = -\frac{cD}{kT}\left(\Omega\frac{\partial\sigma}{\partial x}\right) , \tag{2.2}$$

where σ is the stress normal to the grain boundaries, and Ω the atomic volume. The total flux, electromigration-induced and stress gradient-induced, is then given by

$$J = \frac{cD}{kT}\left(\rho e Z^* j - \Omega\frac{\partial\sigma}{\partial x}\right) . \tag{2.3}$$

The number of atoms along the length of a segment evolves as a function of time according to Fick's 2^{nd} law. At steady state the electromigration and stress gradient-induced fluxes are equal in magnitude but of opposing sign. For a finite segment of length L, this leads to a linear stress profile over the length of the segment. At steady state it follows from equation 2.3 that

$$\rho e Z^* j = \Omega\frac{\Delta\sigma}{L} , \tag{2.4}$$

where $\Delta\sigma$ is the stress difference between the two ends of the segment. The stress profile is illustrated graphically in Figure 2.3.

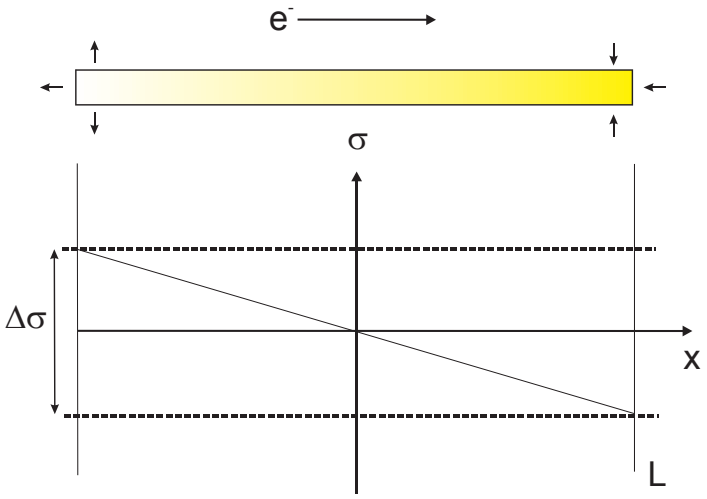

Figure 2.3: The stress difference $\Delta\sigma$ in a segment of length L. The arrows in the upper diagram refer to tensile and compressive stresses, respectively. Electron flow direction is from left to right.

The Blech effect is now readily explained by the existence of a *maximum* stress difference $\Delta\sigma_c$ that can be sustained by the material. This implies that a threshold value for jL exists which is expressed by

$$(jL)_c = \frac{\Omega\Delta\sigma_c}{eZ^*\rho} \,. \tag{2.5}$$

Using equations 2.3 and 2.5, the electromigration drift velocity (equation 1.2) can now be written as

$$v = \quad D/kT \cdot \rho e Z^*(j - j_c) \quad , \; j > j_c \tag{2.6}$$

$$v = \qquad 0 \qquad\qquad , \; j < j_c \,, \tag{2.7}$$

where $j_c = \Omega/\rho e Z^* \cdot \Delta\sigma_c/L$ is called the critical current density. The product $(jL)_c$ is called the threshold product or critical product. For a given current density, a critical length, or for a given segment length, a critical current density is required to generate damage. An experimentally determined value of $(jL)_c$ for unpassivated, pure Al segments is 1200 A/cm [Blech, 1976]. The existence of an electromigration threshold which obeys equation 2.5 has been confirmed by numerous observations, for example [Ross et al., 1989, Grabe and Schreiber, 1983, Oates, 1996b]. This concept of a back-flux induced by a stress gradient which cannot exceed a critical value is referred to as the Blech-Herring model in this work.

2.2.2 Experimental observation of stresses

The first direct observation of a stress gradient was made by Blech himself [Blech and Tai, 1977], using X-ray topography. The gradient was detected over the entire length of an unpassivated Al segment. Even earlier Blech has made an indirect observation of the back-driving stress gradient [Blech, 1976]: a segment passivated by Si_3N_4 was first depleted by electromigration. Then the current was turned off, and a back-flux of the Al was observed.

Another indirect measurement of compressive stresses due to electromigration was carried out in 1991, using NPN bipolar transistors as pressure sensors [Hemmert and Costa, 1991]. These transistors show a current gain, when operated in the conduction mode, which depends on the stress in the emitter contact. This technique is based on the fact that the bandgap of the semiconductor is a function of stress. The authors determined the build up of compressive stress as a function of

time and position along the conductor length towards the anode end. Their results are in reasonable agreement with the stress gradient models.

Recently, some direct measurements of strains in passivated Al interconnects have been performed *in-situ* during electromigration [Wang et al., 1998]. The authors investigated electromigration-induced strain gradients in 200 μm long, 10 μm wide Al segments under 1.5 μm SiO_2 passivation layers, using synchrotron-based X-ray microdiffraction. This technique allows the evaluation of the individual strain components along the conductor length and across the conductor width, which were transformed into stresses using Hooke's law. Both the steady-state and transient electromigration-induced stress gradients were examined and are in agreement with the electromigration models including stress gradients. The authors determined a steady state stress gradient of 1.2 MPa/ μm (at 260°C) at a current density of 0.1 MA/cm^2. Values for the effective valence Z^* and effective grain boundary diffusion coefficient D_{eff} for Al at 260°C were estimated to be -1.6 and $8.2 \cdot 10^{-15}$ m^2/s, respectively. In addition, the authors presented data of the stress gradient as it increases linearly with current density, if the current density was kept below the threshold density. Above the critical stress gradient (1.8 MPa/ μm), when the segment drifted, one data point was published showing that the gradient stays constant.

The measurements in the literature clearly demonstrate the existence of a stress gradient inducing a back-flux opposing the electromigration-induced flux. While the Blech-Herring model explains the electromigration behavior observed, the question of the physical origin of the threshold stress remains.

2.2.3 Threshold stresses

The critical stress gradient has been associated with the formation of damage. At the cathode end of a segment, depletion of atoms generates tensile stresses, whereas accumulation of atoms at the anode end generates compressive stresses. As a result, voids and material extrusion or hillocks are formed. These processes are briefly examined in the following.

Blech made the observation that unpassivated segments made from gold did not show a critical length effect [Blech and Kinsbron, 1975]. In contrast to aluminum, the noble metal gold does not form a natural oxide layer. In the case of Al, an Al_2O_3 scale covers the metal, such that the formation of a free surface requires energy on

the order of what is needed to nucleate a void. A number of experimental studies of void formation in Al interconnects were published over the past few years. Electromigration testing of unpassivated lines has shown that the Al_2O_3 scale remains intact as a void forms underneath [Arzt et al., 1994]. This observation implies that void nucleation occurs at the Al-Al_2O_3 interface. *In-situ* TEM observations on bamboo lines showed that voids form at the sidewalls of the lines [Riege et al., 1996]. This study also showed that the microstructure is important: the authors found that the voids formed almost exclusively at grain boundaries. Other studies showed similar results [Marieb et al., 1995][Shih and Greer, 1995]. This suggests that the interception of a grain boundary with the Al-Al_2O_3 interface is a preferred site for void formation.

The problem of void nucleation under electromigration conditions was investigated theoretically by Arzt and Nix, 1992. It was shown that homogeneous nucleation is a difficult process, and that the stresses required are much too large resulting in nucleation times, which are much too long to agree with experiments. Therefore, there must be some mechanism, or preexisting condition that makes the void easier to form than what is theoretically expected. Pre-existing voids that were formed during thin film fabrication have been suggested [Lloyd and Nakahara, 1977], but this has not been proven. There are indications that electromigration-induced voids are not necessarily associated with those that were present before electromigration testing. Such voids would accumulate vacancies efficiently, and grow readily under electromigration conditions, as has been demonstrated by intentionally added defects [Doan et al., 1999b].

The critical stresses needed to form a void have been analyzed using classical nucleation theory for different *heterogeneous* nucleation cases [Gleixner et al., 1997]. The cases of the Al-Al_2O_3 interface, a grain boundary, the line sidewall and interface notches at the sidewall have been treated. The calculations showed that even stresses as high as 2 GPa would generate nucleation rates far too low to account for observed rates. To give an example, the nucleation of a void at an interface notch poses a nucleation barrier of roughly 8.2 eV, in comparison to 25 eV for the nucleation at a grain boundary. Both barriers result in nucleation rates which are more than 60 orders of magnitude smaller than observed rates.

It was suggested that flaws smaller than 20 nm (diameter) at the Al-Al_2O_3 interface may develop into a void under typical electromigration-induced stresses [Clemens et al., 1997]. Interface flaws could be formed by contaminants, residues from the dry etching process, left-behind photo resist, and the like. No adhesion is assumed between the metal and the adjacent material at the contaminant patch. At low tensile stress, the free Al surface is driven to adopt the equilibrium surface curvature and an embryo forms. An energy barrier exists between the embryo and a stable growing void. Above a critical stress, the free energy decreases monotonically with void volume, and a stable void is formed. For example, with the presence of a flaw of 4 nm size, the critical (hydrostatic) stresses can be as low as 500 MPa, which is a reasonable value attainable by electromigration.

At locations where accumulation of atoms occurs, e.g. the anode ends of segments, compressive stresses lead to the formation of hillocks. In the cases in which the segments are not covered by a passivation, it is not clear which process limits the development of compressive stresses. It was proposed that hillock formation occurs when the yield stress of the film material is exceeded [Lloyd, 1997]. This has not been validated experimentally. To the contrary, evidence was found that the electromigration threshold stress and the yield stress determined by thermo-mechanical deformation (wafer curvature) are not equivalent [Straub, 2000]. It has also been suggested that $\Delta\sigma_c$ corresponds to a threshold stress for diffusional creep [Glickman et al., 1998]. The threshold product would depend on the deformation rate because the hillock growth then controls the stress at the anode. This implies that the critical product would have a j dependence, which requires experimental verification.

In the case in which the segments are covered by a passivation, the compressive stresses in the metal lead to tensile stresses in the passivation. Due to the brittle nature of the passivation material it cracks when the stresses are too high. Hillocks can form only after the passivation cracked. Hence, the maximum possible stress in the Al depends on the toughness of the passivation. The maximum stress a SiO_2 glass passivation can sustain was estimated to be roughly 1 GPa [Hemmert and Costa, 1991].

2.3 Time dependent models for electromigration

While the Blech-Herring model describes the steady state case, for time dependent predictions of the evolution of stress, more sophisticated models have been developed. These will be briefly reviewed in the following.

An early approach was to calculate the vacancy concentration as a function of time and position along the length of conductors [Shatzkes and Lloyd, 1986]. This was performed by a number of groups, for different boundary conditions to obtain predictions for the time to form damage [Clement, 1992, Lloyd and Kitchin, 1994, Dwyer et al., 1994, Dwyer et al., 1996]. In the Shatzkes/Lloyd model, the failure time is considered as the time to reach a critical vacancy concentration at a flux divergence. Analytical and numerical results from this model show a $1/j^2$ dependence consistent with experimental results from lifetime measurements. However, in the model it is assumed that the total number of vacancies in a segment is constant. This assumption led to failure times much too short to account for observed lifetimes. Actually, when atoms move along an interconnect segment they can change the local vacancy concentration or join sources and sinks in the material. Such sources and sinks could consist of climbing dislocations which would change the stress field. The internal stress is coupled with the vacancy concentration since it might cause generation or annihilation of vacancies (sink/source action).

In contrast, the stress model derived by Korhonen et al. assumes that the largest portion of the transported vacancies will be taken up in annihilation by climbing dislocations, thereby changing the local stress [Korhonen et al., 1993b]. From the Korhonen model more realistic lifetime values are obtained than from previous models. It is a widely accepted model for the description of electromigration phenomena. In particular, it was used to explain microstructural effects on the stress evolution during electromigration. It considers a thin and narrow interconnect line, deposited on an oxidized silicon wafer and covered by a rigid passivation layer. For simplicity, the lines are modeled as embedded in an infinitely thick, rigid dielectric. The metallization has a columnar microstructure so that there are only grain boundaries normal to the substrate. Diffusive fluxes of atoms arise due to potential differences between different locations of the interconnect line. This model will be reviewed in some more detail, since several solutions will be used to discuss the experimental data of this work.

In this model, chemical and electrical potentials are considered. The chemical potential function for atomic diffusion is the difference between the chemical potentials for atoms and vacancies [Herring, 1950]

$$\mu = \mu_a - \mu_v \ . \tag{2.8}$$

In the case that the vacancies are in local equilibrium ($\mu_v = 0$) by adding or subtracting lattice defects at the grain boundaries, the chemical potential function is $\mu = \mu_0 - \Omega\sigma$, where σ is the stress acting normal to the grain boundary.

A basic assumption of the model is that the vacancy concentration is in equilibrium with the stress, which can be expressed by

$$C_v = C_0 \exp(\frac{(1-f)\Omega\sigma}{kT}) \,, \tag{2.9}$$

where C_0 is the vacancy concentration at zero applied stress, and f is the ratio between the volume of a vacancy and an atom. When vacancies are swept towards the cathode end of a segment, they are being annihilated such that their local equilibrium concentration is maintained. This process changes the number of lattice sites in the material, producing a volumetric expansion or contraction. In a segment that is constrained by the surrounding material, stresses develop to accommodate the volume change. The flux of atoms due a chemical potential gradient $\nabla\mu$ and an electric field E is given by

$$J_a = -DC_a/kT(\nabla\mu + Eq^*) \,, \tag{2.10}$$

where C_a is the atomic concentration, D the diffusion coefficient, and $q^* = |Z^*|e$ the effective charge. The net number of atoms $\nabla J_a dt$ entering a volume element can be spent to change the vacancy concentration by dC_v, or can be deposited at a grain boundary or lattice dislocations. Korhonen assumes that atoms are deposited predominantly at grain boundaries, such that lateral stresses σ_x, σ_y are created due to the confinement. x and y refer to the directions along the length and across the width of the interconnect. Because of Poisson contraction, σ_z arises in the direction normal to the substrate. In local thermal equilibrium the chemical potential is assumed to be constant at any cross-section of the line so that the lateral stresses are equal ($\sigma_x = \sigma_y = \sigma$). Because the diffusion distance across an interconnect, which is on the order of 0.5-5 μm, is usually short compared to length of a line (on the order of 100 μm), local equilibrium is attained in a short time in comparison to the time scale of the experiment.

A uniform stress $\sigma = \sigma(x)$ over any cross-section is then defined by the position coordinate x along the line. The change in the number of available lattice sites per unit volume dC is supplied by climbing dislocations. In confined metal lines the relative density change dC/C corresponds to the stress increment as

$$\frac{dC}{C} = -\frac{d\sigma}{B} \,, \tag{2.11}$$

where B is an applicable modulus. Typical values for B are 0.3-0.5 times the Al modulus, since the strain change in the metal is accommodated by the metal, the surrounding dielectric, and the substrate. By combining the continuity equation, equation

2.9 and the flux equation 2.10, the following partial differential equation for the stress development in confined metal lines during electromigration is obtained:

$$\frac{\partial \sigma(x,t)}{\partial t} = \frac{\partial}{\partial x}\left(\kappa(x)\left(\frac{\partial \sigma(x,t)}{\partial x} + \gamma\right)\right) , \tag{2.12}$$

where $\kappa = D\Omega B/kT$ is a normalized diffusivity and $\gamma = Eq^*/\Omega$ the normalized electromigration driving force. This equation has to be solved for the appropriate boundary conditions. The diffusivity D was assumed to be independent of stress.

Another formulation of the same model can be established by considering the flux of vacancies instead of atoms [Clement and Thompson, 1995]. In this formulation, a sink/source term was included in the continuity equation to account for the generation or annihilation of vacancies at climbing dislocations. As in the Korhonen model it is assumed that the vacancy concentration is in equilibrium with the local stress field. The authors follow Korhonen's reasoning and argue that the largest portion of the transported vacancies will be taken up by changing the local stress, whereas only a small number of vacancies will go into changing the local vacancy concentration to maintain the local equilibrium with the stress. Korhonen et al. assumed in their derivation that the lattice site concentration is effectively constant $C = C_a = 1/\Omega$, where C_a is the atomic concentration. Clement and Thompson showed that if this assumption is used, the models are equivalent.

The Korhonen model will be used to analyze several experiments in this thesis. Therefore analytical solutions of the central equation 2.12 for different boundary conditions are described in the following.

2.3.1 Solution: Semi-infinite line

The simplest case is a semi-infinite line where the flux is blocked at $x = 0$ [Korhonen et al., 1993b]. Physically, the blocking boundary might be caused by a tungsten via or by a region where the Al has been removed as in the case of Blech segments. The stress as a function of position and time, obtained by the method of Laplace Transformation, is given by

$$\sigma(x,t) = \frac{Z^* e \rho j}{\Omega}\left[\sqrt{\frac{4\kappa t}{\pi}}\exp\left(-\frac{x^2}{4\kappa t}\right) - x\,\mathrm{erfc}\left(\frac{x}{\sqrt{4\kappa t}}\right)\right] , \tag{2.13}$$

The stress at $x = 0$ becomes

$$\sigma(0,t) = \frac{2Z^* e \rho j}{\Omega}\sqrt{\frac{DB\Omega t}{kT\pi}} . \tag{2.14}$$

Damage occurs when the stress at $x = 0$ reaches a critical value, σ_c, as suggested by Blech's experiments (section 2.2.1). The incubation time t_{inc} to reach σ_c is then given by

$$t_{\text{inc}} = \frac{kT\pi}{DB\Omega}\left(\frac{\Omega\sigma_c}{2Z^*e\rho j}\right)^2 , \tag{2.15}$$

where $D = D_0 \exp(-E_a/kT)$. This expression has the form of equation 1.3, which Black originally proposed from his empirical results.

2.3.2 Solution: Finite segment

In the case of an Al segment of length L on a continuous TiN line, the flux is blocked at both ends ($J(0,t) = J(L,t) = 0$) [Korhonen et al., 1993b]. With these boundary conditions the time dependent solution $\sigma(x,t)$ is given by

$$\sigma(x,t) = \frac{Z^*\, e\, j\, L\, \rho}{\Omega}\left(\frac{1}{2} - \frac{x}{L} - 4\left(\sum_{m=0}^{\infty}\frac{1}{m^2}\exp(-m^2\,\frac{B\,D\,t\,\Omega}{k\,L^2\,T})\,\cos(m\,\frac{x}{L})\right)\right) , \tag{2.16}$$

where $m = (2n+1)\pi$. The steady state solution results in the simple expression:

$$\sigma(x,\infty) = \frac{Z^*q\rho jL}{\Omega}\left(\frac{1}{2} - \frac{x}{L}\right) . \tag{2.17}$$

The maximum steady state stress occurs at both $x = 0$ and $x = L$. The magnitude is given by

$$|\sigma_{max}| = \frac{Z^*e\rho jL}{2\Omega} . \tag{2.18}$$

This stress corresponds to half the stress difference $\Delta\sigma$ between the two ends of the segment, which is consistent with the steady state solution originally given by Blech and Herring, 1976, (equation 2.4).

2.3.3 Solution: Finite segment with void

In the last case to be considered it is assumed that there is a void present at the cathode end ($x = 0$) of the segment, implying that the stress is zero at this end [Korhonen et al., 1993a]. The flux at the anode end is assumed to be blocked. Additionally, a constant thermal stress σ_T along the length of the segment is assumed, before electromigration begins at $t = 0$. The solution can be separated into two parts:

$\sigma_{em}(x,t)$ due to electromigration alone, and $\sigma_T(x,t)$ due to relaxation of thermal stress.

$$\sigma_{em}(x,t) = -\gamma \left(x - 2L \sum_{n=0}^{\infty} (-1)^n \exp\left(-k^2 \kappa t / L^2\right) \sin\left(kx/L\right) / k^2 \right) \quad (2.19)$$

$$\sigma_T(x,t) = 2\sigma_T \sum_{n=0}^{\infty} \exp\left(-k^2 \kappa t / L^2\right) \sin\left(kx/L\right) / k \quad (2.20)$$

where $k = (n+1/2)\pi$. The void volume can be calculated at any time t by integrating the strain associated with the atomic redistribution as

$$V(t) = \left(\frac{1}{B}\right) \int_0^L \sigma(x,t)\, dx \quad (2.21)$$

where, as well as in what follows, the void volume is normalized by the cross-section area. Substitution of equations 2.19, 2.21 and integration results in

$$V(t) = V_{em}(t) + V_T(t)\ , \quad (2.22)$$

where the volume is separated into the two parts for electromigration-induced depletion and for relaxation of thermal stress. These volumes are given by

$$V_{em}(t) = \frac{\gamma L^2}{2B} \left(1 - 4 \sum_{n=0}^{\infty} (-1)^n \exp\left(-k^2 \kappa t / L^2\right) / k^3 \right) \quad (2.23)$$

$$V_T(t) = \frac{L\,\sigma_T}{B} \left(1 - 2 \sum_{n=0}^{\infty} \exp\left(-k^2 \kappa t / L^2\right) / k^2\ . \right) \quad (2.24)$$

The maximum void volume at saturation is

$$V_{max} = \frac{\sigma_T}{B} L + \frac{\gamma}{2B} L^2\ . \quad (2.25)$$

The time dependent void size, and the void size at saturation, can be compared with measurements.

2.3.4 Incubation time

The incubation time to nucleate a void or to form a hillock is, according to the models, defined by the time to develop a critical stress. All models predict that nucleation times scale with j^{-n}, where $n \geq 2$. In the literature one can find only few attempts to measure nucleation times directly. In a recent study the nucleation times and growth rates of electromigration-induced voids were measured by means of electron microscopy and concurrent resistance measurements in pure Al lines [Doan et al., 1999a]. The results indicate that the nucleation time of the first void in a line scales roughly as j^{-1}. This result conflicts with the standard models described above. It is also not

consistent with another study, in which incubation time and void growth were examined separately [Kawasaki et al., 1998]. In this case the authors used via-terminated interconnect segments. Experimentally, a resistance measurement method was used to determine void nucleation times as well as the growth rates. The nucleation times were found to scale roughly with the inverse square of the current density, whereas the growth rate scaled roughly with the inverse of the current density, which is in agreement with the models. However, in these experiments an Al(1% Cu) alloy was used. Cu is known to reduce the Al drift [Hu et al., 1993a, Spolenak et al., 1998b], thus it is not clear whether these results can be compared directly with the stress models.

2.4 Passivation of interconnects

Interconnects in integrated circuits are always covered with interlevel dielectric/passivation layers. The function of these overcoat layers is to provide electrical isolation, and protection against mechanical damage and corrosion. In early studies it has been shown that the electromigration lifetime of Al interconnects is substantially improved by covering the lines with a rigid passivation [Black, 1967, Spitzer and Schwartz, 1969, Ainslie et al., 1972]. Materials such as SiO_2, P- or B-doped SiO_2, and polyimide have been used as passivation layer materials. The lifetime enhancement may be brought about in two ways, either from a change in the nucleation conditions for voids or hillocks, such that damage formation is more difficult, or from a decrease in the rate of electromigration caused by high compressive stresses in the metal.

In the latter case, a reduction in the diffusivity occurs due to compressive stresses imposed by the passivation layer [Ainslie et al., 1972, Lloyd and Smith, 1983, Ross et al., 1989]. The atomic diffusivity as a function of stress is given by

$$D = D_0 \exp\left(\frac{\sigma \Omega_A}{kT}\right) , \tag{2.26}$$

where D_0 is the atomic diffusivity at zero applied stress, σ is the hydrostatic stress, and Ω_A is the activation volume. Ω_A has been measured for Al bulk diffusion to be roughly $1.3\,\Omega$ [Tomizuka and Emerick, 1965]. A value for Al grain boundary diffusion is not available. For example, from equation 2.26 it is expected that D decreases by 20% for 100 MPa hydrostatic compression at 500 K. Whether this effect is important for electromigration is disputed. In the study of Ross et al. a reduced drift velocity

was observed, if the segments were covered by a passivation [Ross et al., 1989]. For these measurements, a fraction of the Al layer was anodized at room temperature. The oxide layer served as "passivation". When such segments are tested at elevated temperatures, a different stress state is expected than if conventional passivation is used. Conventional passivation layers are deposited at elevated temperatures leading, to tensile stresses in the interconnects due to thermal mismatch.

Kahn and Thompson studied the effect of an applied mechanical bending stress on the electromigration failure times (open lines) of unpassivated lines [Kahn and Thompson, 1991]. They found that the lifetime decreased with increasing applied tensile stress, and that the activation volume is similar to the vacancy volume. The study showed that the increase in the grain boundary diffusivity alone is too small to explain the lifetime decrease. This suggests that a passivation may change the critical stress for damage formation, such that the improvement in failure times depend mainly on the change of $\Delta\sigma_c$ with passivation.

The addition of a passivation layer increases the threshold product making damage formation more difficult. Whereas unpassivated lines show threshold products around 2000 A/cm [Lloyd and Smith, 1983], passivated sub-micron wide lines have threshold products around 5000 A/cm [Gall, 1998]. Also Ross et al. found that the threshold product increased after anodizing the Al segments [Ross et al., 1989]. The increase in the critical current density, derived from the increase in threshold product (equation 2.6), did not account for the reduction in v measured by Ross et al. It should be mentioned that the threshold product was obtained from segments that have already begun to drift, which is problematic because j_c could be significantly different from the value of undamaged segments.

From the literature it is not clear what the important effect of the passivation is: whether it significantly reduces the Al mobility, or it changes the threshold for damage formation. This issue calls for further investigation.

2.5 Addition of Cu to Al interconnects

It was first recognized in 1970 that the addition of a small percentage (0.5-4 wt%) of Cu enhances the lifetimes of Al interconnects by up to two orders of magnitude [Ames et al., 1970]. Al(Cu) alloys are now routinely used for interconnects in microelectronic devices. The effect of Cu on Al electromigration has been a field of intense study ever since, although the exact mechanism is still not fully understood. It is known that the distribution of the Cu in the interconnect has a large influence on the Al motion [Theiss and Prybyla, 1996, Kang et al., 1996]. In particular, it has been reported that Al only begins to move after an incubation time during which the Cu is preferentially depleted from the cathode region of an interconnect segment [Shine and d'Heurle, 1971, Grabe and Schreiber, 1983, Spolenak et al., 1998b, Hu et al., 1993a, Witt and Volkert, 1997]. Extrapolation to lower temperatures shows that the rate of Cu depletion may be more important than the rate of Al motion in determining the time to failure under service conditions [Kawasaki et al., 1998]. Thus the distribution of the Cu in the interconnect is very important in predicting and understanding the electromigration reliability of interconnects.

The Cu effect was mostly studied in polycrystalline material. It has been proposed that the Al diffusion in grain boundaries is retarded by the presence of Cu [Rosenberg, 1972]. Whether Cu has a large effect in bulk diffusion is not clear. Evidence from bulk Al alloys indicates that, in contrast to grain boundary electromigration, Al electromigration in the lattice is enhanced by Cu atoms in solution [Doan and Bocquet, 1975]. Whether Cu has a large effect in bamboo structures is also not clear. Although interfacial diffusion has not been characterized, it is possible that alloying with Cu may effect interfacial transport in the same manner as along grain boundaries. The retarding effect of Cu in the case of a bamboo microstructure is not well documented: in one reference incubation times were reported on 0.7 μm wide lines, which had a near bamboo microstructure [Hu, 1995]. In another publication, *no* incubation time was found in very narrow Al(Cu) lines (0.3 μm) [Proost et al., 1998].

The Cu redistribution during the incubation time has been investigated by analytical measurements in polycrystalline Al(Cu) segments [Spolenak et al., 1998b]. Analytical methods such as energy dispersive X-ray analysis (EDX) are not capable of distinguishing between Cu that is in solution or in precipitates. Commonly it is assumed that precipitates serve as reservoirs for depleted Cu in solution, thus it is expected that precipitates play an important role in the Cu redistribution process. Precipita-

tion in thin Al(Cu) films has been studied thoroughly by Rutherford backscattering (RBS) and X-ray absorption spectroscopy (XAS) [Marcus and Bower, 1997]. Figure 2.4 shows a map of precipitate observations at different film deposition temperatures as a function of Cu concentration. At low Cu concentrations and low temperatures, precipitates are expected from the equilibrium solvus, but they were not observed (triangles in Figure 2.4). This was explained by the solute trapping phenomenon: solute atoms deposited at low temperatures are trapped where they land. Since they must diffuse in order to precipitate, precipitation is suppressed at low temperatures.

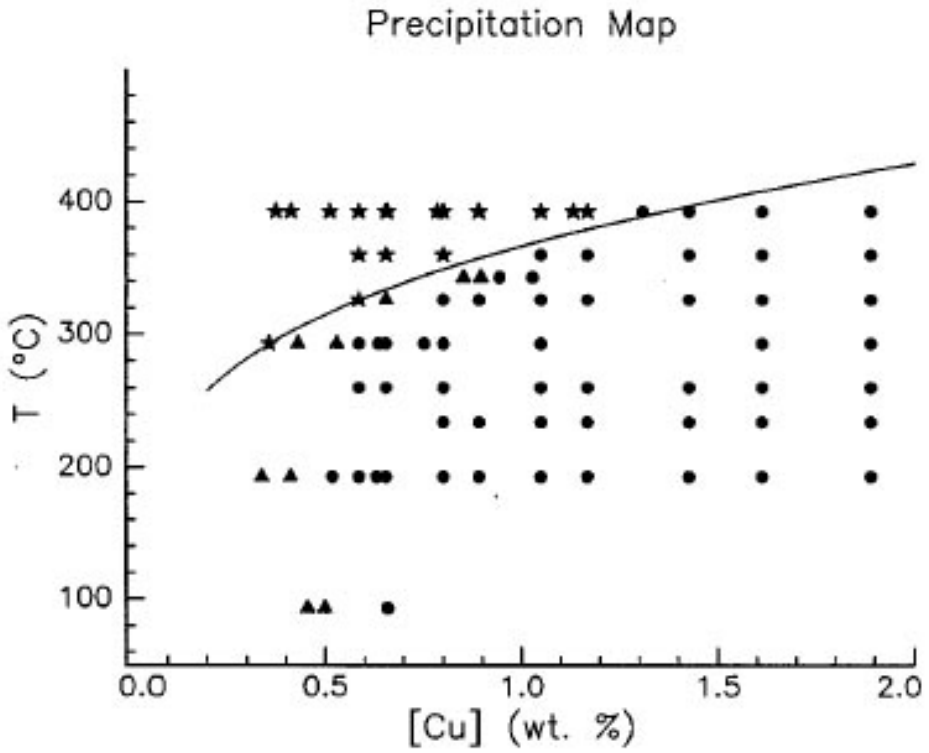

Figure 2.4: Effective phase diagram of Al(Cu) films after deposition. The ordinate represents the deposition temperature and the abscissa the depth-average Cu concentration. The solid curve is the bulk equilibrium solvus. Dots indicate evidence of precipitation, the stars indicate Cu in solution. The triangles show samples for which precipitates are expected, but none was found. After [Marcus and Bower, 1997].

The instability of precipitates during electromigration was investigated by a number of researchers. The depletion of Cu from the cathode end of an Al(Cu) interconnect segment has been shown to include the disappearance of Al_2Cu precipitates, which appear to act as reservoirs replacing the Cu electromigrating downstream along the line [Blech, 1977]. The instability of Al_2Cu precipitates was observed by *in-situ* TEM

experiments [Rosenberg, 1972, Kim and Morris, 1993, Theiss and Prybyla, 1996]. In these studies, single Al lines connected to bonding pads at both ends were used. These pads may act as reservoirs re-supplying Cu atoms that were removed from a precipitate by electromigration. In another study Al(Cu) segments connected to W pads, which act as diffusion barriers, were observed *in-situ* by TEM [Shaw et al., 1995]. It was found that precipitates near the cathode end of the segment dissolved during electromigration and other precipitates grew near the anode end of the segment. The dissolution of precipitates did not lead to the formation of voids, i.e. the original precipitate volume was *refilled* by Al. Since the total number of atoms is conserved in this system, it might be concluded that a back-flux of Al exists. This phenomenon, following speculations of the authors, might be due to a vacancy gradient resulting from the Cu flux. The implication is that an Al flux opposite to the electromigration flux would add significantly to the lifetime.

The retarding effect of Cu was also treated theoretically. A commonly accepted idea of the effect of Cu is that the Al diffusivity is greatly reduced by the presence of Cu, although the exact mechanism is not clear. Early theoretical considerations were based on a binding between Cu atoms and vacancies, which reduces the amount of mobile vacancies in the alloy [Rosenberg, 1972]. There are some interesting recent developments in this area: based on atomistic simulations it was suggested that Cu atoms segregate preferentially to grain boundary interstitial sites due to a stronger bonding of Cu atoms to Al neighbors [Liu et al., 1999]. Following the reasoning of the authors, the activation energy for jumps of Al atoms is increased by the presence of Cu atoms, thus diffusion along grain boundary paths is impeded if a sufficient number of Cu atoms is present at the grain boundary. As an important alloying effect, the solute drag effect on the mobility of grain boundary dislocations has been proposed [Spolenak et al., 1997]. Other theoretical developments apply atomistic jump models, developed for diffusion in dilute binary alloys, to the case of electromigration [Dekker and Gumbsch, 2000]. These results show that if Cu atoms and vacancies diffuse as pairs (assuming a strong Cu-vacancy bond), some Al atoms diffuse against the electron wind reducing the total Al flux. More recently, a new, co-operative diffusional mechanism was proposed, in which diffusive jumps of Al atoms in the vicinity of Cu atoms are preferred [Schmidt et al., 2000]. This leads to an increased dwell time of vacancies in the vicinity of Cu atoms and a flux of Cu atom-vacancy pairs occurs, which generates a back-flux of Al atoms. This concept does not rely on a binding between Cu atoms and vacancies.

It is worth mentioning that the effect of Cu to reduce the Al mobility has been verified in recent experiments [Kao et al., 2000]: the local strain of a polycrystalline Al(Cu) segment was measured *in-situ* during electromigration by X-ray microdiffraction. Simultaneously, the Cu concentration was measured using X-ray fluorescence. The study showed that, when Cu is swept towards the anode end, a strain/stress gradient persists only up to a position where the Cu exceeds a certain critical concentration (0.15 at% at 310°C). That means that the Al flux is basically "blocked" behind that position, which is sometimes called the *copper front*.

2.6 Objectives of this work

The purpose of this work is to illuminate the effect of a passivation and the addition of Cu on electromigration in sub-micron wide, Al interconnects with a bamboo microstructure. The literature overview shows that there is still no agreement about the importance of interface diffusion in bamboo lines. There are several reasons for this discrepancy: the large variety of fabrication processes and interfaces that are used appear to have a great influence on measured drift velocities. The unavailability of a suitable radioactive tracer for Al generates some uncertainty when comparing electromigration data with literature diffusivity values.

While the retarding effect of Cu on Al drift in polycrystalline interconnects has been demonstrated in a number of studies, the picture for bamboo Al(Cu) lines is less consistent. No attempt has been made to analyze the motion of Cu in bamboo lines during electromigration. A reason for this lack might be the difficulty to measure the position of Cu in such small dimensions, in particular at low Cu concentrations around 0.5 wt%. On a phenomenological basis, the effect of Cu is understood in terms of a reduction of the Al diffusivity in grain boundaries. Whether this model can be transferred to bamboo lines has to be verified.

The existence of the classical Blech product was confirmed by many groups. Also the existence of a stress gradient was confirmed several times. Attempts to obtain statistical information on the threshold product were not made. From the theoretical point of view, physically based models were established describing the evolution of stresses during electromigration for various boundary conditions. More experimental verification of the models has to be performed; in particular, studies on the early stage of electromigration are rare. Most work was done in form of lifetime measurements,

although lifetimes incorporate the incubation time for damage formation and the evolution of damage to a certain size. Attempts were made to observe the damage stages separately, but the results are not consistent with the models. The beneficial effect of adding a passivation layer was attributed to a reduction in diffusivity, or a change in the threshold for damage formation. Separate measurements of the drift velocity and threshold product with and without passivation should be made to illuminate the effect.

3

Experimental

3.1 Sample fabrication

3.1.1 Al(Cu) segments

Electromigration drift experiments were performed on Al(0.5 wt%Cu) Blech-type segments on a continuous TiN line. Test interconnects of 0.8, 0.5, and 0.3 μm width were fabricated in a clean room environment, at the Bell Laboratories, New Jersey, from a film stack of 500 nm thermally grown SiO_2 / 45 nm sputtered Ti / 300 nm sputtered TiN / 400 nm sputtered Al(0.5 wt%Cu) / 30 nm sputtered TiN (anti reflection coating) and approximately 100 nm PECVD SiO_2. The TiN thickness was chosen to keep Joule heating negligible during electromigration testing. The final SiO_2 layer was required as a mask to protect the metal during etching. Otherwise the stack was a standard device metallization stack. Following film deposition, the wafers were annealed for 60 min at 400°C in forming gas to promote grain growth. Next, the metal films were patterned using UV lithography and reactive ion etching to form single line test structures. In a second step 5 μm long gaps in the Al were patterned leaving Al segments on the TiN line with lengths varying between 5 and 100 μm (4 of 5 μm length, 5 of 10 μm length, 4 of 20 μm length, 2 of 25 μm length, 1 of 35 μm length, 3 of 50 μm length, 2 of 100 μm length). The TiN underlayer was kept continuous to provide electrical conductivity. The Al segments are shown schematically in Figure 3.1. After patterning the wafers received an additional anneal at 400°C for 30 min in forming gas to stabilize the microstructure. Some samples received an additional (200 nm) passivation layer of SiO_2 deposited at 400°C by plasma enhanced CVD. The passivation on the contact pads was removed by reactive ion etching to allow for contacting.

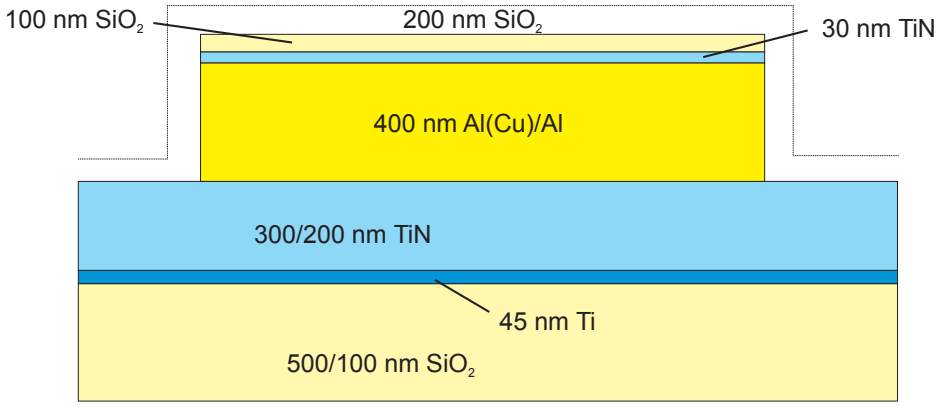

Figure 3.1: Schematic diagram of the cross-section of the sample structure used. The different film thicknesses refer to the sample types Al(Cu) and pure Al. In the case of passivated segments, 200 nm SiO_2 was added conformally on top.

The wafer was cleaved into roughly 8x8 mm large pieces (dies). Each die contains several test structures. Each test structures consists of a 800 μm long, sub-micron wide TiN line with the Blech-segments on top. These sub-micron wide lines are connected to 20 μm wide lines, which lead into four large contact pads. The contact pads can be used for 4-point resistance measurements. A test structures is shown in Figure 3.2.

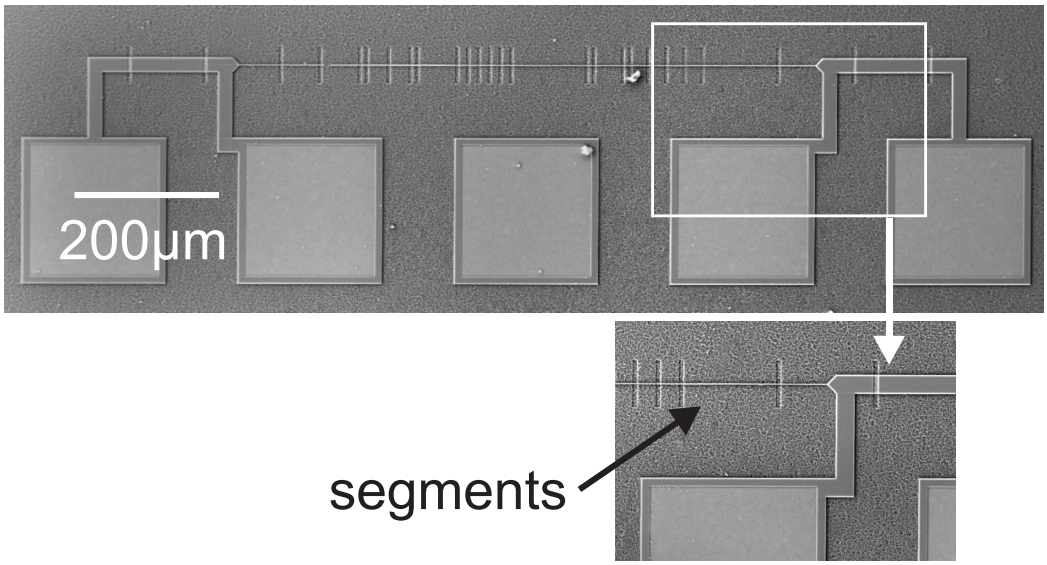

Figure 3.2: SEM micrograph of an electromigration test structure. The 0.5 μm wide, and 800 μm long line is connected to 20 μm wide lines, which terminate at (200x200) μm^2 large contact pads. The Blech-segments can be seen in the inset in the lower right corner.

3.1.2 Pure Al segments

The pure Al samples were fabricated in a second batch with a process similar to the one used for the Al(Cu) samples. In this case the thermal SiO_2 underneath the Ti/TiN was 100 nm and the bottom TiN was 200 nm thick. In contrast to the Al(Cu) samples, the Blech-segments were made of identical length on each test structure. This is advantageous, because the resistance change of such test structure can be used as a measure of the average Al displacement. The segment lengths varied between 10 and 195 μm (53 of 10 μm length, 32 of 20 μm length, 23 of 30 μm length, 14 of 50 μm length, 10 of 75 μm length, 8 of 95 μm length, 4 of 195 μm length). One test structure on each die was equipped with only one 5 μm long gap at one end, whereas the other end was still connected to the bonding pad. This geometry is referred to as reservoir end hereafter.

3.2 Sample characterization methods

3.2.1 Focused Ion Beam

A focused ion beam microscope, or shortly FIB, was used to image the grain structure of the Al films as well as to characterize the interconnect structure [FEI, 1998]. The working principle of an FIB is similar to that of an SEM: charged, accelerated (30 keV) particles are being deflected by electromagnetic fields in order to scan the beam across the surface of the sample. The secondary electrons detected at every beam position are used to generate the image. The interaction of the ions with a crystalline sample depends on the orientation. The contrast between individual orientations is called channeling contrast. Using this contrast, the FIB is able to reveal the microstructure of polycrystalline material. Due to the orientation sensitivity, the channeling contrast depends on the tilt angle at which the image is acquired. As a result, some ambiguity arises with regard to the microstructure, if only one tilt angle is used, because it is sometimes difficult to distinguish two adjacent grains. In order to avoid errors, at least three images at different tilt angles should be taken.

Using ions as scanning beam implies another feature of the FIB: the scanning ion beam removes material off the surface by sputtering. As a consequence, the surface oxide of metallic specimens is being removed resulting in a good channeling contrast. This is particularly important for Al specimens, since they oxidize even in a vacuum atmosphere of 10^{-6} mBar which is typical for the FIB specimen chamber. Additionally,

the sputtering effect of the ion beam can be used to remove material selectively from areas specified by the operator. Utilizing this feature, it is possible to produce cross-sections of films or interconnects, and image the sectioned area afterwards without the need to transfer the sample to another instrument. In a similar manner, TEM specimens can be thinned by FIB. This technique was applied in this work to thin interconnect segments in some cases. Further details of the TEM sample preparation are described by Spolenak et al., 1998a.

It should be noted that a liquid-metal ion source made from Ga is used in the FIB to generate the ions. Some of the Ga is being implanted by the ion beam, therefore specimens prepared by FIB are Ga contaminated.

3.2.2 Transmission Electron Microscopy

Because of the thick TiN (300 nm) underneath the Al, a conventional plan view preparation was not appropriate for the present interconnects, hence a side-view approach was taken. A side-view TEM specimen is schematically shown in Figure 3.3. A single test structure was diced from the wafer using a diamond saw. This silicon slab was roughly 2 mm long and 0.2 mm wide, with the long side parallel to the Al line. Next, the slab was ground and polished from both sides to achieve a final thickness of roughly 50-60 μm next to the interconnect. This was carried out using a tripod resulting in a slightly trapezoidal-shaped slab.

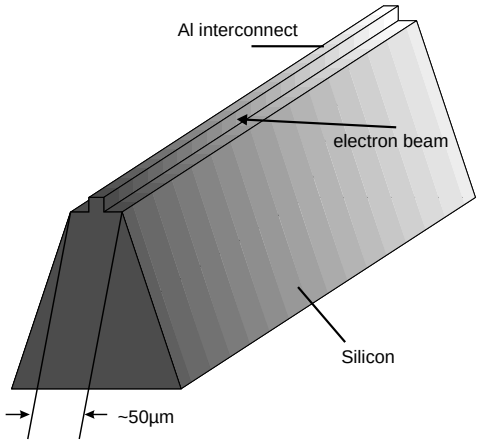

Figure 3.3: Schematic of specimen preparation for TEM side-view imaging. The width of the top face was minimized to allow for sample tilting without shadowing.

This slab was finally glued on a 3 mm (Cu- or Ni-)ring, which could be mounted in the TEM sample holder. In the case of *post-mortem* investigations, the interconnect width was thinned by ion milling in the FIB. This procedure resulted in interconnect

segments of typically 100 to 150 nm width which was sufficiently thin to be transparent for a 200 keV electron beam. The thinned regions were typically 20-30 μm long. For interrupted electromigration experiments, TEM inspection was desired before and after electromigration, hence *no* FIB thinning was used. Lines covered by a passivation were not electron transparent at 200 keV, therefore a high energy microscope (1 MeV) [AEI, EM7] was used.

3.3 Electromigration testing

All samples were tested at constant current and at constant temperature. In the course of this work, different equipment has been used for electromigration testing.

3.3.1 Ex-situ

Early electromigration experiments were performed *ex-situ* in a furnace. For SEM inspection, the tests were interrupted so that the specimen could be transferred into the microscope. The furnace was part of a commercially available electromigration testing system [Microinstruments, 1995]. Sample dies were mounted into a ceramic chip carrier using wire bonding for electrical connection. Details on wiring and the chip-carrier are described in Appendix A.

3.3.2 In-situ

Early *in-situ* testing was performed using a commercial hot plate/probe station manufactured by RAITH. The sample was glued on the hot plate using silverpaint (Fa. Plano). Electrical connection was established by tungsten probes which were attached to arms which could be moved by motorized stages. This allowed for remote control, such that contacting could be performed inside the SEM.

A new *in-situ* test apparatus, described in detail in Appendix A, has been developed for several reasons: first, electrical contact by probes was not found to yield reproducible resistance measurements at a resolution required for drift measurements. Second, due to the mechanical construction, the minimum working distance (between the pole piece of the SEM and the sample surface) had to be on the order of 24 mm. To obtain higher resolution, a working distance on the order of 10 mm is more desirable.

It was also desired to be able to rotate and tilt the sample for SEM inspection while testing, which was not possible with the probe stage due its large size. When designing the new stage, it was taken into account that it is compatible to other microscopes.

Temperature stability

An important requirement for accurate drift measurements is the thermal stability of the measurement set-up. The temperature is measured by a thermocouple mounted directly on the sample. The long term temperature stability of the test stage used is better than 0.2°C as shown in Figure 3.4. The sample (die) temperature was confirmed

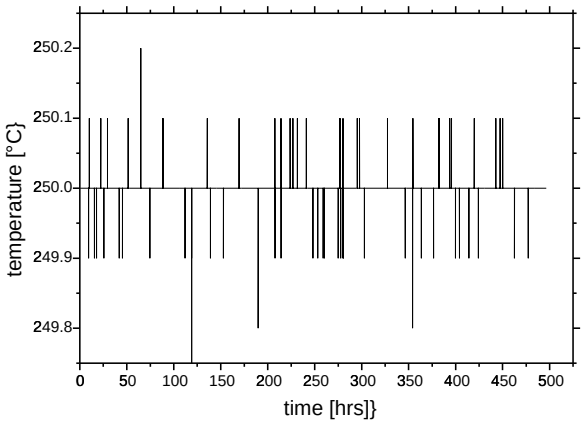

Figure 3.4: Temperature stability of the *in-situ* testing stage over a period of 20 days. The deviations from 250°C did not last longer than 3 min.

by measuring the resistance of some test structures (4 point measurements) and heating the stage, first, by the heater and, second, externally in a furnace with known ambient temperature. The furnace was equipped with an air homogenizer (ventilator), therefore the furnace temperature was taken to be a good reference. The temperature of the chip was found to deviate from the reference by less than 2°. The stage was tested up to temperatures of 380°C, the maximum temperature it was designed for is 400°C, which is limited by the stainless steel parts used, making it suitable for testing of Cu-based interconnects.

Electronic stability

The accuracy of the resistance measurements was assessed by monitoring the resistance of a test structure at a current density much smaller than the threshold density. The structure consisted of four passivated, 200 μm long, and 0.5 μm wide pure Al segments. The current density was 0.01 MA/cm^2. The resistance measurement over a period of roughly 3 weeks is shown in Figure 3.5. The measurement shows clearly a 24 h period, which was due to the daily temperature change in the laboratory, which

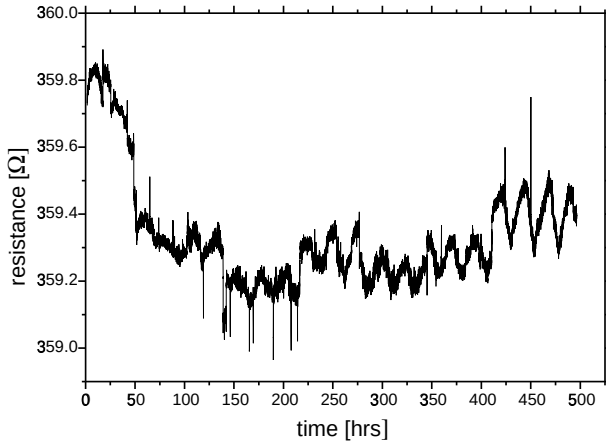

Figure 3.5: Resistance measurement of non-drifting pure Al segments. Data acquisition interval was 2 min, test temperature was 250°C.

did not have climate control. This became clear by opening or closing the window shades. The short term noise in the signal is on the order of 50 mΩ (peak to peak). The spikes in the signal occurred when the sample was moved for SEM inspection. They are due to short term temperature changes on the order of 0.2°C, which occurred because the radiation reflection changed by moving the sample near the pole piece of the microscope. In spite of that, there is a significant resistance decrease during the first 100 hrs which is probably due to healing of defects in the interconnect.

3.4 Measuring electromigration-induced drift

3.4.1 A new method for drift measurements: EDX mapping

A new experimental method was developed using energy dispersive X-ray (EDX) analysis in a Scanning Electron Microscope (SEM). It can be used to quantitatively measure the amount of Al material depleted and accumulated due to electromigration in both passivated and unpassivated interconnects. The objectives of establishing this technique was to look more carefully at the absence of atom motion in sub-critical long Al segments and to measure small amounts of Al drift accurately. The electron beam is used to generate a spectrum of X-rays from a region near the surface of the sample; by measuring the characteristic X-ray intensity one gets a measure of the number of atoms of each element of interest. When the electron beam is scanned across the sample a 2-dimensional map of the elements is obtained. Thus, when calibrated correctly, the technique can be used to quantitatively determine the amount of Al in an interconnect section.

To measure the Al depletion due to electromigration, a standard SEM/EDX system [JEOL6400, 1994] was used. A 15 keV electron beam at normal incidence was stepped over the sample and the emitted radiation was detected by a Si(Li) energy dispersive detector and then spectrally analyzed. At each point on the surface the K_α X-rays from Al and Si were recorded resulting in two element maps, as well as an SEM image as illustrated in Figure 3.6.

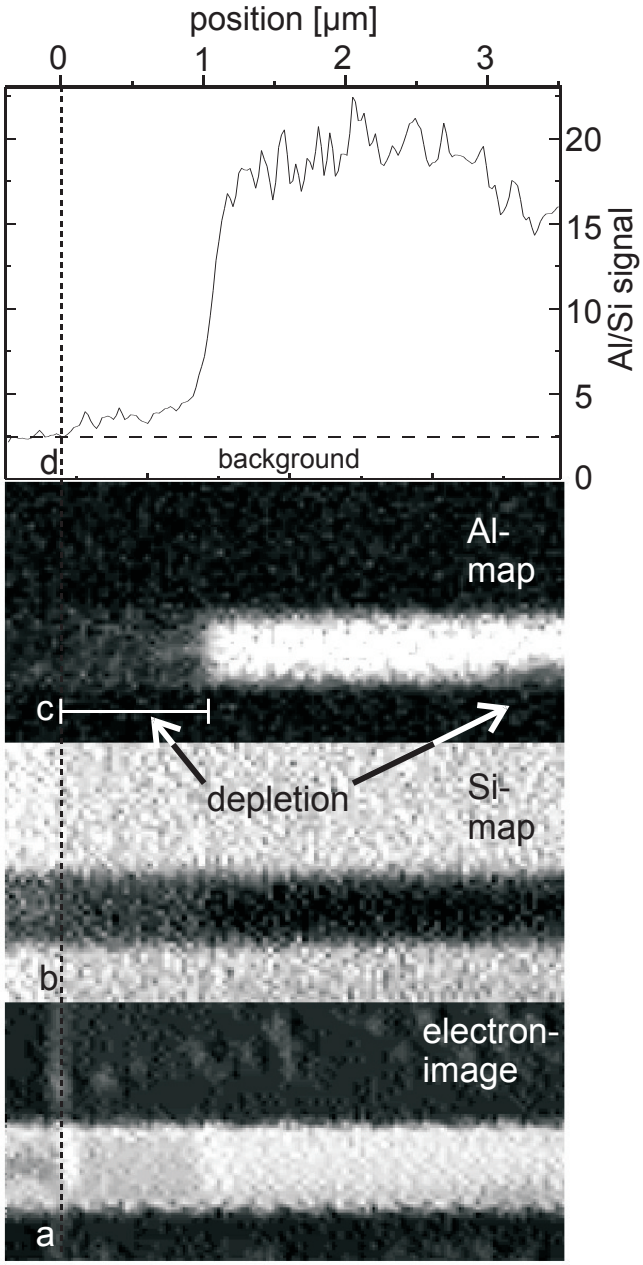

Figure 3.6: The cathode-end of an unpassivated, 0.5 μm wide, and 20 μm long Al segment after 100 hrs of testing at 2 MA/cm^2 and 200°C. Depletion occurred at the cathode end of the segment as well as 3.5 μm from the end. The original end of the segment is indicated by the dashed line. Residual Al material can be seen in the depleted section in both the Al-map (c) and in the Al/Si signal (d). It is difficult to detect this in the secondary electron image (a).

Subsequent to data collection, the Al counts (Figure 3.6 c) at each point in the entire map were divided by the Si counts (Figure 3.6 b) in order to avoid effects of variations in electron beam intensity during acquisition. This ratio was then summed across the width of the Al-segment leading to a one-dimensional, width-averaged measure of the Al concentration along the length of the line (Figure 3.6 d), referred to as the Al/Si signal hereafter. Since the Al signal decreases and the Si signal increases with decreasing Al concentration, the ratio Al/Si is more sensitive to Al concentration changes than the Al or Si signal alone.

In order to accurately align the Al/Si curves obtained at different measurement times, the position of the step in the silicon oxide was used (dashed line in Figure 3.6) which was created by the etching used to segment the Al runner. To determine the amount of material depleted by electromigration at any given time, the Al/Si signal was subtracted from the initial Al/Si signal, and this difference was summed over the length of the segment resulting in a final value Δs, which was converted into an edge displacement.

The electron beam current (0.1 - 1 nA) and the detector settings were chosen to maximize the number of Al K_α X-ray counts recorded per unit time without generating pile-up of pulses in the acquisition system. In order to keep the sample current roughly the same for all measurements it was periodically examined at a particular spot on the sample. Typical maps contained 50 x 100 points at a point spacing of 0.05 μm. The dwell time of the electron beam at each point on the surface was typically 50 - 100 ms, so that an entire map could be acquired in less than 10 min. This resulted in the generation of roughly 50 Al K_α X-ray counts per point from a 400 nm thick Al film. The time of 10 min was chosen to avoid significant motion of the sample stage which was on the order of $\sim$ 10 nm/min during map acquisition.

Another important parameter to choose in this set-up was the electron energy. At low energies the characteristic X-ray intensity increases with the electron beam energy. However, at higher energies the cross-section for elastic scattering decreases leading to a maximum in the Al X-ray intensity. For a 400 nm thick Al film the maximum was found at roughly 12 keV. The electron energy dependence is shown in Figure 3.7, together with the ratio of the Al and Si signals. For higher energies the X-ray excitation volume of the surface Al film decreases with energy, enhancing the lateral resolution in the Al. As a compromise, an electron beam energy of 15 keV was chosen to maximize Al X-ray counts while still maintaining reasonable lateral resolution which was on the

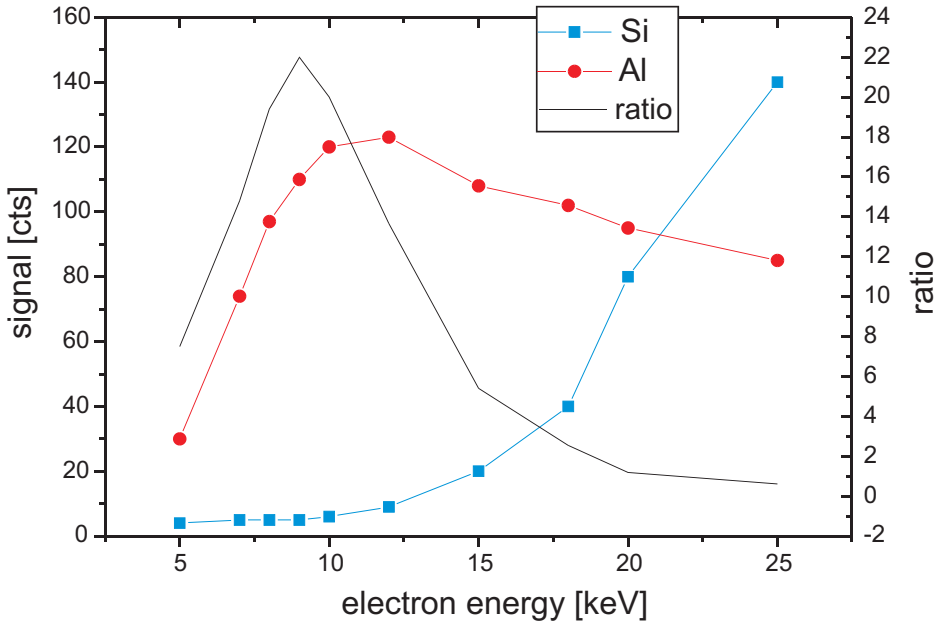

Figure 3.7: EDX X-ray signals as a function of electron energy: The signals were taken simultaneously on a continuous (unpassivated) TiN/Al(400 nm)/TiN/Ti film stack.

order of 400 nm as determined by measuring the width of the rise in the Al K_α counts (roll-off) during a line scan across a sharp Al film edge shown in Figure 3.8. This corresponds roughly to the diameter of the activated volume in the Al. The roll-off in the Al signal occurred as the film edge intercepted the activation volume.

Beyond the film edge, where the electron beam impinges the SiO_2 substrate, the Si signal increases by 25% due to lower attenuation of primary electrons (label a in Figure 3.8). The Si X-ray radiation is still shadowed as long as the electron beam is in proximity to the Al film edge (label b in Figure 3.8). Only at a distance of 3-4 μm away from the film edge is the unshadowed Si signal observed. This distance gives roughly the lateral diameter of the excitation volume in the substrate. The penetration depth was estimated by a Monte-Carlo simulation to be on the order of 1.6 μm at 15 keV [Drouin and Hovington, 1997].

Because of the complicated dependence of the Al/Si signal on the sample geometry, it is best to calibrate the Al/Si signal to the amount of Al in the excited volume using Al lines of various known thicknesses. In order to calibrate the Al/Si signal, measurements were carried out on 0.5 μm wide Al lines of 100, 200, 300, and 400 nm thickness, as shown in Figure 3.9. It was found that the signal was quite linear with the Al thickness, so that a constant was used to convert the difference Δs between the

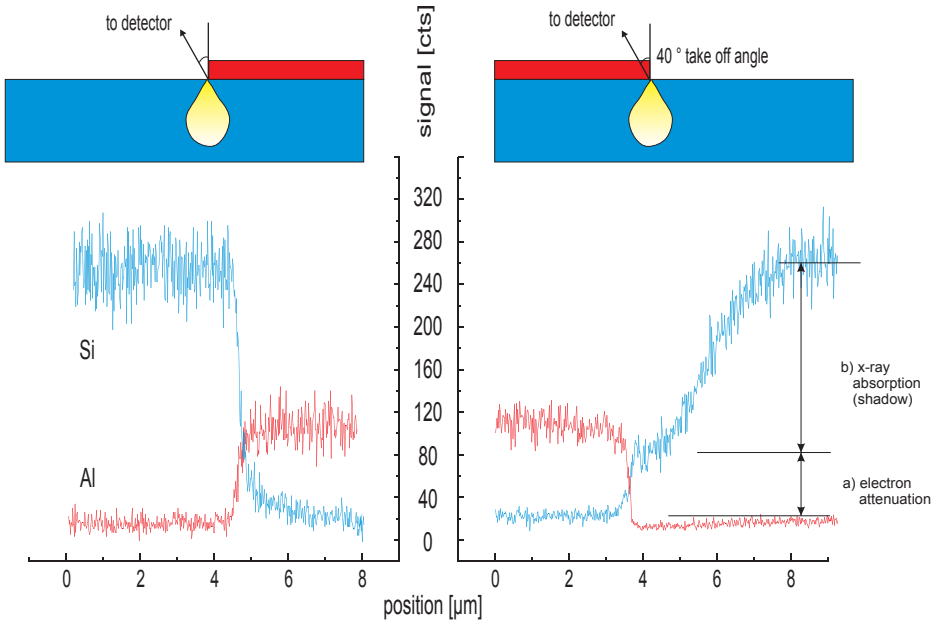

Figure 3.8: Effect of activation volume geometry on EDX signal distribution: the line-scans at 15 keV across an edge of an 400 nm thick Al film show the shadow effect towards the detector. Take off angle (detector position) was 40°.

measured Al/Si signals into an equivalent thickness change ($\Delta t = 20.4 \cdot \Delta s$). Finally, this number was subsequently converted to displacement of the cathode edge, assuming uniform depletion.

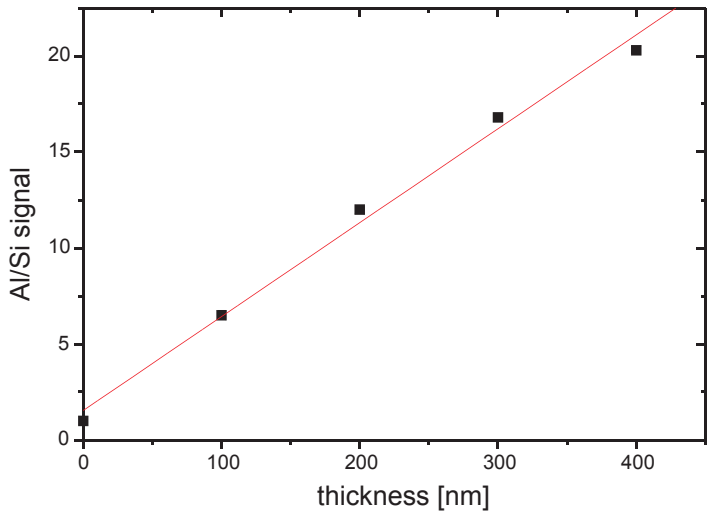

Figure 3.9: EDX X-ray signal calibration to line thickness: Al/Si signal ratio as function of line thickness. Width of the line was 0.5 μm.

Edge displacements as small as 100 nm and a change of ∼15% in the number of atoms in the excited volume (0.2 μm^3) could be measured with this technique. This corresponds to a minimum change in the number of Al atoms of $\sim 2 \cdot 10^9$ that could be detected. The spatial resolution to measure uniform edge displacements

is less than direct electron imaging (described below). However, the EDX mapping technique is advantageous in determining the exact amount of displaced atoms when the displacement is not uniform, or leaves material behind.

3.4.2 Drift measurements by electron imaging

Direct observations of damage in passivated samples were performed by backscattered electron imaging, which is capable of revealing depleted areas, even if they are covered by a passivation provided a sufficiently high accelerating voltage is used. For this work either a Camscan or a JEOL microscope was used [Camscan, 1993, JEOL35, 1970]. The first was operated at maximal 40 kV the latter at 35 keV electron accelerating voltage. An example of a passivated interconnect with depletion at the cathode end underneath the passivation is shown Figure 3.10. Backscattered electron imaging

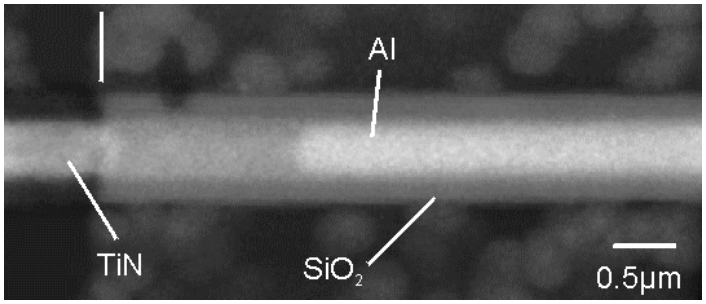

Figure 3.10: Backscattered electron image of a depleted cathode end of passivated 0.5 μm wide segment after testing at 250°C. Due to the different backscattering efficiency of Al, TiN and the passivation, these materials can be clearly distinguished.

(BEI) showed the dimension of voids underneath the passivation more clearly than secondary electron imaging. In particular, if voids were located near the sidewall, it was difficult to determine their size exactly. The volume of each void was estimated by measuring the area in the SEM and assuming a columnar structure. In most cases the voids spanned the width of the line hence the length was recorded; in the other cases the recorded length corresponded to the estimated length should they have spanned the line. Voids smaller than roughly 50 nm could not be detected with this technique.

In the case of unpassivated samples, observations were performed by secondary electron imaging. The void sizes were determined in the same way as with backscattered electron imaging. The resolution was higher than in passivated segments, such that voids as small as roughly 30 nm could be observed.

3.4.3 Drift measurements by resistance

Since the interconnects can be treated as a parallel circuit of the TiN and the Al, the resistance increase induced by depleting Al from the TiN is proportional to the displaced length. In order to correlate the resistance increase measured with the actual Al displacement, a calibration using electron imaging has been performed, as shown in Figure 3.11. The sample was a single, unpassivated, 800 μm long and 0.5 μm wide pure Al segment, connected to a contact pad (reservoir end). From the calibration, the edge displacement Δx in μm was calculated from the resistance measurement using $\Delta x = \Delta R/4.65$. In other words, an Al displacement of 0.2 μm converts to 1 Ω resistance change. The electronic resolution of 0.2 Ω is sufficient to measure to 50 nm uniform edge displacement. In the case of very small voids that do not span the width

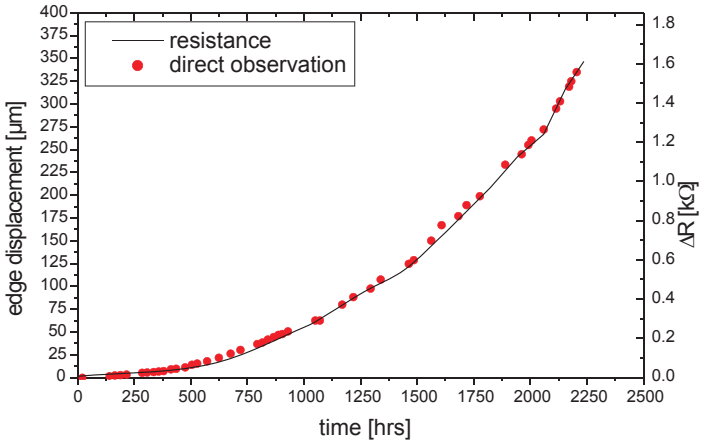

Figure 3.11: Electromigration-induced resistance change due to Al displacement in an unpassivated, pure Al segment at 250°C (solid line). The TiN resistivity obtained from this measurement was 48 $\mu\Omega$cm. The displacement rate increased because the current density has been increased.

of the segment, the resistance change depends on the shape of the void. For example, a very long void that does not span the width of the segment generates a resistance change, which is less than a void of the same volume that does span the width of the segment. In order to accurately determine the displaced volume, direct observations were performed concurrently to the resistance measurements.

When measuring test structures with more than one segment, the measured resistance change yields the total depletion for all segments. In the case of pure Al samples, all segments on a testing structure had the same length, hence the average depletion could be calculated by dividing the total depletion by the number of segments. Information on the drift of individual segments was obtained by direct microscopical observation.

3.4.4 Precipitation measurements by electron imaging

Backscattered electrons at 35 keV were used to image the Al segments under the SiO_2 passivation. Due to the large atomic mass contrast, the formation of Cu-rich precipitates was clearly visible. Figure 3.12 shows an example of a precipitate, imaged with backscattered electrons.

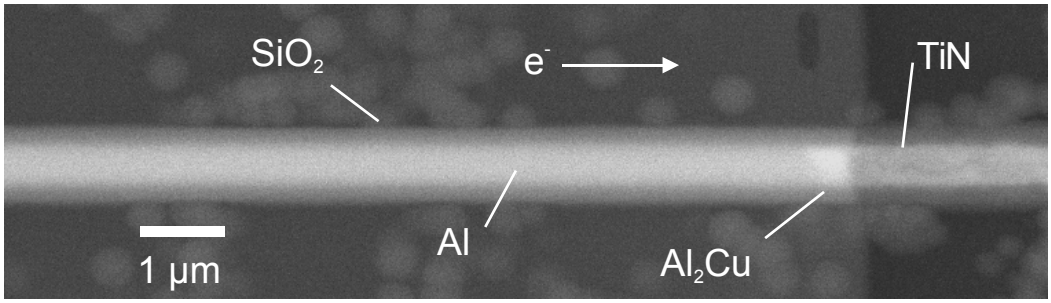

Figure 3.12: Backscattered electron image of precipitate at anode end of a passivated, 0.5 μm wide Al(Cu) segment after testing at 250°C.

The volume of each precipitate was estimated by measuring the area in the SEM and assuming a columnar structure. In most cases the precipitates spanned the width of the line hence the length was recorded; in the other cases the recorded length corresponded to the estimated length should they have spanned the line. Precipitate sizes for segments of the same length were averaged. Precipitates smaller than roughly 50 nm could not be measured.

4

Results

In this chapter the experimental results of sample characterization and electromigration testing are presented. First, the microstructure of the films and lines is presented. The results of the electromigration tests are divided into three sections: measurements of the threshold for damage formation including the statistical distribution of thresholds, measurements below the threshold which include the redistribution of Cu, and measurements above the threshold including the incubation time for void formation. Finally, observations of the electromigration-induced damage morphology are presented.

4.1 Microstructure

In order to characterize the microstructure of the Al films and interconnect segments, FIB imaging was performed. Since it was difficult to resolve the microstructure of the 0.5 μm wide lines by FIB, side-view TEM has been carried out as well. These techniques were also used to assess the shape and dimensions of the interconnects. Backscattered electron imaging in an SEM was used to measure the number and size of precipitates in the passivated Al(0.5 wt%Cu) film before and after annealing. EDX in an SEM was used to show that these precipitates are Cu-rich. Side-view TEM was used to characterize Ti-rich precipitates which were found in both the films and the lines. EDX in a TEM was used to show that these precipitates are Ti-rich.

4.1.1 Film microstructure

Figure 4.1 shows an FIB micrograph of an unpassivated Al(0.5 wt%Cu) film taken from one of the $(200 \cdot 200)\,\mu m^2$ large contact pads on a patterned wafer. In order to reveal the grain structure, the 80 nm SiO_2 and 30 nm TiN capping layers were removed prior to imaging. This was accomplished in the FIB by ion beam sputtering at high current (1000 pA). Next, images of the Al grain structure at a lower beam current (70-150 pA) were obtained. The grain size distribution was determined by applying an

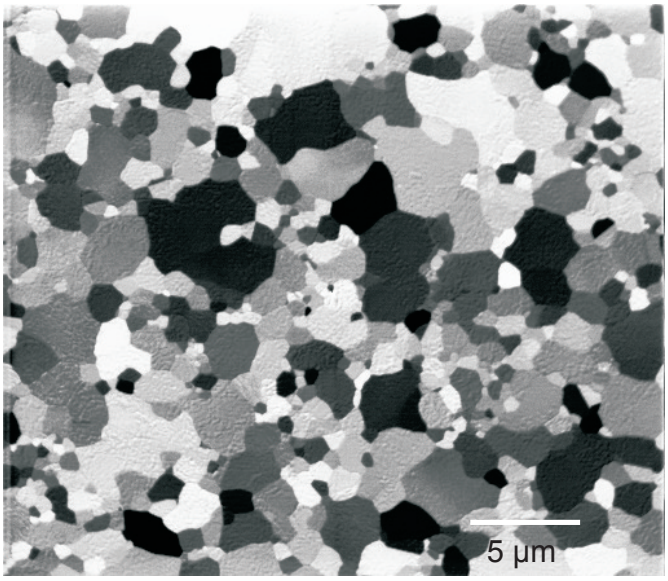

Figure 4.1: FIB image of an unpassivated, 400 nm thick Al(0.5 wt%Cu) film. Tilt angle was 10°.

automatic grain size analysis system [FEI, 1998] to three images of the same location taken at different tilt angles (10°, 15°, 20°). The use of more than one tilt angle increases the chance of distinguishing between the grains. The automatic grain size analysis determines the grain areas and calculates the linear grain size by taking the square root of the areas. The cumulative distribution of linear grain sizes for the film shown in 4.1 is displayed in Figure 4.2. The median grain size d_{50} and the deviation in grain size σ_d were obtained from the data, assuming a lognormal grain distribution.

Passivated Al(Cu) films were inspected by FIB as well. FIB images were taken from the contact pads where the passivation and capping layers had been removed during the fabrication process. The median grain size and deviation were 1.1 μm and 0.8 as determined by the same method as in the unpassivated Al(Cu) film. This value is in reasonable agreement with the median grain size in the unpassivated Al(Cu) films, indicating that the passivation does not cause grain growth.

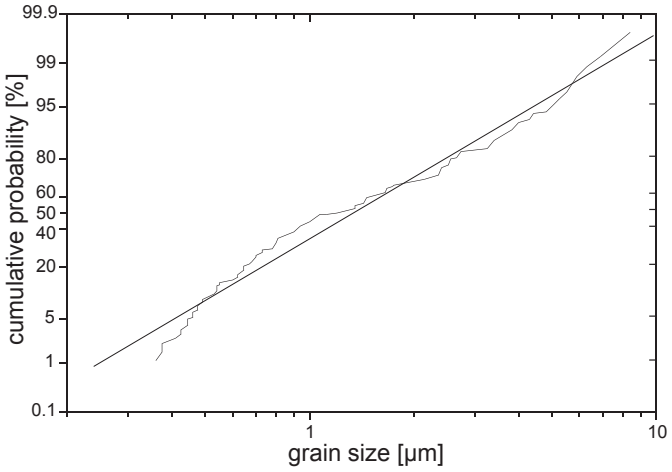

Figure 4.2: Grain size distribution of the Al(Cu) film shown in Fig. 4.1. The straight line shows a fit with a lognormal distribution function. ($d_{50} = 1.24\,\mu$m, $\sigma_d = 0.73$.)

In the cases of passivated and unpassivated pure Al films, FIB inspection revealed that the grains were bimodally distributed. This was not observed in the Al(Cu) films and the reason for the distribution is not clear since the Al films were deposited in the same system with the same parameters as in the Al(Cu) films. The average grain size was roughly $1\,\mu$m for the small grains and $25\,\mu$m for the large grains.

4.1.2 Line microstructure

FIB imaging was used to examine the cross-section of the segments. Figure 4.3 shows the cross-section of a passivated, $0.5\,\mu$m wide Al(Cu) segment. The different materials, Al, TiN, and SiO_2 are labeled in the micrograph. The TiN and Al layer thick-

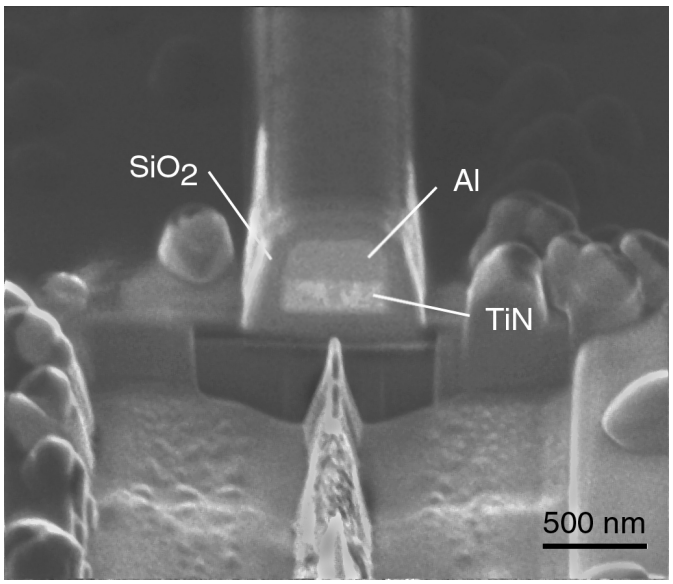

Figure 4.3: FIB cross-section of a passivated, $0.5\,\mu$m wide Al(Cu) segment. Tilt angle 45°, beam current 70 pA. The bubble-shaped structures next to the interconnect are part of the passivation layer.

nesses were 300 and 400 nm, respectively. The Al/TiN cross-section is not perfectly rectangular-shaped, but rather trapezoidal. The profile depends on details of the reactive ion etch process used to pattern the segments. The 200 nm thick SiO_2 passivation layer was conformal. The bubble-shaped structures on the left and right side of the interconnect are part of the passivation layer. The reason for these structures is not clear. The passivation on the segments was uniform, i.e. no bubble structures were present.

Cross-sections of the other sample types, passivated and unpassivated pure Al, and unpassivated Al(Cu) segments showed a rectangularity comparable to passivated Al(Cu) and the dimensions agreed with the nominal values. The passivation on the pure Al segments was conformal, and showed no bubble structures.

The FIB was further used to image the microstructure of the sub-micron lines. Figure 4.4 shows an array of unpassivated, 0.5 μm wide Al(Cu) lines. These arrays were located on the chips which were used for the electromigration tests. Before the microstructure could be imaged, the SiO_2 and TiN capping layers were removed in the same manner as for the unpassivated films (section 4.1.1). A total line length of roughly 120 μm is displayed in the micrograph. Within this range only one possible triple point was detected and the microstructure is almost perfect bamboo. This region was imaged at three different tilt angles (6°, 13°, 40°) to better distinguish between individual grains. The average distance between grain boundaries was 1.4 μm. The

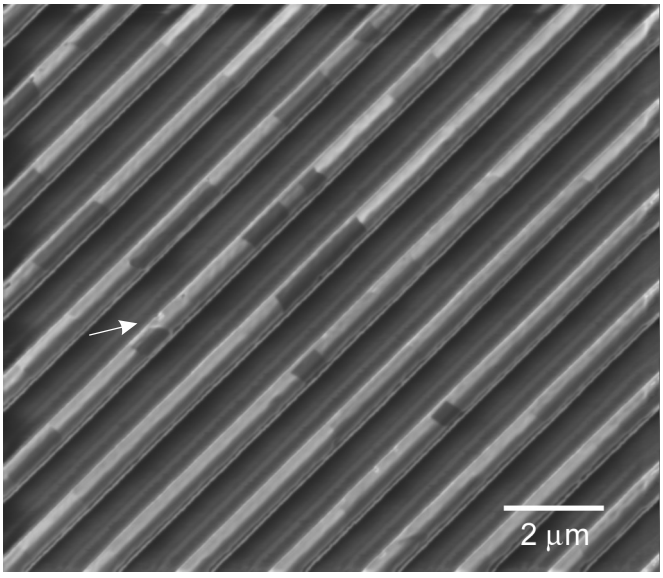

Figure 4.4: FIB image of 0.5 μm wide Al(Cu) lines. Image size was 15 μm, tilt angle was 6°, and the beam current was 130 pA. The point marked by an arrow was possibly a triple point.

FIB preparation does not remove the material uniformly from the top of the lines since the edges are milled down faster by the ion beam leading to a rounded cross-section. Therefore it is possible that triple points near the edge of the line were sputtered away before FIB examination. The ion sputtering effect also limits the total time during which FIB images can be obtained. The measured distances between grain boundaries in the unpassivated Al(Cu) segments (Figure 4.4) compares reasonably well with the grain size measured in the continuous film (Figure 4.2). Around 10 triple points were found in the film images, when a grid of the same dimensions as the segments in Figure 4.4 was overlayed. If the postpattern anneal had no effect on the microstructure, the same number of triple points would have been expected in the lines. It is known that the microstructure of interconnects can change from polycrystalline to bamboo, when the lines are subjected to postpattern anneals [Walton et al., 1992]. It is concluded that the postpattern anneal removed most of the triple points in the Al(Cu) segments, leading to the almost perfect bamboo microstructure.

For passivated Al(Cu) and unpassivated pure Al, side-view TEM of the microstructure was performed. The structure of a passivated Al(Cu) segment is shown in Figure 4.5 and of unpassivated pure Al in Figure 4.6. In the pure Al case, the intercon-

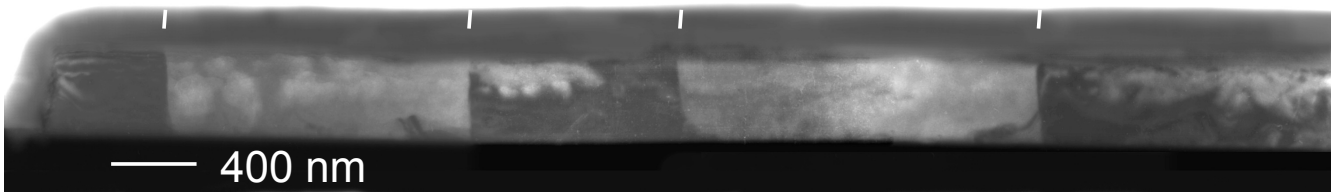

Figure 4.5: Side-view TEM micrograph of a 0.3 μm wide passivated Al(Cu) segment imaged at 1 MeV. Grain boundaries are marked above the segment.

nect has been thinned by FIB to a thickness of roughly 0.2 μm. The Al(Cu) was not subjected to FIB treatment. The total length inspected was roughly 50 μm in both cases. By tilting the sample and observing the contrast change of individual grains in the microscope, the grain boundaries could be identified. The TEM micrographs show that the grain boundaries are perpendicular to the Al segment direction. The average distance between grain boundaries was 1.3 μm in the case of Al(Cu) which is in reasonable agreement with Figure 4.4. No lines or contrast changes indicating triple points were observed in the pure Al and Al(Cu) segments inspected. For the 0.3 μm wide lines, the number of triple points that can be expected from the film images, is

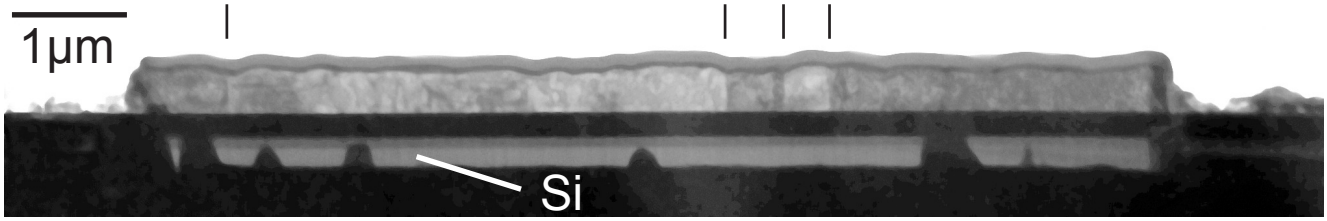

Figure 4.6: Side-view TEM micrograph of a unpassivated, 10 μm long, and 0.3 μm wide pure Al segment. Grain boundaries are marked above the segment. The different layers visible are TiN/Al/TiN/Ti/SiO_2/Si from the top. Electron energy was 120 keV.

around 2-3 within the 50 μm line length, if the postpattern anneal had no effect. It is concluded that most triple points were annealed out without a significant change in grain size. The average grain boundary distance in pure Al was 1.5 μm for the small grains which agrees with the grain size observed by FIB. In one incident, a grain of 30 μm size was also observed by side-view TEM indicating the bimodal grain size distribution in these films.

4.1.3 Precipitates

According to the equilibrium phase diagram, Θ-phase Al_2Cu precipitates are expected in Al(0.5 wt%Cu) alloys below a temperature of 320°C [Massalski, 1990, p. 141]. However, after sample fabrication, no precipitates were observed by backscattered electron imaging in the contact pads or in the sub-micron wide segments of the passivated Al(Cu) wafer. After annealing a sample of the wafer at 250°C, no precipitates were observed in the 0.5 μm wide lines within 1000 μm length inspected. However, precipitates were found in the contact pads after annealing. Figure 4.7 shows a portion of a (200·200) μm^2 large contact pad that had been annealed at 250°C for roughly 1300 hours. No electrical current had been applied to the pad. EDX in the SEM was used to confirm that the precipitates contain Cu. The precipitates in the pad were imaged using backscattered electrons revealing a total of 120 precipitates, which corresponds to a number density of roughly 0.003/ μm^2. The area fraction of the precipitates was roughly 0.2 %. Assuming that the precipitates are the Θ-phase and columnar, they account for roughly 0.16 wt % Cu, which is close to what is expected from the equilibrium solubility of ~0.2 wt% at 250°.

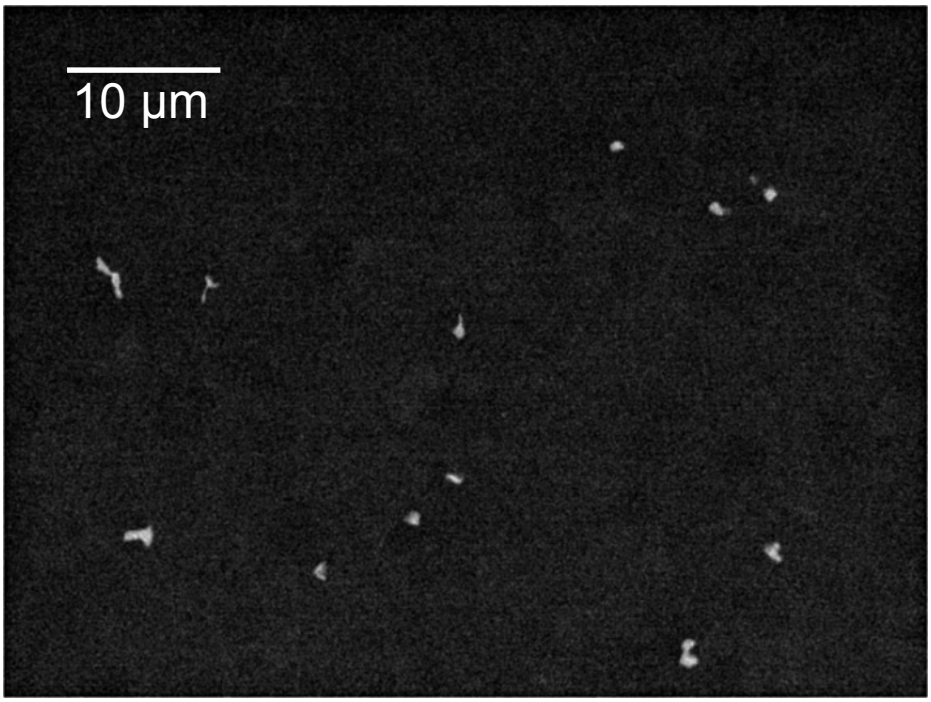

Figure 4.7: Backscattered electron image of an Al(Cu) film annealed for 1300 hrs at 250°C. The Cu-rich precipitates show up bright, due to the higher backscattering efficiency of Cu.

Beside the Cu-rich precipitates, small Ti-rich precipitates were observed in the lines. A typical side-view TEM image of these precipitates is shown in Figure 4.8. The Ti-based particles, labeled $TiAl_x$ in the micrograph, were always located at the bottom Al/TiN interface. The precipitate diameter was usually on the order of 20-60 nm. EDX in a TEM has confirmed that these particles are Ti-rich. The exact stoichiometry was not analyzed. These particles are presumably formed by reaction of Ti from the TiN barrier layer with the Al [Besser et al., 1997].

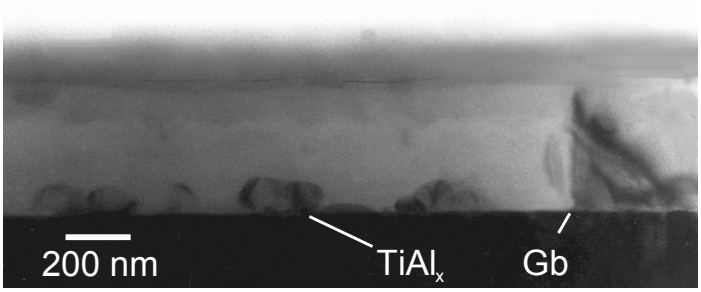

Figure 4.8: Side-view TEM micrograph of a passivated Al(Cu) segment. A grain boundary is labeled "Gb". The microscope was the AEI (EM7) operated at 1 MeV.

4.2 Threshold product

To determine the threshold product for damage formation, the cathode ends of segments were examined by backscattered or secondary electron imaging during electromigration testing. To detect hillock formation, the anode ends were inspected by electron imaging. As soon as a void was detected, the segment was considered to be damaged. In the case of unpassivated Al(Cu), the cathode ends were also inspected for voids by EDX mapping in the SEM.

4.2.1 Threshold distribution in unpassivated pure Al

The dependence of the threshold product on the segment length was investigated on a set of unpassivated, pure Al segments. All segments (23 of 30 μm long segments, 14 of 50 μm long segments, 10 of 75 μm long segments, 8 of 95 μm long segments, 4 of 195 μm long segments) were located on a single die. They were connected in series, and tested simultaneously. The current density was increased in steps of typically 0.02 MA/cm^2 until each individual segment started to drift. At each current density, the current was held for at least 24 hours, which is significantly longer than the expected incubation times for void formation in the 195 μm long segments at current densities greater than 0.4 MA/cm^2 (to be presented in section 4.4.1). At the current densities applied for 195 μm long segments, the expected incubation times are on the order of 20 hours. The experiment was terminated after half of the 30 μm long segments had begun to drift.

Figure 4.9 shows the cumulative distribution of threshold current densities for all segments. The plots for the various segment lengths follow straight lines, showing that they are approximately normally distributed. The lines are best linear fits to the data. The threshold products were calculated and their cumulative distributions fitted to straight lines. From these fits the mean values and deviations in the threshold products were determined. The median critical current densities for drift were roughly the same as the means.

The means and deviations in threshold products are shown as a function of segment length in Figure 4.10. The threshold product $(jL)_c$, which is a measure of the maximum stress gradient that can be sustained by the segment, is fairly constant with segment length with an average value of 4670 A/cm. However, the deviation in threshold product exhibits a systematic decrease as the segment length increases.

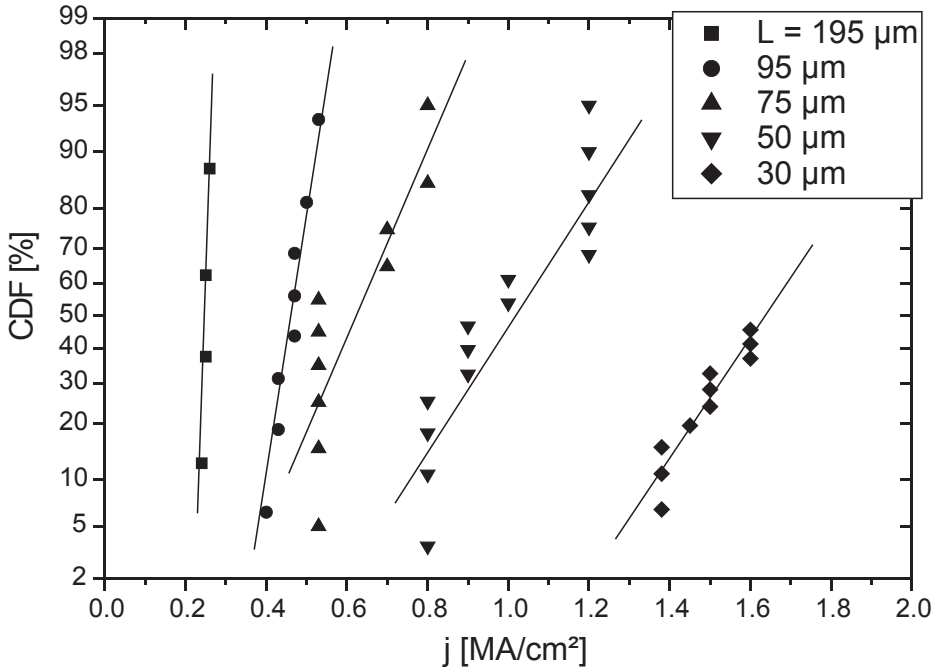

Figure 4.9: Normal plot of the cumulative distribution of critical current densities for unpassivated pure Al segments of length L. Test temperature was 250°C.

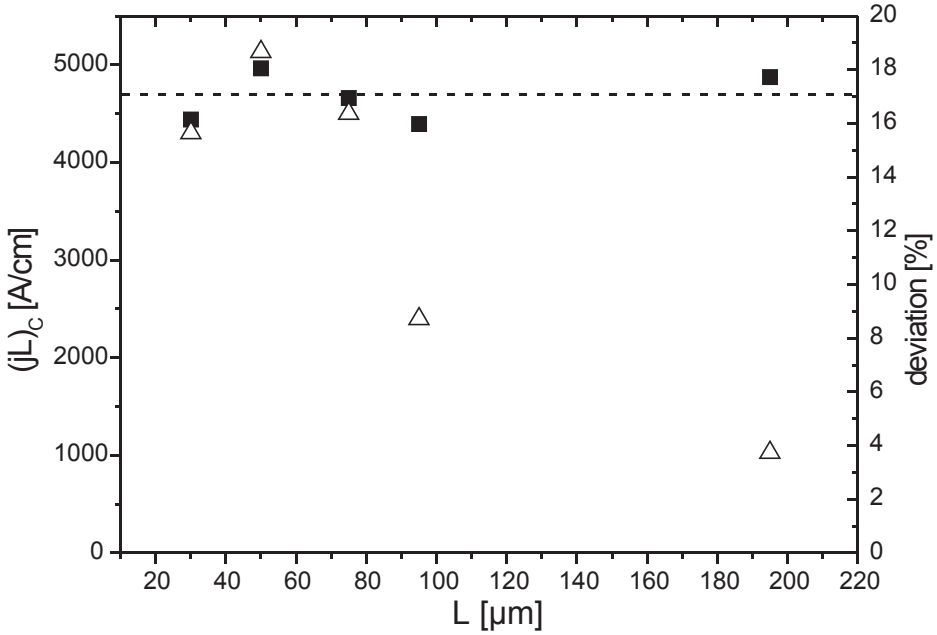

Figure 4.10: Mean threshold product (squares) and relative deviation (triangles) in threshold product extracted from the threshold distributions as a function of segment length. The relative deviation was calculated by dividing the absolute deviation by the mean. The average threshold product is indicated by the dashed line.

4.2.2 Threshold product as a function of sample type

The threshold product has been measured for different sample types in order to assess the influence of Cu and the passivation layer. In the case of passivated and unpassivated Al(Cu), a range of different segment lengths between 5 μm and 100 μm were tested simultaneously, since these segments were located on the same test structure. The currents applied to these segments were 1.5, 2, and 3 MA/cm^2. The shortest segment that depleted, as well as the longest segment that did not deplete at a given current density were recorded. The test procedure for unpassivated pure Al was described in the previous section. Passivated, 100 and 200 μm long pure Al segments were tested in series at 250°C and 0.8 and 1.0 MA/cm^2.

Figure 4.11 shows the summary of threshold products for the different sample types. For unpassivated segments, damage was observed at both ends of the segments. It could not be distinguished whether voids or hillocks formed first. On the other hand, two regimes were observed in passivated segments. At intermediate current densities, a void formed and grew to saturation, but no hillocks were generated. At even higher current densities, the passivation eventually cracked, a hillock formed, and further depletion took place. The passivation increased the threshold for void

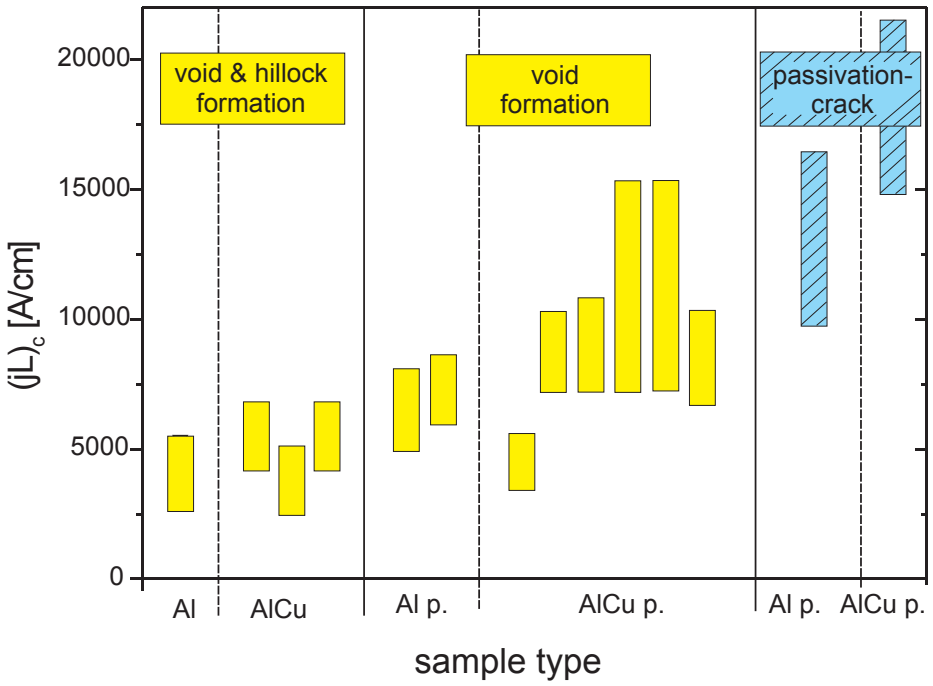

Figure 4.11: Summary of threshold products obtained for various sample types. Temperature was 250°C for Al, passivated Al, and passivated Al(Cu). In the case of unpassivated Al(Cu) the test temperature was 200°C.

formation in both Al and Al(Cu). The value for passivated Al(Cu) was roughly 1000-2000 A/cm higher than for passivated pure Al. The value for unpassivated Al(Cu) was roughly 500 A/cm higher than the one for unpassivated pure Al. The test temperature for unpassivated Al(Cu) was 200°C. However, the temperature dependence of the threshold product is known to be small [Straub, 2000], therefore the datapoints were included in Figure 4.11.

4.3 Below threshold

4.3.1 Al redistribution

In order to confirm the absence of depletion in sub-threshold segments, the EDX mapping technique was used to measure atomic concentrations at the cathode end of Al(0.5 wt%Cu) segments. Electromigration testing of unpassivated, 0.5 μm wide and 5 μm long Al(Cu) segments was performed at 200°C and 2 MA/cm^2 in air. The testing was interrupted to perform EDX measurements and SEM inspection. Figure 4.12 shows the Al/Si signal distribution of the cathode end of a segment after various times of electromigration testing. No depletion was observed by EDX mapping or SEM inspection within the experimental resolution.

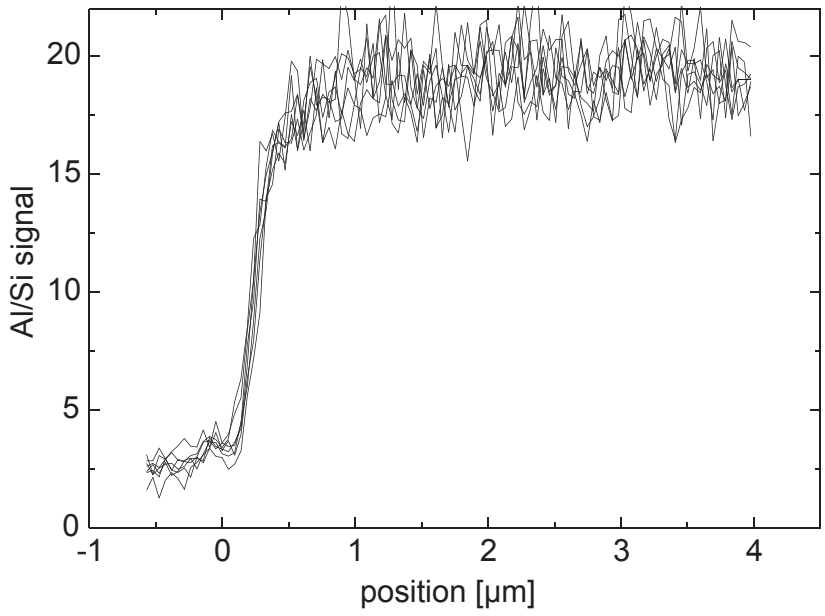

Figure 4.12: Al/Si signal at the cathode end of an unpassivated, 0.5 μm wide and 5 μm long Al(Cu) segment after 0, 19, 40, 67, 99, and 136 hours of testing at 200°C and 2 MA/cm^2. No evidence of voiding or any form of Al depletion was found.

4.3.2 Cu redistribution

The growth and dissolution of electromigration-induced precipitates in passivated, 0.5 μm wide Al(0.5 wt%Cu) segments were measured *in-situ* in a SEM using backscattered electron imaging. Electromigration testing was performed at 250°C and for current densities between 0.2 and 1.5 MA/cm^2. In order to minimize sample to sample variations, all experiments were performed on a single set of Al segments of lengths between 5 and 100 μm (4 of 5 μm length, 5 of 10 μm length, 2 of 25 μm length, 1 of 35 μm length, 3 of 50 μm length, 2 of 100 μm length), which were located on the same TiN line. The precipitate lengths were measured in each segment as a function of time and current density. Precipitate sizes for segments of the same length were averaged.

During the experiments, the electrical current was used to sweep the Cu solute to the anode ends of the segments where *single* precipitates were formed. Then the current direction was reversed and the Cu redistributed. A typical example of redistribution in 100 μm long segments as a function of time after switching the current direction is shown in Figures 4.13 and 4.14. The precipitation and dissolution upon current reversal can be divided into a *saturation stage* and a *constant drift stage*.

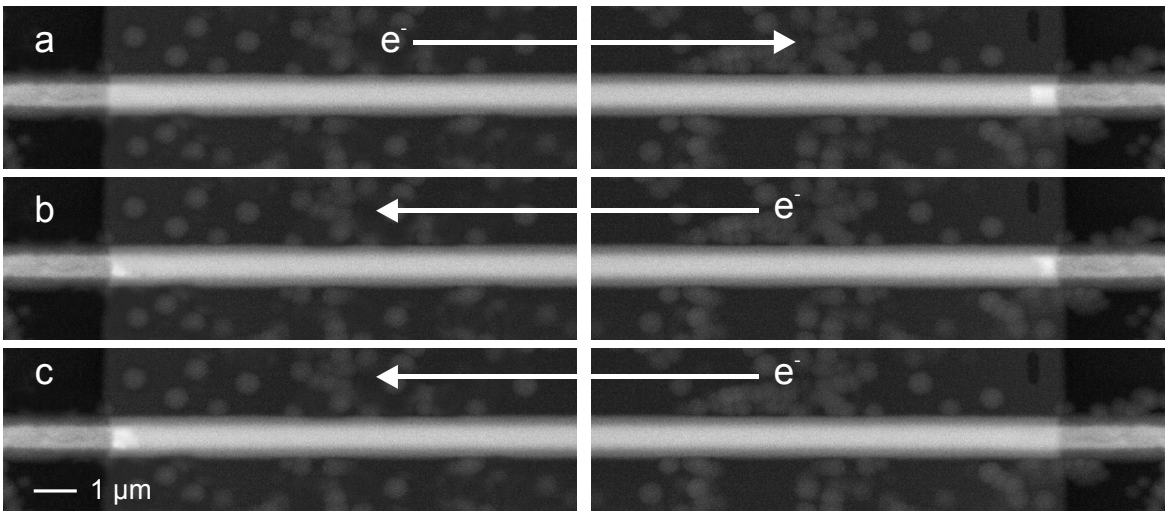

Figure 4.13: Precipitate formation and dissolution during current reversal at 250°C and 0.5 MA/cm^2. Before the current was reversed the precipitate grew to saturation (a). After current reversal, this precipitate began to dissolve, and a new formed eventually at the opposite end (b). Eventually, the old precipitate completely dissolved, and the new precipitate grew to saturation (c).

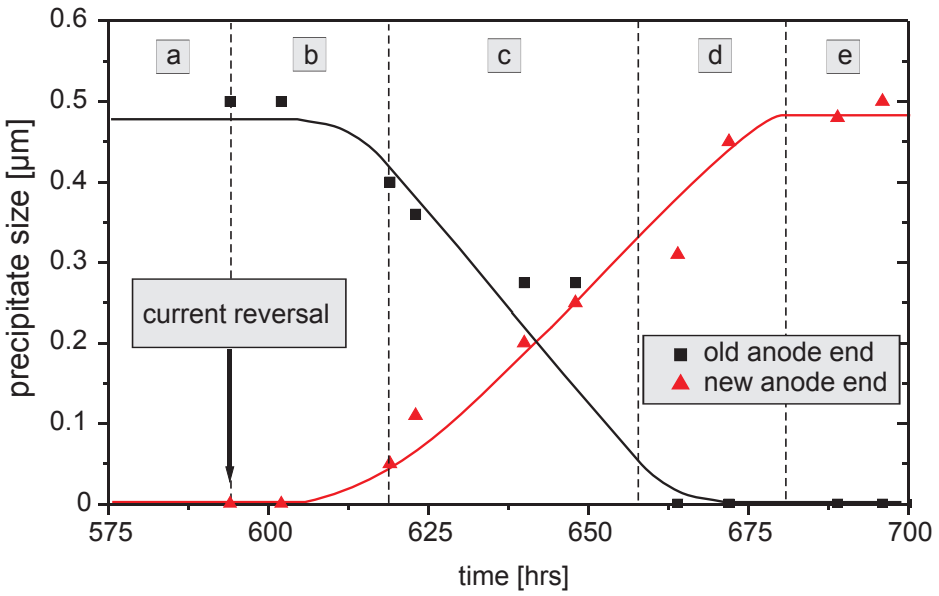

Figure 4.14: Dissolution and growth of a precipitate at the two ends of 100 μm long segments after current reversal. The data was averaged from two 100 μm long segments tested in series. Testing was performed at 250°C and 0.5 MA/cm^2.

After sufficient time at a given current density, the precipitates at the anode ends reached steady state and ceased to grow further (*saturation stage*) (Figure 4.13, label a, and old anode end in Figure 4.14, label a). When the current was reversed, the precipitate began to dissolve (Figure 4.14, label b). For low currents and short segments, the precipitate did not completely dissolve and no new precipitates were formed. For higher currents and longer segments, a new precipitate formed at the opposite end of the segment (new anode end), and dissolution of the old and growth of the new precipitate then proceeded at a constant rate *(constant drift stage)* (Figure 4.13, label b, and 4.14, label c) until the old precipitate had completely dissolved (Figure 4.13, label c and 4.14, label d). Once the old precipitate had dissolved, the new precipitate grew further until it also reached steady state (*saturation stage*) (Figure 4.14, label e). The final size of the precipitates was the same as that at the previous anode end of the segments before current reversal. This cycle was repeated several times at various current densities, and in all cases a single precipitate was observed to form at or near the anode end.

In most cases, the precipitates were located directly at the end of the segments. In some cases precipitates formed within a few microns from the anode end, as shown in the example in Figure 4.15. This precipitate is located at the intersection of a grain boundary with the bottom Al/TiN interface. In some experiments, it was observed

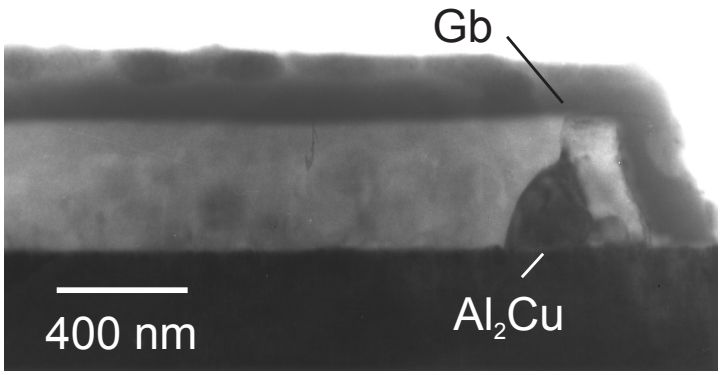

Figure 4.15: Side-view TEM image of the anode end of a passivated, 25 μm long segment after electromigration testing at 250°C and 0.5 MA/cm^2. The precipitate formed roughly 0.5 μm away from the anode end at a grain boundary.

that the precipitate location was *different* from the location during the previous current cycle. This suggests that precipitate formation was not entirely determined by the same microstructural feature in the segment. After formation, the precipitates were never observed to migrate during electromigration.

Also, no voids were observed at low current densities, in particular at the locations where precipitates dissolved, indicating that the Cu atoms were somehow replaced with Al atoms during precipitate dissolution, which is similar to observations reported earlier [Shaw et al., 1995]. A void in the Al was only observed at very high current densities. No passivation cracking and hillock formation occurred during the entire experiment.

4.3.2.1 Morphology of electromigration induced precipitates

Side-view TEM was performed to characterize typical electromigration-induced precipitates, as shown in Figure 4.16. In order to determine the phase of this precipitate, selected area diffraction (SAD) was performed. The diffraction pattern is shown in Figure 4.17. The SAD pattern was consistent with a tetragonal Θ-Al_2Cu structure, which is in agreement with results in the literature [Marcus and Bower, 1997, Colgan and Rodbell, 1994].

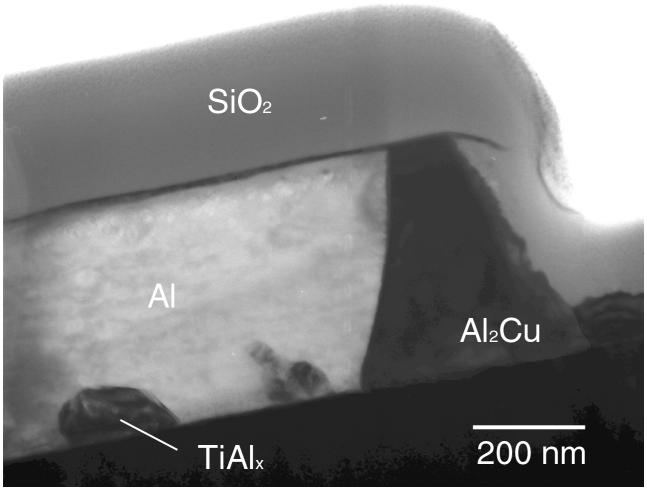

Figure 4.16: Side-view TEM image of a precipitate at the end of a passivated, 35 μm long Al(Cu) segment after testing at 250°C and 1.5 MA/cm^2. The segment width was thinned by ion milling in the FIB to a thickness of roughly 300 nm. The precipitate appears dark due to higher electron attenuation of Cu. EDX confirmed that the small precipitate labeled by $TiAl_x$ was Ti-based.

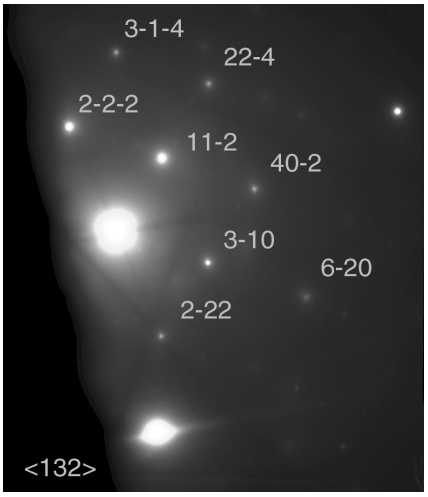

Figure 4.17: SAD pattern of the Al_2Cu precipitate shown in Figure 4.16. The diffraction spots that were considered for structure identification are labeled in the image. The lattice spacings of the Θ-Al_2Cu phase were identified with an error of smaller than roughly 3%. The zone axis was $< 132 >$, beam energy was 200 keV, and the camera length was 80 cm.

4.3.2.2 Saturation stage

Precipitate sizes at saturation for the different segment lengths are summarized in Figures 4.18 and 4.19. The measured precipitate sizes scale roughly linearly with the segment length (Figure 4.18) and are only weakly dependent on the current density (Figure 4.19). The measured precipitate sizes are close to the sizes that are expected if all Cu were in the precipitates (dashed line in Figure 4.18). In this case, the precipitate sizes can be expressed as $\Delta L = c_0/c_p L$ (see section 5.2.1), where L is the segment length, c_0 the initial Cu concentration, and c_p is the Cu concentration in the precipitate.

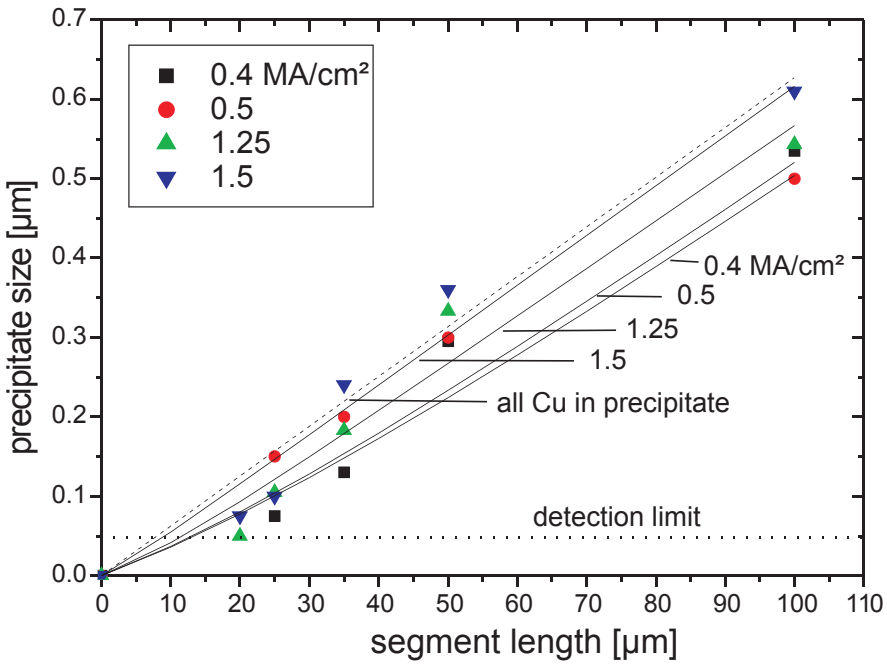

Figure 4.18: Precipitate sizes at saturation as a function of segment length for various current densities. The solid lines show a fit with a model presented in chapter 5. The dashed line indicates the precipitate sizes that are expected if no Cu is in solution. The dotted line in the graph indicates the minimum measurable precipitate size.

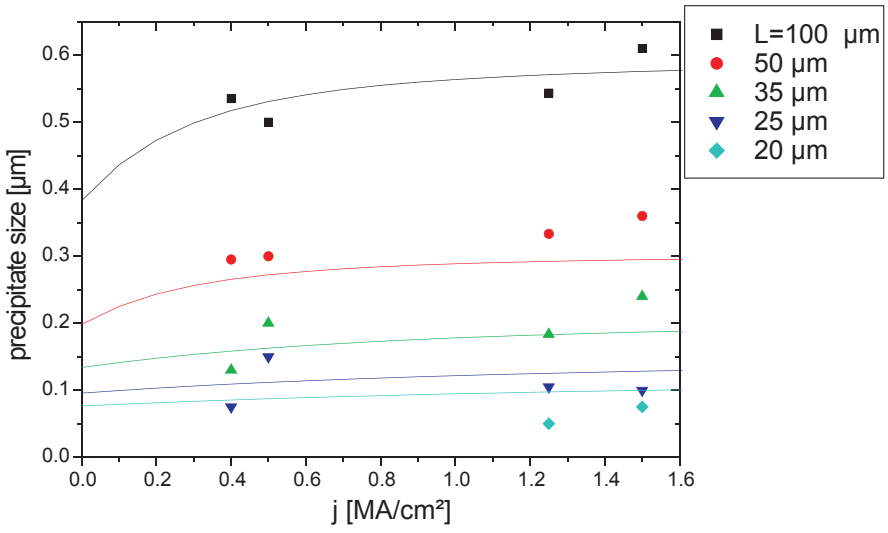

Figure 4.19: Precipitate sizes at saturation as a function of current density for the different segment lengths.

4.3.2.3 Conditions for precipitate formation

Figure 4.20 shows a map of the segment lengths and current densities that were investigated. Prior to electromigration testing, no precipitates were detected in any of the interconnect segments. During the electromigration experiments no precipitates were observed in short segments (5 and 10 μm), indicated by x's in Figure 4.20. This is consistent with the detection limit, indicated by the dashed lines in Figures 4.18 and 4.20. In all longer segments, a single precipitate was observed to form at or near the

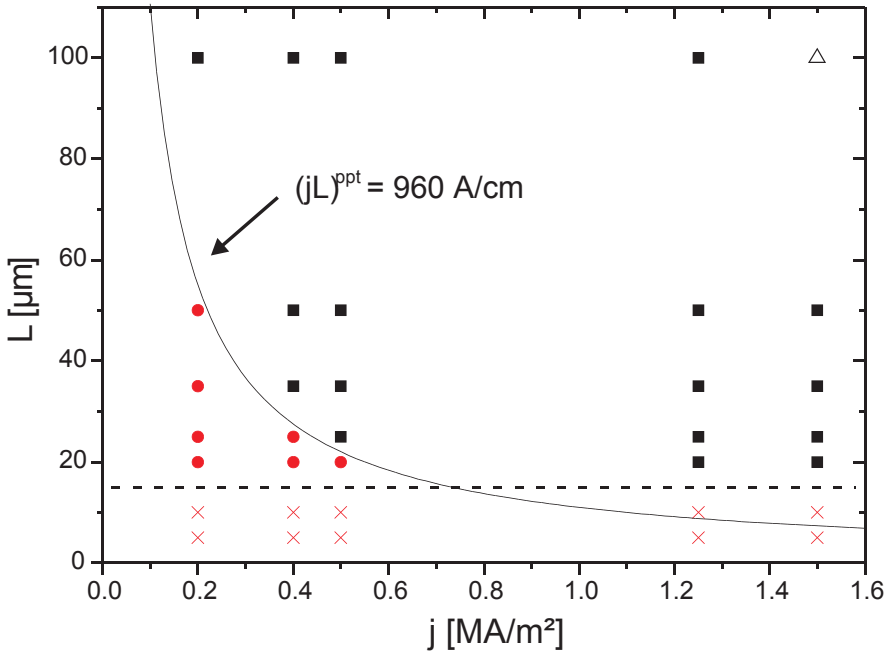

Figure 4.20: Map of segment lengths and current densities. Squares correspond to precipitate observation at the new anode end. In the cases indicated by circles, no precipitate was observed at the new anode end, although the old precipitate was still present at the new cathode end. The triangle refers to the observation of a void. The dashed line corresponds to segment lengths below which the maximum precipitate sizes are too small to be detected.

anode end of each segment. However, when the current was reversed more complex behavior was observed. Only at sufficiently large currents, the precipitate dissolved completely and a new precipitate formed at the new anode end (squares in Figure 4.20). If the current density was too low or the segment length too short, no precipitate was observed at the new anode end (circles in Figure 4.20), and the precipitate at the old anode end was not completely dissolved. This behavior did not change even after 150 hrs of constant current stressing, and the dissolution of the cathode end

precipitates did not further progress. The two regions divided by $(jL)^{ppt} = 960\,\mathrm{A/cm}$ indicate where precipitates formed.

4.3.2.4 Constant drift stage

Once precipitates were present at both ends of the segments, the rates of dissolution and precipitation were equal and roughly constant. The rates for the various current densities were determined by fitting linear functions to the precipitate size vs. time data. For short segments (20, 25, and 35 μm), not enough data was acquired to determine the kinetics of growth and dissolution. The rates for the 50 and 100 μm long segments are shown in Figure 4.21. For higher current densities, fewer data-points during the constant drift stage were recorded, thus the scatter is increased. The rates scale roughly with current density and show no apparent dependence on the segment length. A precipitation and dissolution rate of 3.9 nm/hr (or $8 \cdot 10^{-4}$ μm^3/hr) at 0.25 MA/cm^2 was measured, which is in good agreement with previously reported values (between $3 \cdot 10^{-4}$ and $1.3 \cdot 10^{-3}$ μm^3/hr at 0.24 MA/cm^2 and 260°C) [Shaw et al., 1996].

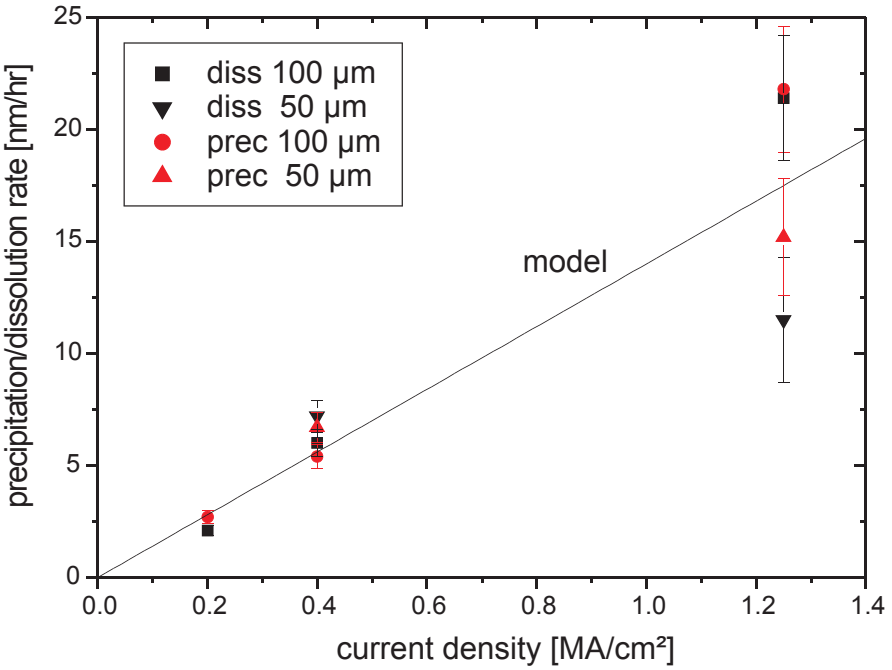

Figure 4.21: Dissolution and precipitation rates as a function of current density. The rates were determined during the *constant drift stage* when precipitates were located at both ends of the segments.

4.3.2.5 Back-diffusion of Cu

In one experiment, the segments were stressed at a high current density of 1.25 MA/cm^2 until the precipitates at the anode ends reached saturation. Then, the current was turned off and the precipitates began to dissolve. The average precipitate size in each segment length is shown as a function of time in Figure 4.22. Even after 150 hours, none of the precipitates had completely dissolved, nor had any new precipitates formed.

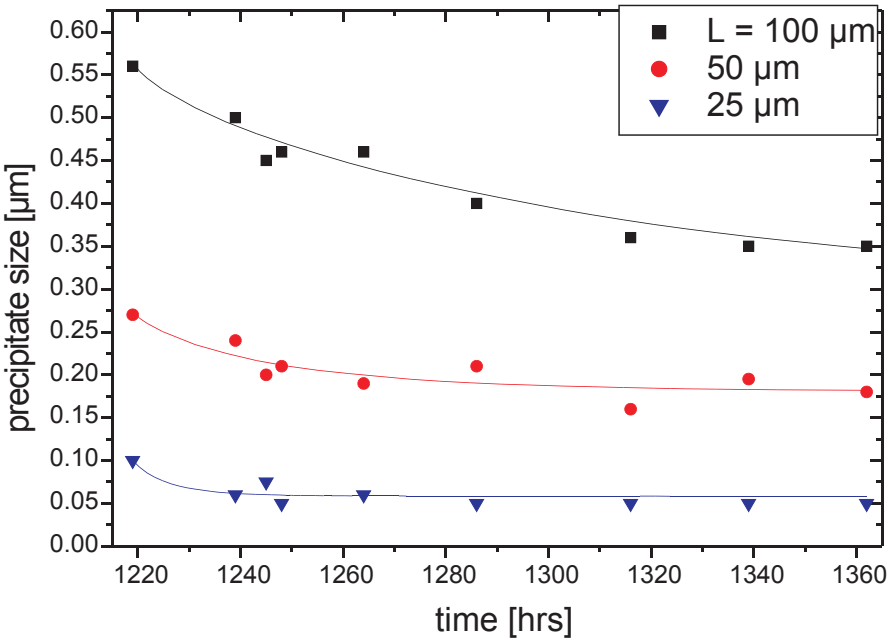

Figure 4.22: Dissolution of precipitates after turning the current off at 1220 hours which had been previously grown to saturation at 1.25 MA/cm^2 and 250°C.

4.4 Above threshold

In this section, the electromigration behavior of Al segments *above* the threshold for damage formation is examined. After sufficient time, application of a super-critical current leads to stresses, which exceed the threshold stress in a given interconnect segment. This results in damage in the form of material depletion at the cathode end and accumulation at the anode end.

Electromigration-induced depletion was measured in unpassivated, Al(Cu) segments by the EDX mapping technique, and the accumulation observed by SEM inspection (compare section 4.3.1). Electromigration testing of unpassivated, 0.5 μm wide and 20 μm long Al(Cu) segments was performed at 200°C and 2 MA/cm^2 in air. The testing was interrupted to perform EDX measurements. Figure 4.23 shows the Al/Si signal distribution of the cathode end of a segment after various times of electromigration testing. The segment was depleted uniformly from the cathode end. By SEM inspection, it was observed that at the anode end of the segment, Al was accumulated and a hillock formed.

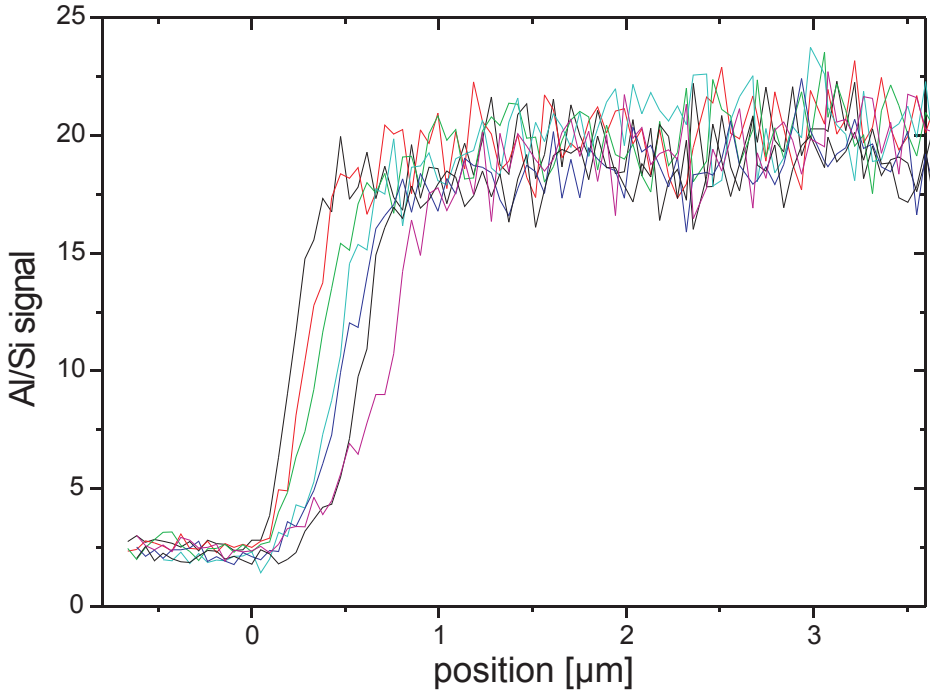

Figure 4.23: Al/Si signal at the cathode end of an unpassivated, 0.5 m wide, and 20 μm long Al(Cu) segment after 0, 19, 40, 67, 99, 117, 136 hours of testing at 200°C and 2 MA/cm^2. Zero is the position of the initial cathode end of the segment.

The depleted length as a function of time, referred to as drift, can be used as a measure of material transport due to electromigration, as introduced by Blech, 1976. The results are henceforth given in terms of depleted length. Generally, the drift behavior of a segment of length L can be divided into

- an incubation period,
- motion at a constant drift rate (pure Al, large L), or
- at an increasing drift rate ((Al(Cu), large L), and
- saturation (L comparable to threshold length L_c).

The results presented in the next sections are organized by these damage stages.

4.4.1 Incubation time

The incubation time to form a void was measured in both passivated and unpassivated 800 μm long pure Al segments, which were connected at the anode end to a large contact pad. Electromigration testing was performed *in-situ* in an SEM at 250°C and current densities between 0.04 and 0.8 MA/cm^2. Because it is difficult to detect very small voids, the resistance was measured simultaneously. The resistance change as a function of time was used to determine the incubation times.

In the case of the unpassivated segment, the experiment was performed only once. An opening in the interconnect or void, formed roughly 1 μm away from the cathode end, and then uniform depletion took place. In the case of the passivated segment, the measurement was performed several times. This was possible because in contrast to the unpassivated segment, the void could be closed by reversing the current. The void always formed at the same place 2 μm away from the cathode end. After it spanned the width of the segment, uniform depletion was observed. This motion was continued at a constant current density until roughly 5 μm was uniformly depleted, before reversing the current. No residual material in the depleted region was found by SEM inspection. The remaining 2 μm Al at the cathode end neither migrated nor changed its shape. After reversing the current the void completely closed up, and no damage could be observed. By reversing the current direction again, a void formed again at the same position, and subsequent uniform depletion occurred again. This cycle was repeated 7 times at various current densities. Using a single segment to measure the incubation times is advantageous, because sample to sample variations are minimized.

Figure 4.24 shows a characteristic resistance measurement as a function of time. The left part of the Figure schematically shows the cathode end as it was observed in the microscope. At $t = 0$ a current of $0.15\,\mathrm{MA/cm^2}$ was applied to the sample. No voids were present initially nor after 4 hours of testing (time a). After 10 hours, a void was observed in the SEM but only a small resistance increase was measured (time b). After roughly 13 hrs, a sudden increase in resistance occurred. At 16 hours (time c) it was observed that the void spanned the width of the line. From then on, depletion took place uniformly, and the Al end migrated at a roughly constant rate towards the anode accompanied by a constant rate of resistance increase. A resistance increase of $4\,\Omega$ corresponds to $1\,\mu$m of uniform displacement, as indicated by the right-hand axis in Figure 4.24. Assuming a constant growth rate of the void after nucleation, the time of nucleation was defined by extrapolating the resistance change back to the initial value as shown in Figure 4.24.

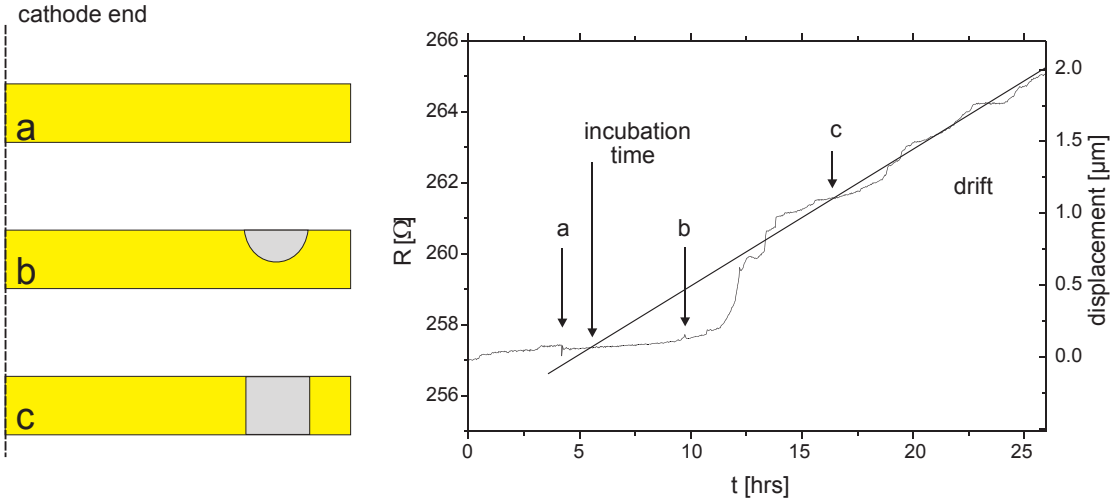

Figure 4.24: Void evolution (shown schematically on the left) and resistance changes (on the right) during electromigration in a passivated Al segment at 250°C and $0.15\,\mathrm{MA/cm^2}$. SEM observations were performed at times labeled by a, b and c. $4\,\Omega$ resistance change corresponds to $1\,\mu$m uniform Al displacement.

The void nucleation times were determined for each current density. The results are summarized in Figure 4.25. At a current density of $0.04\,\mathrm{MA/cm^2}$ no void was observed even after 90 hours, as indicated by the arrow in the Figure. The small numbers in the Figure indicate the order in which the current cycles (void open/close) were performed and the data points taken. There is no obvious trend with time. The nucleation times

decrease with increasing j, roughly as $1/j^2$. The line in Figure 4.25 (slope -2) refers to the modeled incubation time to be discussed in section 5.3.1. The diagram also shows the incubation time in the unpassivated Al segment.

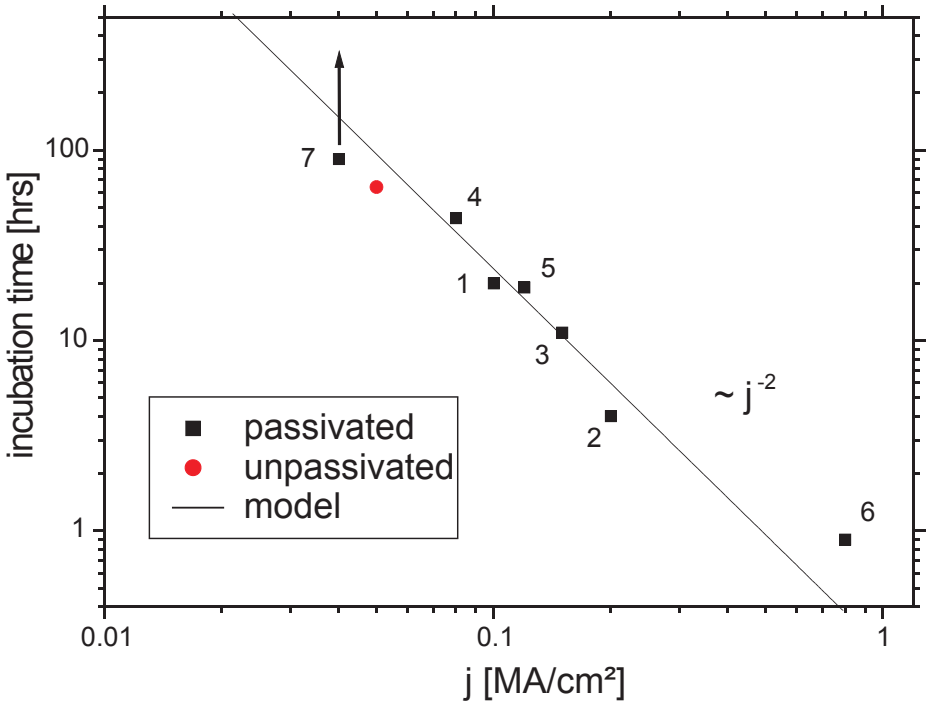

Figure 4.25: Incubation time for void formation in the passivated (squares) and unpassivated (circle) pure Al segment, determined from resistance changes (Figure 4.24). Segment length was 800 μm in both cases. For the lowest current density applied (0.04 MA/cm^2), no void was observed even after 90 hours. The small numbers indicate the order in which the current cycles were performed and the data points taken.

4.4.2 Drift

In this section the influence of the passivation and the Cu on drift is examined. Since the drift depends on the segment length, this section is divided into *long* and *short* segments. Long segments are defined as those which are much longer than the critical length at a given current density. In other words, with sufficiently long segments, the stress gradient-induced back-flux (Blech-Herring model) can be neglected, and the drift velocity is proportional to the current density (equation 1.2). Short segments are defined as those for which the back-flux due to the stress gradient substantially modifies the drift behavior , such that saturation is observed. The subsections are further divided into pure Al and Al(Cu).

4.4.2.1 Long segments: Drift velocity

Pure Al

The dependence of drift velocity on current density was investigated for both passivated and unpassivated long pure Al segments, in order to elucidate the effect of a passivation. The 800 μm long Al segments connected at the end to contact pads, which were used for the incubation time measurements (section 4.4.1), were also used to determine the drift velocities. The results are shown in Figure 4.26. The displacements were determined from changes in the resistance of the segments, and confirmed by direct observation in the SEM. The drift velocities were obtained by fitting linear functions to the displacement vs. time data. In the case of the passivated segment, this fitting procedure was applied to both drift away from the blocking boundary (squares in Figure 4.26) and in the reverse direction (triangles in Figure 4.26). The observations from these measurements can be summarized as follows:

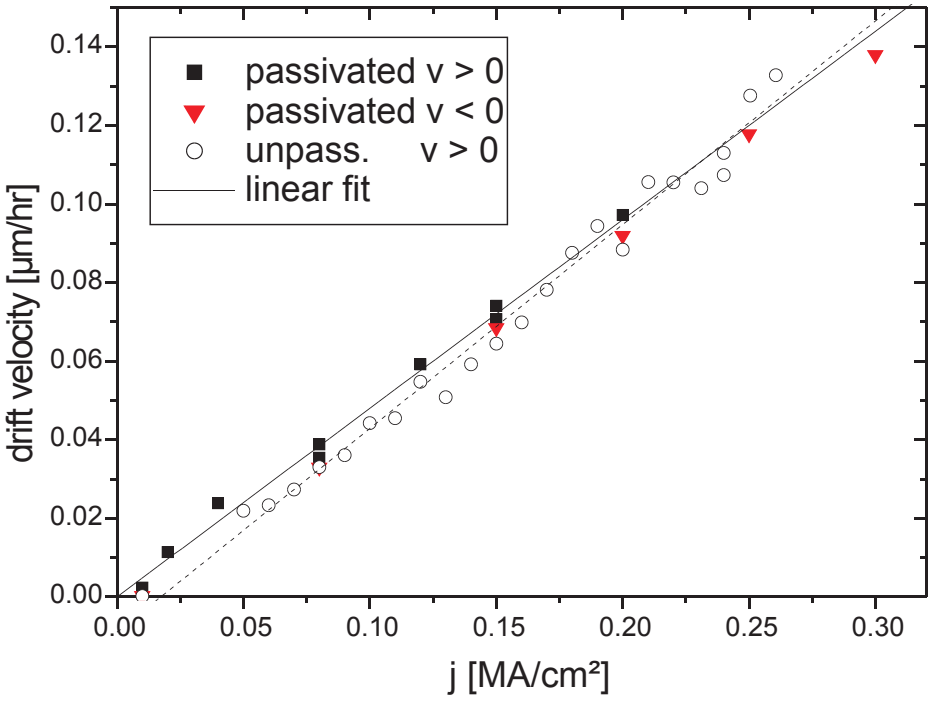

Figure 4.26: Drift velocity as a function of current density in pure Al. Squares refer to drift towards the contact pad in the passivated segment, triangles to the reverse direction. Circles refer to drift in the unpassivated segment (forward direction only). Temperature was 250°C in both cases.

1. The linear fits shown in Figure 4.26 result in an average slope of 0.48 $10^{-10}\,\mathrm{cm}^3/\mathrm{A\ hr}$. This result is used later to determine a value for the product of the effective valence and the effective diffusivity DZ^*.

2. The critical current density j_c is given by the intersection of the linear fits with the abscissa (solid and dashed lines in Figure 4.26). In both cases the predicted critical current densities for drift are zero within the measurement accuracy ($\pm\,0.02\,\mathrm{MA/cm}^2$).

3. In the case of the passivated segment, there was no obvious difference between drift in the forward and reverse directions.

4. There was no obvious difference in drift velocity between unpassivated and passivated segments.

Al(Cu)

In contrast to pure Al, Al(Cu) exhibited an increasing drift velocity with time. The depletion versus time in unpassivated, 50 μm long Al(Cu) segments is shown in Figure 4.27. Electromigration testing was performed at 200°C and $2\,\mathrm{MA/cm}^2$ for approximately 100 hours in air. Edge displacements were determined using the EDX mapping technique. The drift velocity increased after roughly 40 hrs of testing from 5 nm/hr to 54 nm/hr.

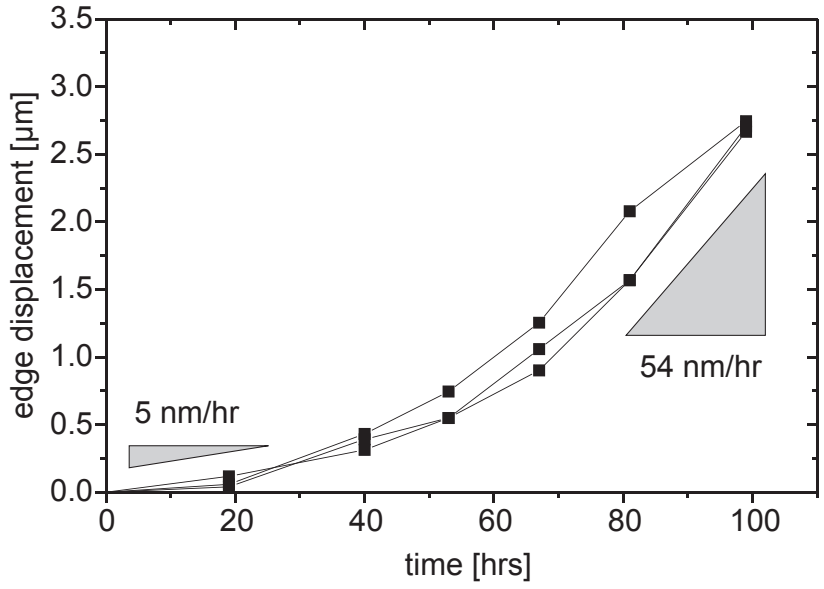

Figure 4.27: Edge displacement measured by EDX mapping in 3 unpassivated, 0.5 μm wide 50 μm long Al(0.5 wt% Cu) segments during testing at 200°C and $2\,\mathrm{MA/cm}^2$.

4.4.2.2 Short segments: Saturation and back-flux

In this section, drift in passivated Al and Al(Cu) segments is examined to show the effect of the back-flux and the effect of the Cu. Depletion in passivated segments saturates after relatively small amounts of Al displacement as long as the passivation is not damaged. Electromigration testing was performed at 250°C. The current density was 0.8 MA/cm^2 for the pure Al segments, and 1.5, 2.0, or 3.0 MA/cm^2 (Al(Cu)) for the Al(Cu) segments. The experiments were performed *in-situ* in an SEM using backscattered electron imaging in all experiments. In the case of pure Al, the resistance was monitored continuously. The Al(Cu) experiments were performed using the probe testing station without resistance monitoring.

The evolution of voids in two passivated, 100 μm long segments is shown in Figure 4.28 together with a schematic of the experiment. In the pure Al segment, no depletion was observed during the first 10 hours. Then both the resistance measurement and SEM observation showed void formation and saturation. In the case of the Al(Cu) segment, the resistance was not recorded and no SEM observation was performed during the first 18 hours. At 18 hours a void had already formed, which grew further and eventually saturated. When the current was turned off at 28 hours (pure Al) and 69 hours (Al(Cu)), a back-flux was observed, and the voids closed up somewhat.

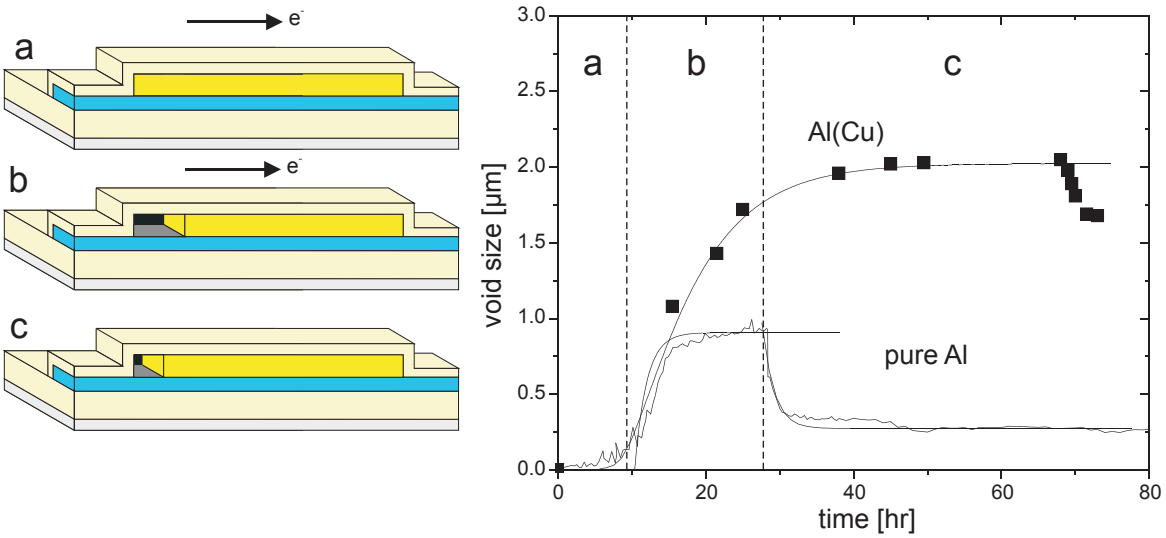

Figure 4.28: Void growth and shrinkage in passivated, 100 μm long segments. The behavior is shown schematically on the left, and void sizes on the right. Testing was performed at 250°C and 0.8 MA/cm^2 for the pure Al segment and 2.0 MA/cm^2 for the Al(Cu) segment.

Void sizes at saturation in all measured segments of various lengths are shown in Figure 4.29. The void sizes increase with segment length. The experiments performed at 3 MA/cm^2 do not show data points for the 100 μm long segments because the passivation cracked.

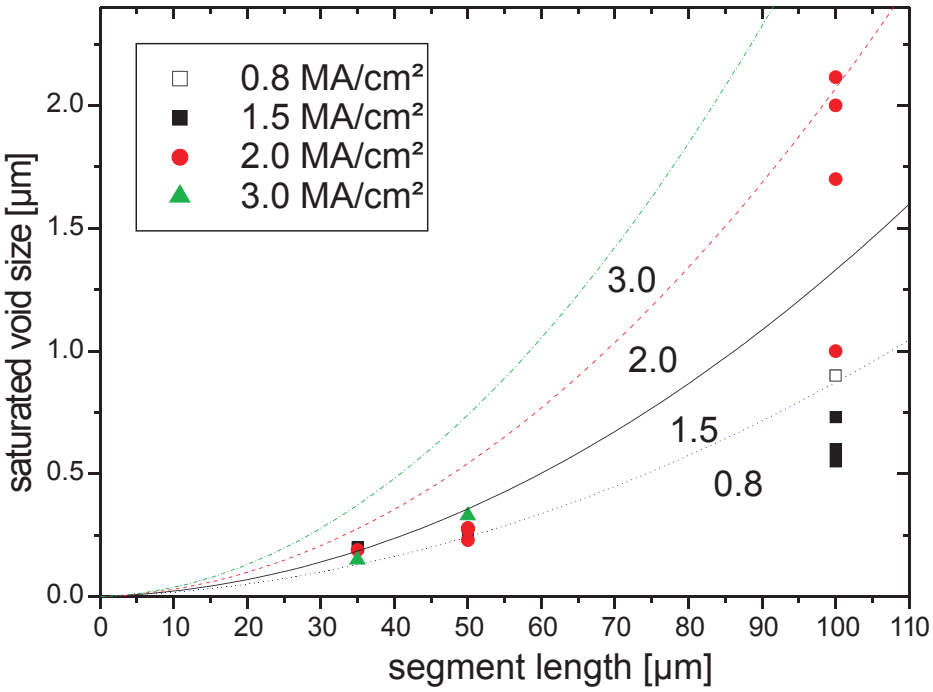

Figure 4.29: Void sizes at saturation as a function of segment length in passivated segments. Testing was performed at 250°C and the current densities listed in the diagram. The open square refers to pure Al, and the filled symbols refer to the Al(Cu) segments. The curves refer to modeled void sizes to be discussed in section 5.3.2.3.

4.5 Damage morphology

The damage morphology of the different sample types was examined by SEM and side-view TEM imaging. The section is organized by the damage and sample types.

4.5.1 Depletion

4.5.1.1 Pure Al

In unpassivated segments depletion or void formation occurred either directly at the cathode end, or within a few microns of the cathode end as illustrated in Figure 4.30. In cases when the voids did not form directly at the cathode end, they formed always at the interconnect sidewall. The void shapes were rounded and not faceted.

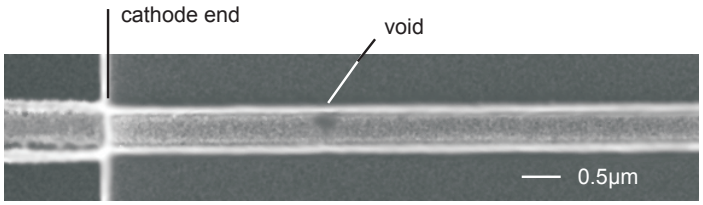

Figure 4.30: SEM image of a void near the cathode end of an unpassivated, 0.5 μm wide, 100 μm long Al segment after testing at 250°C and 0.5 MA/cm^2.

The distribution of void and hillock positions were measured in the unpassivated segments that were used for the threshold distribution measurements (section 4.2.1) to show the correlation between spatial damage and threshold distribution. The distribution of the void distances from the cathode end is shown in Figure 4.31 where it is seen that voids are most likely to form directly at the cathode end. There is some indication that voids are found further from the cathode end in longer segments.

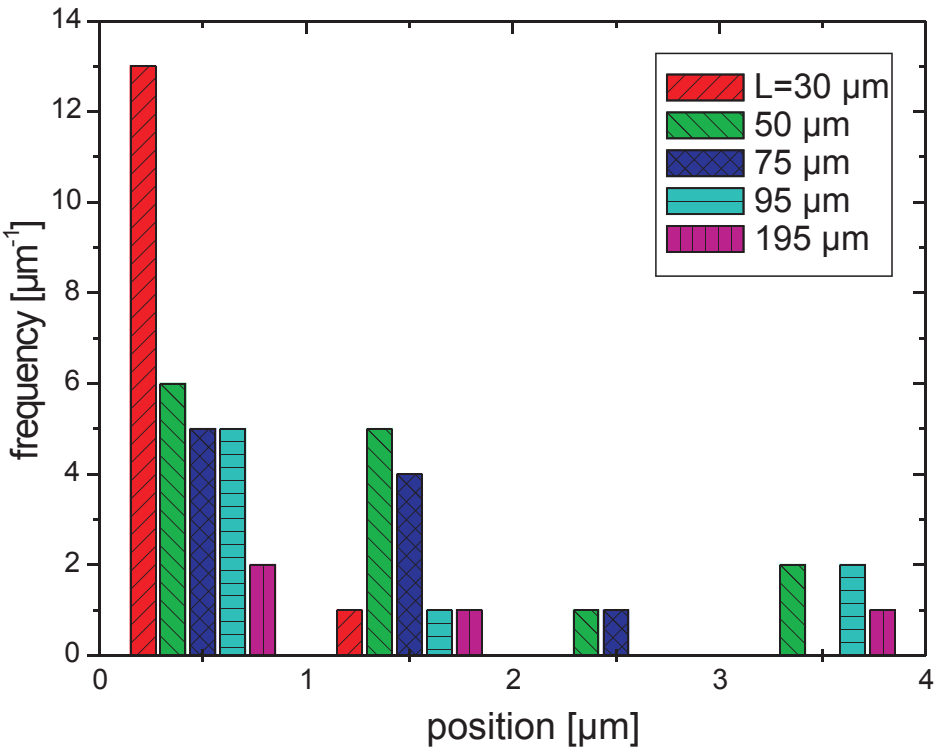

Figure 4.31: Distribution of void distances from the cathode end in unpassivated, pure Al segments after testing at 250°C and current densities between 0.2 and 1.6 MA/cm^2 (section 4.2.1). A total of 50 voids was measured. The histogram shows the number of voids in the first, second, third, and 4$^{\text{th}}$ micron of Al from the cathode end.

In passivated pure Al segments, the void shapes were similar to those in the unpassivated segments. In 200 μm long segments tested at 250°C and 1.0 MA/cm^2 voids were found directly at the cathode end in two cases, and 1.4 and 2.9 μm away from the cathode end in two other cases. In 100 μm long segments tested simultaneously, voids were observed directly at the cathode in four cases and in 1.6 and 1.7 μm distance in two other cases.

4.5.1.2 Al(Cu)

The void morphology in unpassivated Al(Cu) segments was similar to that in pure Al segments. Most voids formed directly at the cathode end, but some formed several microns away. Exact void positions in the Al(Cu) segments were not recorded.

The morphology of voids in passivated Al(Cu) segments was examined by side-view TEM. Figure 4.32 shows the first few microns of a 100 μm long 0.3 μm wide segment before (A) and after (B) electromigration testing. The sample preparation procedure is described in detail in section 3.2.2. Testing was performed *in-situ* in an SEM, and interrupted to perform TEM inspection. In Figure 4.32(A), contaminant particles on

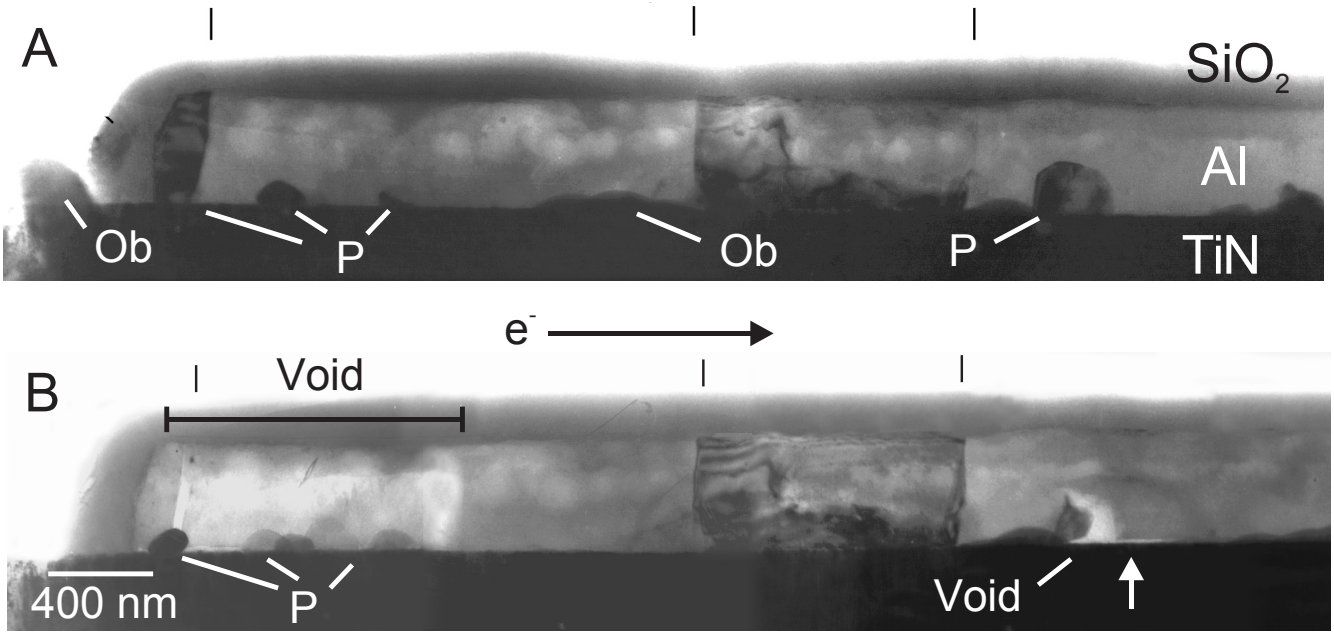

Figure 4.32: Side-view TEM images of a passivated, 100 μm long Al(0.5 wt%Cu) segment before (A) and after (B) electromigration. The positions of grain boundaries are indicated by short lines above the interconnect. Obstacles in the beam path, which were not part of the interconnect are labeled by Ob. Precipitates are labeled by P. Electron energy was 1 MeV. Testing was performed at 250°C and 0.8 MA/cm^2 for 48 hours.

the sample surface next to the Al segment (indicated by Ob), partly obscured the image of the Al. That the particles were not part of the segment was confirmed by adjusting the focus and tilting the sample. Prior to acquiring the image in 4.32(B), the sample was thoroughly cleaned by ethanol rinsing, such that most of the particles were removed. A number of particles were observed at the Al/TiN interface, which were likely Ti- or Cu-based precipitates. The exact compositions were not determined. The precipitates were better visible after electromigration in the depleted region than prior to electromigration testing. This is probably due to the poorer contrast in 4.32(A) since the precipitates are embedded in Al. Two voids were formed during the experiment as labeled in Figure 4.32(B). No other voids were observed in the entire segment. The Al was depleted uniformly in the first void (directly at the cathode end), although some residual material was left behind. The second void formed in and next to a precipitate. The depletion at this void extended under the adjacent Al-grain at the Al/TiN interface, as indicated by an arrow in the micrograph. From the TEM micrograph, the height of this narrow void region can be estimated to be smaller than 20 nm or roughly 90 atom layers.

Figure 4.33 shows the cathode end of a 50 μm long segment from the same test structure as in Figure 4.32, before (A) and after (B) electromigration testing. The micrographs shows the first grain and part of the second grain from the cathode end. The grain boundary is marked by a dashed line. Voiding occurred at the grain

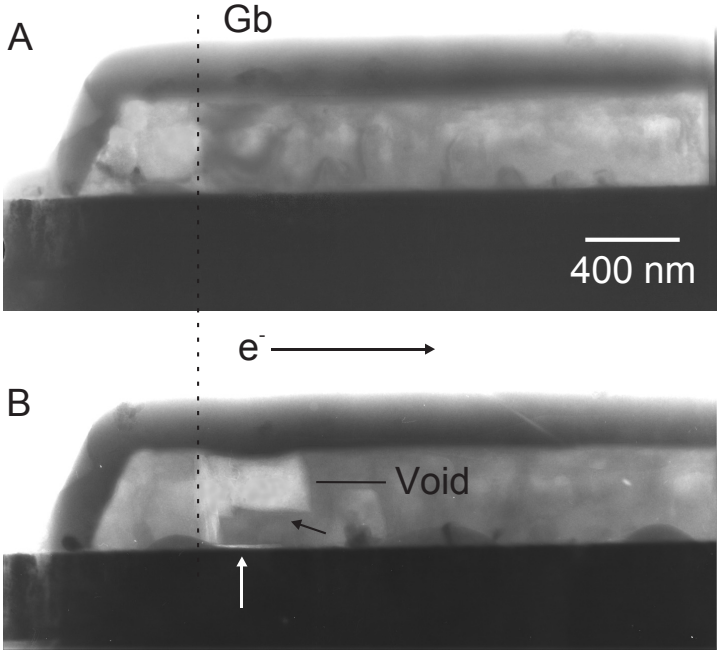

Figure 4.33: Side-view TEM images of the cathode end of a passivated, 50 μm long Al(Cu) segment, before (A) and after (B) electromigration testing for 48 hours at 250°C and 0.8 MA/cm^2. A void formed at the grain boundary, which is indicated by the dashed line.

boundary in the second grain by depletion from the top, as well as by the formation of narrow depletion along the Al/TiN interface (bright arrow). The void surface of the second grain showed facets with 90° corners (dark arrow). These corners could be seen clearly only if the sample was exactly aligned perpendicular to the electron beam in the TEM.

4.5.2 Accumulation

4.5.2.1 Pure Al

Hillocks in unpassivated, pure Al segments were only found directly at the anode ends. A typical example of a hillock in a 50 μm long, pure Al segment is shown in Figure 4.34. Both the capping layers (TiN and SiO_2) and the sidewall material have been

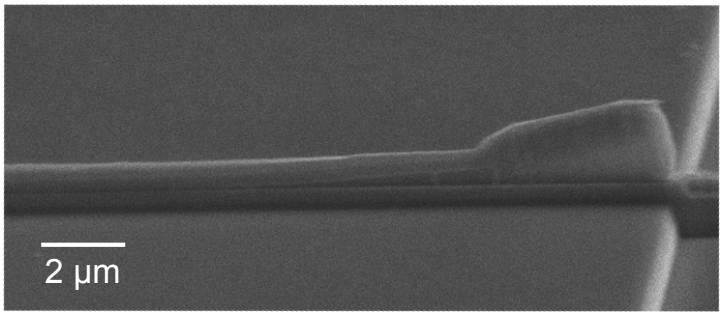

Figure 4.34: SEM image of a hillock at the anode end of an unpassivated, 50 μm long pure Al segment after testing for 29 hours at 1.6 MA/cm^2 and 250°C.

lifted up by the formation of a triangular-shaped hillock. In 24 out of 46 hillocks observed, the morphology was similar to that shown in Figure 4.34. They had grown by vertical extrusion of material and lifting up of the capping layers. The other 22 hillocks showed a more complicated and rounded shape. In all unpassivated, pure Al segments only single hillocks were observed.

Hillocks in passivated, pure Al segments were also found only at the anode ends. The morphology was similar to unpassivated Al. Two out of the five hillocks observed in segments tested at 250°C and 1 MA/cm^2 grew perpendicular to the substrate, whereas the others showed a more complicated morphology. Only a single hillock was found in each segment.

4.5.2.2 Al(Cu)

In contrast to the pure Al samples, hillock formation in the Al(Cu) segments sometimes occurred several microns away from the anode end. Figure 4.35 shows a hillock in an unpassivated Al(Cu) segment, which formed roughly 12 μm from the anode end. The segment was thinned by ion milling in the FIB. The grains in the hillock show a columnar structure. The small particles at the Al/TiN interface are presumably $TiAl_3$ precipitates. In another unpassivated, 50 μm Al(Cu) segment tested at 200°C and 2 MA/cm^2, two hillocks were observed, one directly at the anode end, and the other 12 μm away from the end. In two other 50 μm long Al(Cu) segments tested at the same conditions, hillocks were observed 9, and 14 μm away from the anode ends.

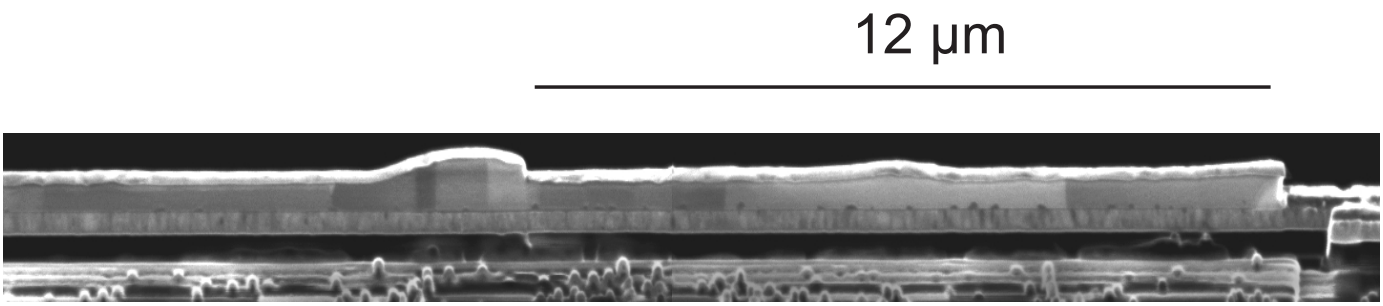

Figure 4.35: FIB micrograph of the anode end of an unpassivated, 35 μm long Al(Cu) segment after testing at 200°C and 2 MA/cm^2 for 48 hrs. Electron flow was from left to right. To reveal the microstructure, the width of the Al was thinned from one side by ion milling in the FIB.

In the case of passivated Al(Cu), hillock formation was also observed away from the anode end. In four 100 μm long segments tested at 2 MA/cm^2 and 250°C, the passivation cracked and single hillocks formed at 8, 10, 15, and 25 μm from the anode end of each segment. In another experiment, passivated Al(Cu) segments with lengths of 50 and 100 μm were tested at 250°C and a very high current density of 5 MA/cm^2. In this case, hillocks formed directly at the anode ends. The number of observations is not sufficient to investigate whether there is a significant correlation between the exact hillock position and the current density. A typical example of a hillock in a passivated, 50 μm long Al(Cu) segment is shown in Figure 4.36. The hillock grew perpendicularly to the substrate, lifting up the cracked part of the passivation. In order to reveal the microstructure, the hillock was examined by side-view TEM (Figure 4.37). The hillock had a columnar grain structure, with the exception of the last grain in the upper right corner in the micrograph. This suggests that the hillock grew by epitaxial addition of Al atoms to the original grains.

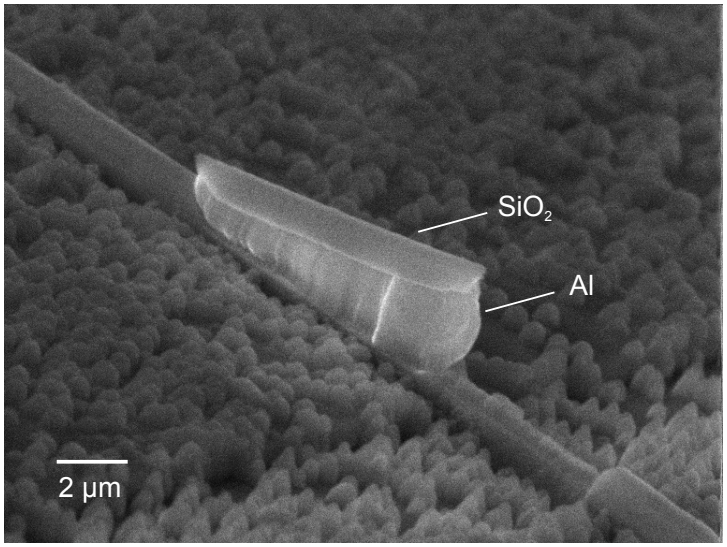

Figure 4.36: SEM micrograph of cracked passivation and hillock in a 50 μm long Al(Cu) segment after testing at 5 MA/cm^2 and 250°C for 22 hours. Tilt angle was 50°.

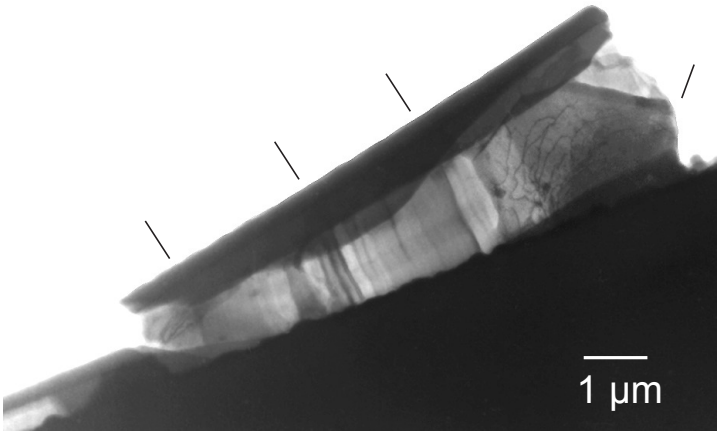

Figure 4.37: Side view TEM image of the hillock in Figure 4.36. Grain boundaries are marked by short lines.

More rounded hillocks were occasionally observed during electromigration testing. Figure 4.38 shows a sequence of SEM images of the anode end of a segment during electromigration testing at 5 MA/cm^2. The micrographs shows that cracking of the passivation occurred after testing for 7 hours. The crack extended along the length of the segment over several microns. After the passivation cracked, a part at the anode end lifted up slightly to form a hillock and further cracked the passivation. At 12 hours, another extrusion formed in front of the downstream hillock, which grew rapidly within roughly 2 hours. The final image shows the complicated morphology after 21 hours of growth. The final morphology is also shown in Figure 4.39 from another viewpoint. Figure 4.40 shows a side-view TEM image of the hillock marked in Figure 4.39. This hillock contained two grains. The grain boundary is indicated in Figure 4.40. The grain boundary region was imaged at higher magnifications, as shown in Figure 4.41, revealing many dislocations. With the exception of the region near the grain boundary, no other dislocations were found in the hillock.

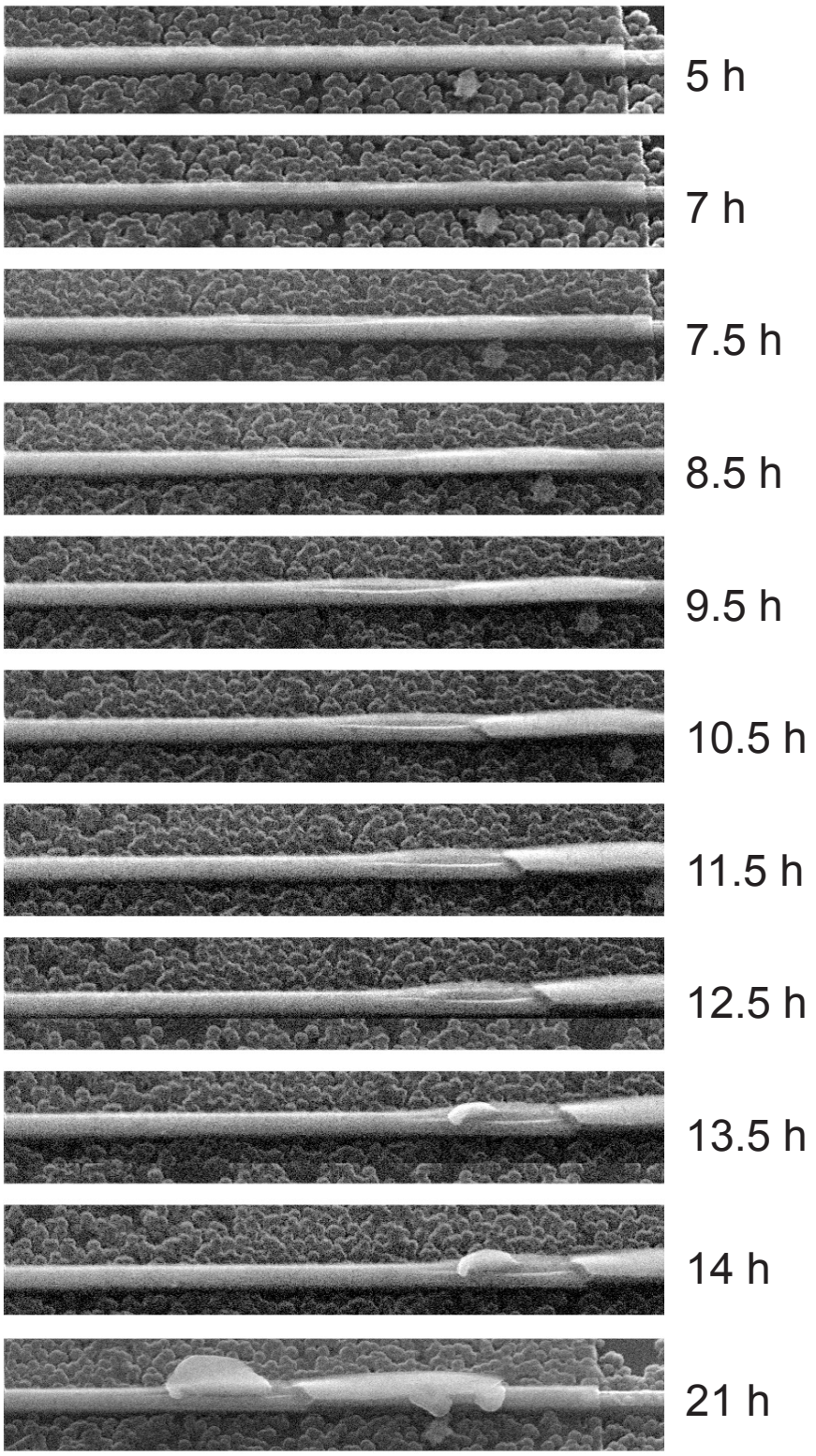

Figure 4.38: Passivation cracking and hillock growth in a passivated, 100 μm long Al(Cu) segment while testing at 250°C and 5 MA/cm^2. Due to sample drift, the images are shifted to the right.

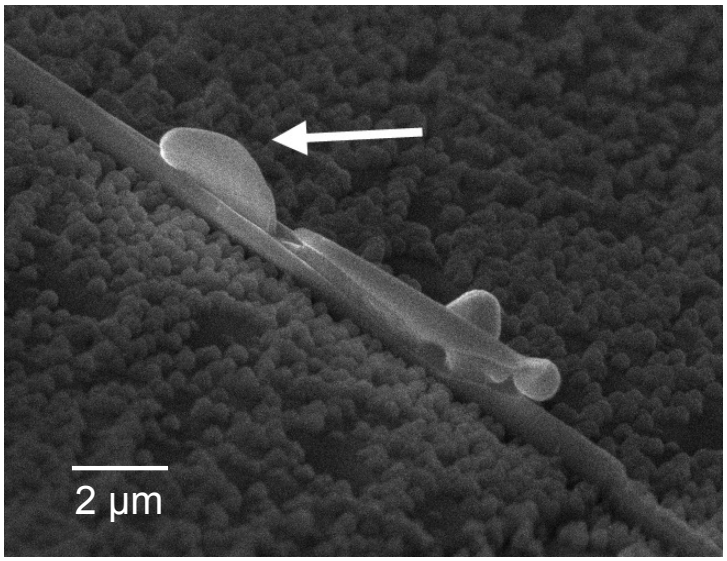

Figure 4.39: SEM micrograph of the final configuration of the anode end shown in Figure 4.38 after 21 hours of electromigration testing.

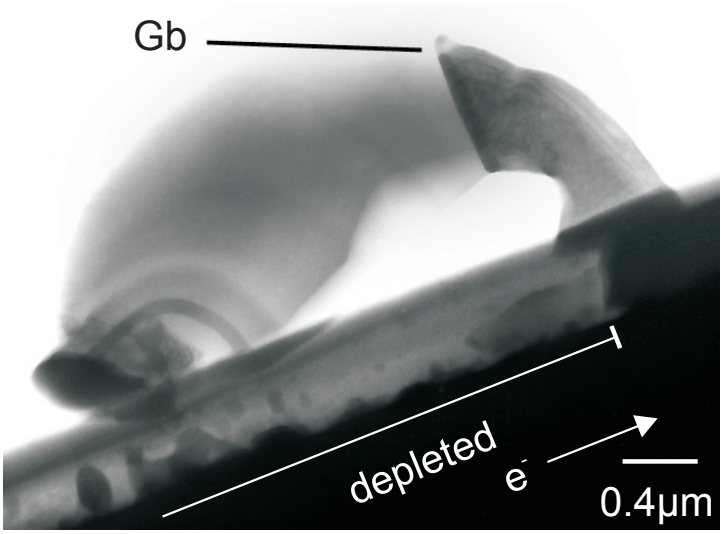

Figure 4.40: Side-view TEM image of the hillock marked in Figure 4.39. The segment was depleted up to the position of the hillock, as indicated in the image.

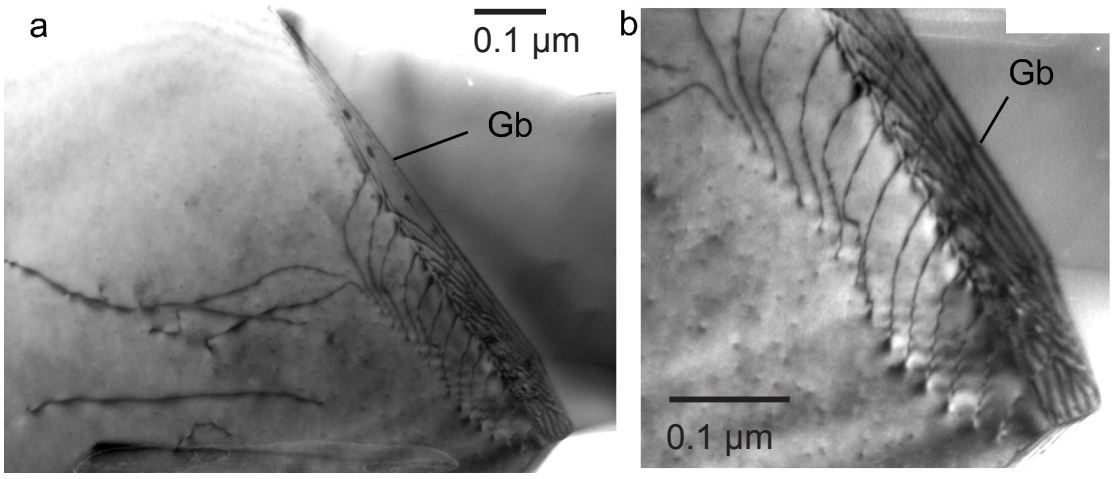

Figure 4.41: Grain boundary marked in Figure 4.40 at higher magnification. The grain boundary is slightly tilted so that the dislocation structure of the grain boundary can be seen. Other dislocations are visible, which extended from the boundary to the sample surface.

4.6 Summary of results

1. FIB and TEM characterization showed that the microstructure is close to perfect bamboo for passivated and unpassivated Al and Al(Cu) segments.

2. Threshold.

   - The threshold product was measured for a set of unpassivated, pure Al segments. The average value from segment lengths between 30 and 200 μm could be fitted using a single value of 4670 A/cm for $(jL)_c$. This is higher than literature values for wide, polycrystalline lines (1200 A/cm [Blech, 1976]), but comparable to values obtained for 0.4 μm wide bamboo lines (between 2400 and 5300 A/cm [Proost et al., 2000]).
   - The deviation of threshold values showed a systematic increase as the segment length decreased.
   - The threshold products for different sample types were found to obey the following order:
     - Unpassivated Al(Cu) > unpassivated Al.
     - Voiding passivated Al > unpassivated Al .
     - Voiding passivated Al(Cu) > voiding passivated Al .
     - Passivation crack Al(Cu) > passivation crack (Al).

3. Below threshold.

   - In the case of Al(Cu), Cu is preferentially transported to the anode end of segments, where Al_2Cu precipitates are eventually formed, but no damage such as voids or hillocks occurred. Growth of the precipitates reached eventually saturation.
   - Upon current reversal, these precipitates dissolved and new precipitates eventually formed at the opposite ends at a rate roughly proportional to current density (during the constant drift stage).
   - If the current was too low, or the segment too short no precipitate formed at the opposite end.
   - Turning the current off after saturation was reached, the precipitates dissolved to some extent.

4. Above threshold.

   - The incubation time to form a void in pure passivated Al was found to scale with j^{-2}.
   - Depletion in passivated and unpassivated pure Al took place at a constant drift velocity which scaled with j.
   - Drift velocities in passivated and unpassivated long pure Al segments were found to be the same.
   - In contrast to pure Al, the drift velocity in long Al(Cu) segments was found to increase as time proceeds.
   - Drift in short passivated segments saturated in both Al and Al(Cu).
   - Void sizes at *saturation* were found to increase with L.
   - Turning the current off after *saturation* of void growth was reached, a back-flux of Al was observed in both Al and Al(Cu).

5. Damage morphology.

   - Voids formed predominantly at the cathode ends or a few microns away from the cathode ends at the sidewalls of the segments in all segment types. In the case of unpassivated, pure Al segments, indication was found that voids form further away in longer segments.
   - At the bottom Al/TiN interface, in the case of passivated Al(Cu) segments, very narrow voids were observed by side-view TEM.
   - The voids inspected by side-view TEM formed either directly at the cathode ends, or at grain boundaries.
   - Hillocks in passivated and unpassivated pure Al segments were found only directly at the anode ends. In Al(Cu) segments, hillocks were also formed several microns away from the anode.
   - At very high current densities, the passivation cracked at or near the anode ends. For one case it has been shown that the crack extended over several microns along the length of the segment.

5

Discussion

In this chapter the analysis of the experimental results is presented. It is divided into a discussion of the electromigration threshold for damage formation, electromigration below the threshold, and experiments above the threshold.

5.1 Electromigration threshold

5.1.1 Threshold as a function of sample type

The existence of an electromigration threshold, as suggested by equation 2.5, has been confirmed by numerous observations, for example [Grabe and Schreiber, 1983, Ross et al., 1989, Hemmert and Costa, 1991]. The threshold product was found to be constant as a function of segment length, current density, and time. This is in agreement with the threshold length concept (Blech-Herring model), and the idea that the maximum stress difference that a segment can sustain is a constant [Blech, 1976].

The average threshold product for unpassivated pure Al segments of 4670 A/cm is significantly higher than what has been reported for wide, polycrystalline lines ($\sim$1200 A/cm [Blech, 1976], but comparable to values reported for narrow lines (2400-5300 A/cm [Proost et al., 2000]). $\Delta\sigma_c$ is known to increase with the aspect ratio of the interconnect: an increase of the threshold product by a factor of 2.5 was reported for segments that had an aspect ratio of 0.33 vs. 1.0 [Hu et al., 1993b].

Significant differences in the threshold product and the damage morphology were found between the different sample types investigated. The order of the threshold products observed and the general nature of damage in the different sample types is

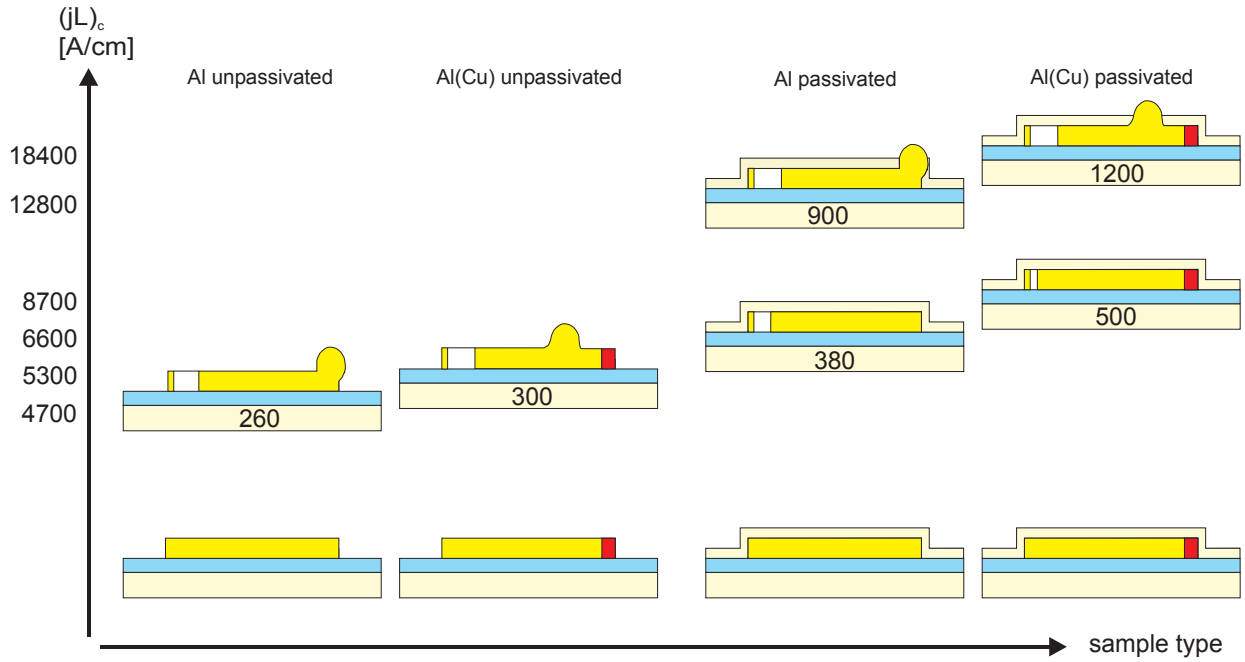

Figure 5.1: Threshold products and nature of damage for the different sample types at 250°C except unpassivated Al(Cu) (200°C). The threshold stress differences in the pictograms are given in MPa. They were calculated using eq. 2.5 and Z^*=-2.2. Precipitates in Al(Cu) are indicated at the anode ends of the segments. For comparison, segments without damage are shown in the lower part.

illustrated in Figure 5.1. The threshold for passivated segments is higher in comparison to unpassivated, and the Al(Cu) segments showed a higher value than the pure Al segments. Hillock positions were shifted away from the anode end in segments containing Cu (passivated and unpassivated), whereas voids were found at or near the cathode end in all sample types.

The threshold product for voiding in passivated, pure Al segments was between 1000-2000 A/cm higher than for unpassivated pure Al segments, which is in agreement with previous measurements [Blech, 1976, Ross et al., 1989]. This difference corresponds to a difference in $\Delta\sigma_c$ of roughly 60-120 MPa (using eq. 2.5 and Z^*=-2.2). In the case of passivated segments hillocks are suppressed, hence the measured threshold product is associated with the threshold stress for void formation. In these segments, the passivation has to crack before hillocks can form. In the case of unpassivated segments, it is possible that hillocks are more easily formed than voids. The critical stress difference $\Delta\sigma_c$ these unpassivated segments can sustain would then be associated with the stress that is required to form a hillock. The difference in threshold product would then reflect the different stresses required to create hillocks (unpassivated) and voids (passivated).

The threshold product in passivated Al(Cu) segments was observed to be 1000-2000 A/cm larger than in passivated pure Al segments. Commonly accepted is the idea that Cu reduces the Al mobility significantly [Hu et al., 1993a]. A critical Cu concentration c_c is defined, below which the Al diffusivity drops from a high value, which is believed to be close to the pure Al value, to a much lower value [Kim et al., 1997]. This is illustrated schematically in Figure 5.2. The position of the critical concentration is sometimes called the Cu-front. Due to the change in the Al diffusivity, the Cu-front position represents an Al flux divergence, leading to a maximum in stress. Hence, the effective Al(Cu) segment length is shorter than the physical length. Assuming a precipitate is present at the anode end of the segment, such that the Cu concentration in solution is held at the solubility concentration ($c(x = L) = c_S$), the Cu concentration profile at steady-state is given by (compare section 5.2.1)

$$c(x) = c_S \exp\left(-\frac{Z^*_{Cu} e \rho j}{kT}(x - L)\right) , \tag{5.1}$$

where x is the distance from the anode end, and c_S the solubility limit. The position of concentration c_c (equivalent to L_{eff}) is then given by

$$L_{\text{eff}} = L - \frac{kT}{ejZ^*_{Cu}\rho} \ln\left(\frac{c_s}{c_c}\right) . \tag{5.2}$$

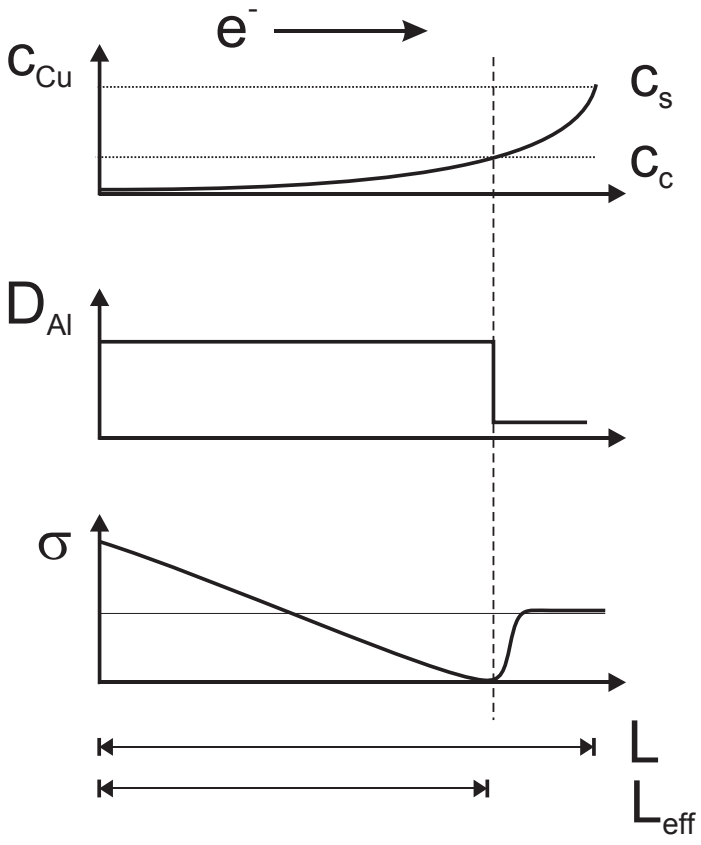

Figure 5.2: Schematic diagram of the Cu effect. The upper graph shows the Cu concentration at steady state. At the position of the critical Cu concentration c_c (Cu-front) a flux divergence occurs, such that the effective segment length L_{eff} is shorter than L.

The change in threshold product is then calculated to be

$$\Delta(jL)_c = |\frac{kT}{eZ^*_{Cu}\rho} \ln\left(\frac{c_s}{c_c}\right)| \,, \tag{5.3}$$

which is shown in Figure 5.3. It is concluded that a critical Cu concentration of roughly 0.04 at% explains the observed behavior. It is worth noting that the Cu-front effect has been verified in a recent experiment [Kao et al., 2000]: the local strain of an Al(Cu) segment was measured *in-situ* during electromigration by X-ray microdiffraction. Simultaneously, the Cu concentration was measured using X-ray fluorescence. The study showed that, when Cu is swept towards the anode end, the strain gradient persists only up to a position where the Cu exceeds a critical concentration of 0.15 at% at 310°C. The value obtained compares reasonably to early estimates of c_s (0.1 at% [Lloyd, 1997]), but is larger than what was used here to explain the results. The difference may simply be due to the fact that the present measurements were performed at 250°C rather than 310°C. The solubility at 250°C is only 0.1 at%, hence such high critical Cu concentration could not be reached.

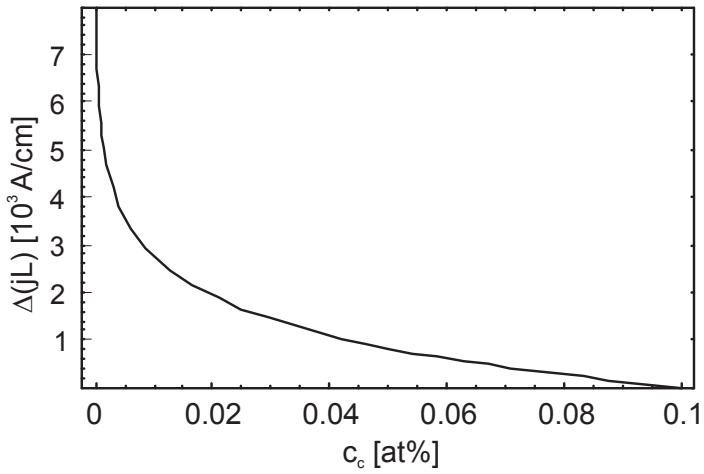

Figure 5.3: Change in threshold product as a function of critical Cu concentration c_c. A solubility of c_s = 0.1 at% at 250°C, and an effective valence for Cu in Al of Z^*_{Cu} = -14 were used.

The threshold product measured can be used to calculate the stress required for passivation cracking using equation 2.5. A critical stress of 900 MPa is obtained for passivated, pure Al, using $Z^* = -2.2$. A rough estimate for the critical stress for passivation cracking in the literature was 1 GPa [Hemmert and Costa, 1991], which is in reasonable agreement with the value obtained here. The threshold product for passivation cracking in Al(Cu) segments was higher than in pure Al segments. The factor by which the threshold increased is roughly the same as the one for the increase for void formation. The effect is also attributed to the influence of Cu. In contrast to

passivated pure Al, where the passivation cracked directly at the anode end, cracking and hillock formation was found at distances between 8 and 25 μm from the anode end in Al(Cu) segments tested at 250°C and 2 MA/cm^2. At the test conditions used, the calculated Cu-front position is 20 μm away from the anode end, using $c_c = 0.04$ at%, which is in reasonable agreement with the hillock positions observed. This observation supports the idea that the Cu leads to a flux divergence at a position away from the anode end.

The threshold product of unpassivated Al(Cu) was 600 A/cm higher than unpassivated pure Al. In contrast to pure Al, hillocks formed between 9 and 14 μm away from the anode end at 200°C and 2 MA/cm^2. These observations are in agreement with the idea of a Cu-front that leads to a reduced effective segment length, as described for the passivated case. At the test conditions used, the calculated Cu-front position is 8 μm away from the anode end, which is in reasonable agreement with the hillock positions observed. The measurements on the unpassivated Al(Cu) samples were performed at 200°C in comparison to 250°C in the pure Al case. The temperature dependence of the threshold product in pure Al is known to be small [Straub, 2000]. However, it is expected that the Cu distribution is temperature dependent, because the Cu solubility is decreased at the lower temperature. Assuming that the temperature of the critical concentration c_c is small, it is expected that the Cu effect in this case is smaller than at the higher temperature, consistent with the observations.

5.1.2 Threshold distribution

For the first time, the statistical distribution of threshold products was investigated in unpassivated, pure Al segments. In agreement with the literature data [Grabe and Schreiber, 1983, Ross et al., 1989], the mean threshold product measured in this work is roughly constant for the different segment lengths. A significant increase in the deviation in the measured threshold product distributions has been observed. A conceptually simple model was established to explain this behavior. It is assumed that the threshold stress is not a fixed value (Blech-Herring model), but shows a distribution along the length of the segment.

For the sake of simplicity, discrete points are considered, possessing various threshold stresses as illustrated in Figure 5.4. The threshold stresses are assumed to be normal distributed with the mean $\bar{\sigma}_c$, and the standard deviation δ. A lower limit in

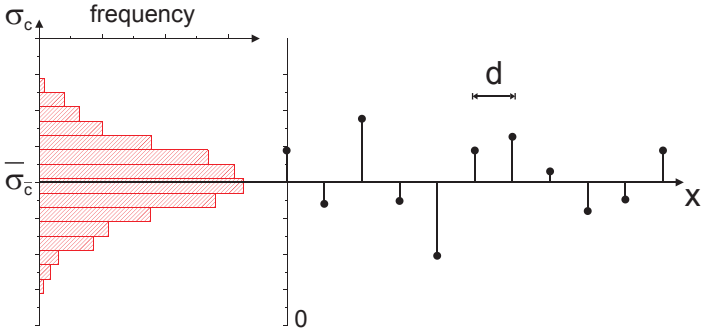

Figure 5.4: Schematic diagram of discrete points of different threshold stresses along the length of the segment, with spacing d. The histogram on the left side of the diagram represents the density function of the threshold stress distribution.

possible threshold stresses σ_L is defined by $\sigma_L = \bar{\sigma}_c - 2\delta$, such that $\bar{\sigma}_c \pm 2\delta$ represents the range in σ_c values that covers 95% of the existing threshold stresses. The intersection of the electromigration-induced stress gradient $\sigma(x)$ and σ_L gives the length ΔL, in which most damage occurs. This length will be called the possible damage zone (*pdz*). As the electromigration-induced stress gradient becomes more shallow in longer segments, ΔL increases. Figure 5.5 shows schematically the electromigration-induced threshold stress gradients for two different segment lengths. For the shorter *pdz* in shorter segments, a smaller number of possible damage sites are subjected to a stress above the threshold. In other words, in long segments, more sites can possibly form

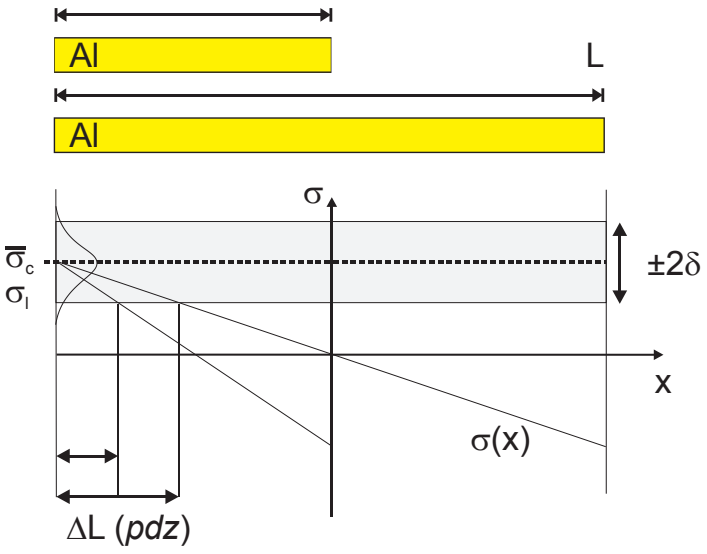

Figure 5.5: As the threshold electromigration-induced stress gradient becomes more shallow with segment length, the possible damage zone becomes larger. 95% of the existing threshold stresses are within the $\pm 2\delta$-window around $\bar{\sigma}_C$.

damage, so that damage is more likely. As the deviation in any statistic is a function of the sample size, the deviation in measured threshold products is smaller for longer segments. Next, it is assumed that the damage sites have a constant spacing d. The number of possible damage sites within the *pdz* N is then given by

$$N = \frac{\Delta L}{d} \,, \tag{5.4}$$

For the electromigration-induced stress distribution the linear steady state profile is used, which is according to eq. 2.5 given by

$$\sigma(x) = GL(1/2 - x/L) \,, \tag{5.5}$$

where $G = 2\bar{\sigma}_c/L$ is the mean threshold stress gradient. The length of the *pdz* can be calculated by the intersection of $\sigma(x)$ and σ_L to be

$$\Delta L = \frac{L(\bar{\sigma}_c - \sigma_L)}{2\bar{\sigma}_c} \,. \tag{5.6}$$

From statistics it is known that for samples of a population of finite variance, the variance of the sample decreases with the sample size as $1/N$, and the change in the standard deviation of the sample as

$$\Delta\delta = \frac{1}{\sqrt{N}} \,. \tag{5.7}$$

The change in standard deviation in threshold stress is then calculated using eqs. 5.6, 5.7, and 5.4 to be

$$\Delta\delta = 1/\sqrt{\frac{(1 - \sigma_L/\bar{\sigma}_c)}{2d} L} \,. \tag{5.8}$$

Equation 5.8 was used to fit the observed deviations as a function of segment length. The result is shown in Figure 5.6. The fit results in a value for the pre-factor before L under the root:

$$\frac{(1 - \sigma_L/\bar{\sigma}_c)}{2d} = (0.9 \pm 0.1)\,\mu m^{-1} \,. \tag{5.9}$$

This factor contains the ratio $\sigma_L/\bar{\sigma}_c$, and the failure site spacing d as unknowns. The ratio $\sigma_L/\bar{\sigma}_c$ may vary between 0 and 1. The failure site spacing d is therefore between 0 and $1.8\,\mu$m. The average grain size of roughly $1\,\mu$m for the small grains compares reasonably with the range of failure site spacings. It is possible that the grain boundaries are the preferred damage sites (compare Figure 4.33).

Beside the deviation, it is also expected that the mean threshold product depends on the segment length, because from a given set of possible damage sites, the one with the smallest threshold stress value fails. As the number of possible damage

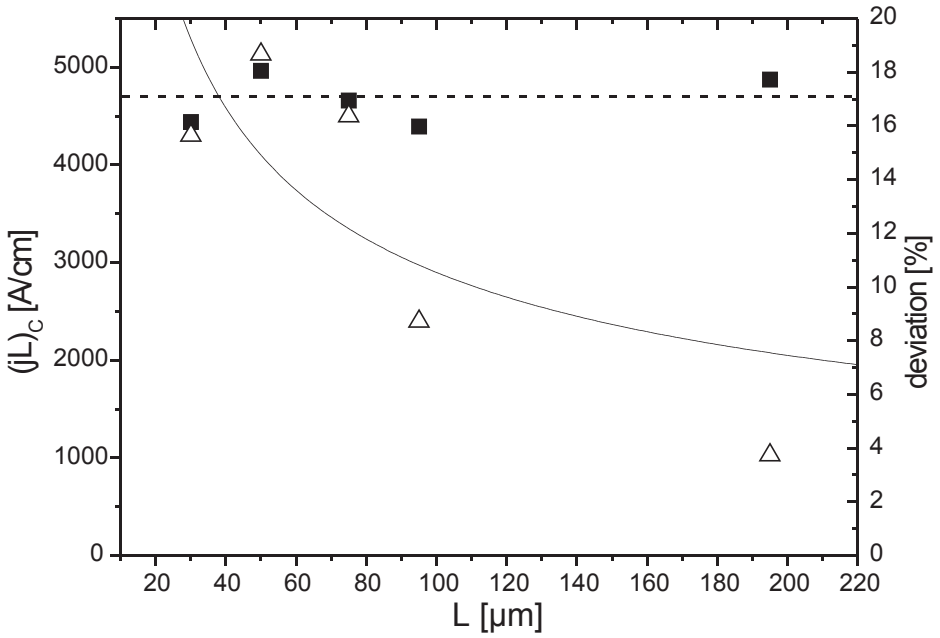

Figure 5.6: Mean (squares), and deviation (triangles) of measured threshold products as a function of segment length. The solid curve is a best fit using equation 5.8.

sites increases with segment length, the mean threshold is expected to decrease. The expected mean threshold stresses as a function of segment length were calculated by Monte-Carlo simulation (see appendix B.1). To simulate a single interconnect segment, normally distributed threshold stresses values were chosen randomly, using a constant spacing d. The threshold stress gradients G between each of these points and the center of the segment (zero stress) were calculated. Then, the minimum value of these gradients was recorded. This procedure was repeated for 1000 segments per segment length, and the average minimum values calculated. The result is shown in Figure 5.7. In the segment length range investigated, it is expected that the mean threshold stress decreases by roughly 5%, which is less than the scatter in the measured mean threshold products.

In real interconnects the failure site spacing is presumably itself statistically distributed. This case is treated in appendix B.1. The expected threshold deviation change as a function of segment length is not significantly different from the constant failure site spacing case. Since the experimental sample size was not large enough to reveal the exact nature of the statistical distributions, the use of a constant failure site spacing is a reasonable approximation.

The stress profiles were assumed so far to follow equation 5.5, implying that the electromigration-induced stress gradient goes through zero in the middle of the segment. Gleixner and Nix pointed out that the linear stress profiles might shift towards

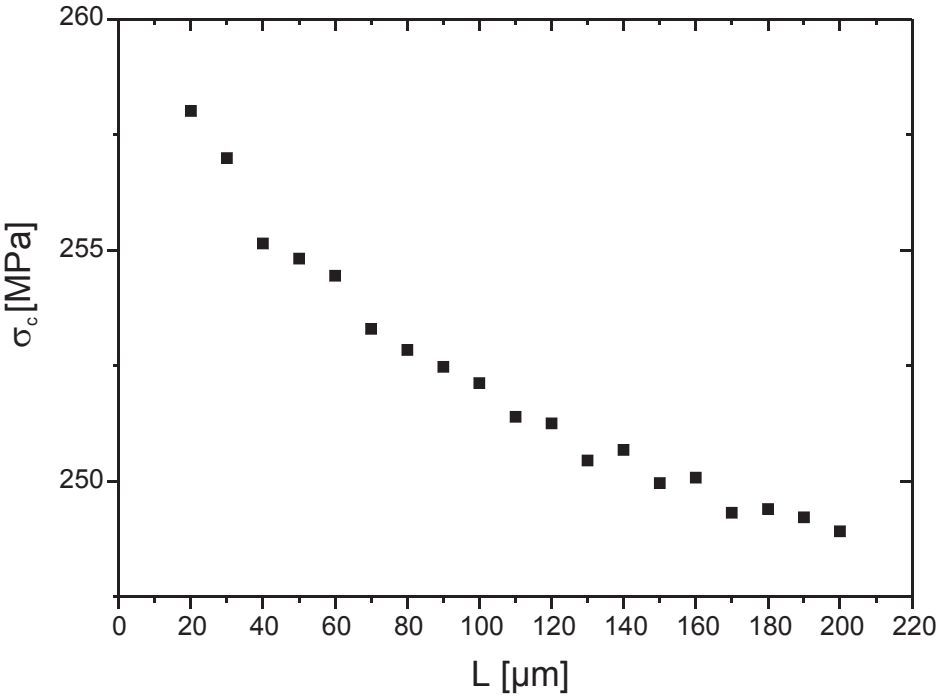

Figure 5.7: Expected mean threshold stresses. A mean σ_c of 260 MPa, a deviation of δ=20 MPa, and a spacing of d=0.5 μm were used.

more tensile or compressive values, due to an asymmetric distribution of grain boundaries, which act as sources and sinks for displaced atoms [Gleixner and Nix, 1998]. The authors showed that the deviation in the maximum electromigration-induced stress (at the segment ends) increases with decreasing segment length. Their calculation was adapted to the dimensions of the present segments, as described in appendix B.2. It can be shown that the deviation in the maximum stress, in the length range of interest between 30 and 200 μm, varies by less than 1%, which is small compared to the variation observed experimentally.

The model of a variation in threshold stresses has been described above for the cathode end of segments. Due to the symmetry of the problem, this idea can be applied to the compressive end as well. However, hillocks were observed only directly at the anode ends of the segments. In contrast, it was observed that voids form further away from the cathode ends in longer segments (see section 4.5.1.1). Hence, the concept of the possible damage zone is used in the following to explain the distribution of void positions as a function of segment length.

The number of voids observed per unit line length is a measure of the damage probability as a function of position x from the cathode end. To calculate the damage probability, the distribution density function of σ_c is integrated over all stress values *below* the electromigration-induced stress at position x:

$$P(x) \sim \frac{1}{L} \int_0^{\sigma(x)} f(\sigma_c')\, d\sigma_c' \,. \tag{5.10}$$

The factor $1/L$ results from the condition that the total probability (integral over all x) is independent of L. The normal distribution density function f for the threshold stresses is given by

$$f(\sigma_c) = \frac{1}{\sqrt{2\,\pi}\,\delta} \exp\left(-\frac{(\sigma_c - \bar{\sigma}_c)^2}{2\,\delta^2}\right) \,. \tag{5.11}$$

The stress profile $\sigma(x)$ along the segment was given by equation 5.5. The lower integration boundary in eq. 5.10 can be approximated by $-\infty$. It follows that

$$P(x) = \frac{nA}{L}\left(1 - \mathrm{erf}\left(\frac{\sqrt{2}\,x\,\bar{\sigma}_c}{L\,\delta}\right)\right) \,. \tag{5.12}$$

where A is a normalization factor, and n the number of segments tested. Equation 5.12 was used to fit the measured number of voids per μm from the cathode end (Figure 4.31), as shown in Figure 5.8. From this fit, a value for $\bar{\sigma}_c/\delta$ is obtained to be $\bar{\sigma}_c/\delta \approx 10..20$. Using 260 MPa as the mean threshold stress (equation 2.5), a deviation δ between roughly 10 and 26 MPa is obtained. The large error stems from the small number of observations.

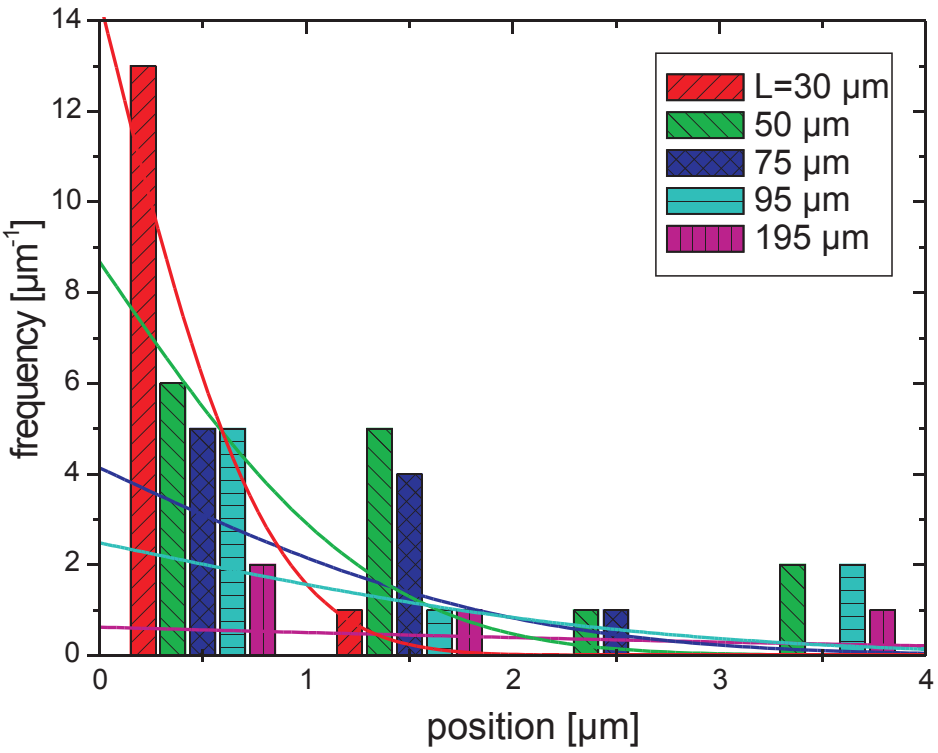

Figure 5.8: Distribution of void positions as a function of position away from cathode end. The curves result from fitting eq. 5.12 to the data. The parameters used were $\bar{\sigma}_c/\delta = 12$, and $A = 31$.

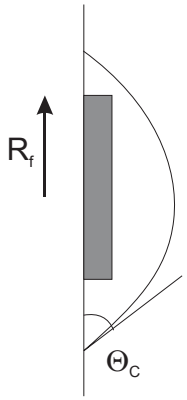

Figure 5.9: Schematic diagram of interface flaw with adjacent void.

As the physical reason for the observed variation in threshold stresses, a size distribution of void nuclei is suggested. Several authors found that nucleation of voids in Al lines under electromigration conditions is a difficult process, such that some kind of flaw or void nucleus must be present to explain the experimentally observed nucleation rates [Arzt and Nix, 1992, Gleixner et al., 1997]. Such flaws could be established by contaminant patches at the sidewall interface [Clemens et al., 1997], which is illustrated in Figure 5.9. The latter study showed that the nucleation barrier depends on the size of the flaw. For a circular interface flaw the threshold stress to nucleate a void is given by

$$\sigma_c = \frac{2\gamma_{Al} \sin \Theta_c}{R_f} \ , \tag{5.13}$$

where γ_{Al} is the Al surface energy, Θ_c the wetting angle and R_f the flaw radius. The threshold stress as a function of R_f is shown in Figure 5.10. The range of observed threshold stresses leads to a range of flaw sizes as indicated in Figure 5.10. It is concluded that flaws of sizes between 2 and 12 nm (R_f) explain the observed variation of threshold stresses.

The implications of the length dependent deviation of threshold products on reliability are illustrated in a damage map (Figure 5.11). Similar damage maps without the statistical deviation in threshold products were suggested earlier [Kraft and Arzt, 1998, Andleigh et al., 1999]. A constant threshold product divides the map into the regions "mortal" and "immortal". As the deviation increases with decreasing segment length, the immortal region becomes increasingly smaller for higher current densities. For comparison, the jL-curves for the mean threshold, the $\pm\delta$, and for the $\pm 2\delta$ ranges are shown in the map. From the normal distribution, one would expect 0.0032% of the interconnect segments to have a threshold stress 4δ lower than

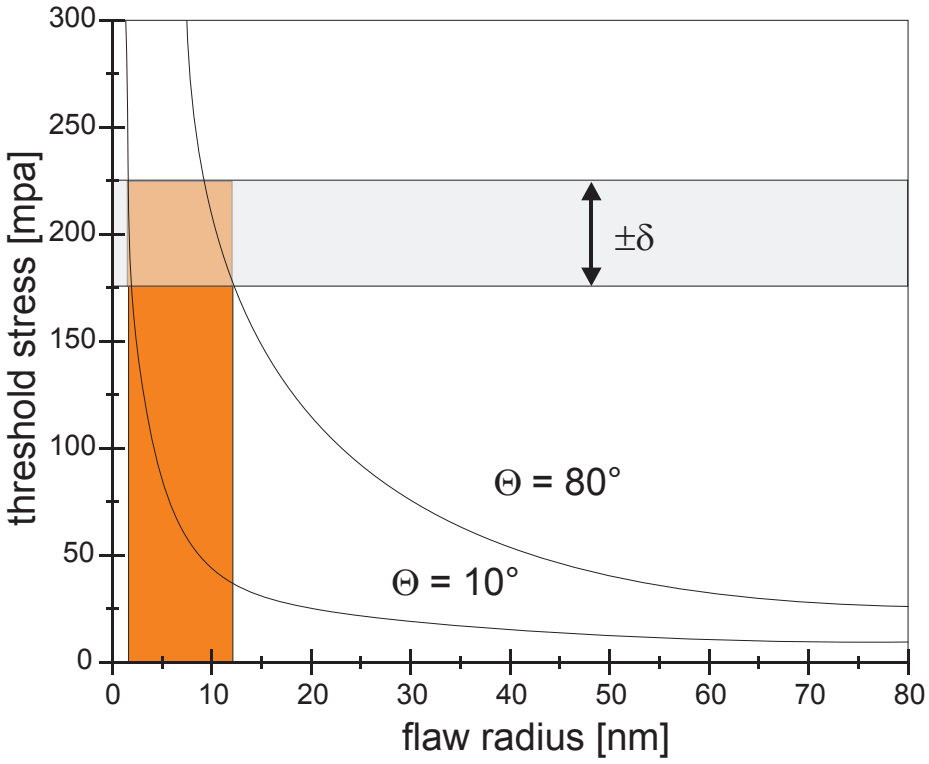

Figure 5.10: Threshold stress for void nucleation as a function of flawsize. The range of observed threshold stresses is indicated by δ. The surface energy of Al was assumed to be $1\,\mathrm{J/m^2}$.

the mean. While this may seem an insignificant percentage, it amounts to over 30 lines in a chip containing one million interconnects. From the models for electromigration, it is expected that a deviation in threshold stress results in a deviation in incubation times for damage formation. Hence, measured lifetimes are expected to show a length dependent deviation if the incubation times are important for lifetimes. Without performing a rigorous analysis, a data set taken from the literature demonstrates the effect. Figure 5.12 shows the lifetime and deviation of sub-micron wide, bamboo segments made from Al(0.75% Si, 0.5% Cu) as a function of segment length [Oates, 1994]. The median time to failure (MTF) was roughly constant with respect to L, whereas the deviation increased significantly as the length approached roughly $100\,\mu$m. Although the threshold length was not listed explicitly in the reference, from typical values for passivated segments obtained in this work (threshold product between 5000 and 10000 A/cm), it can be estimated to be around $100\,\mu$m.

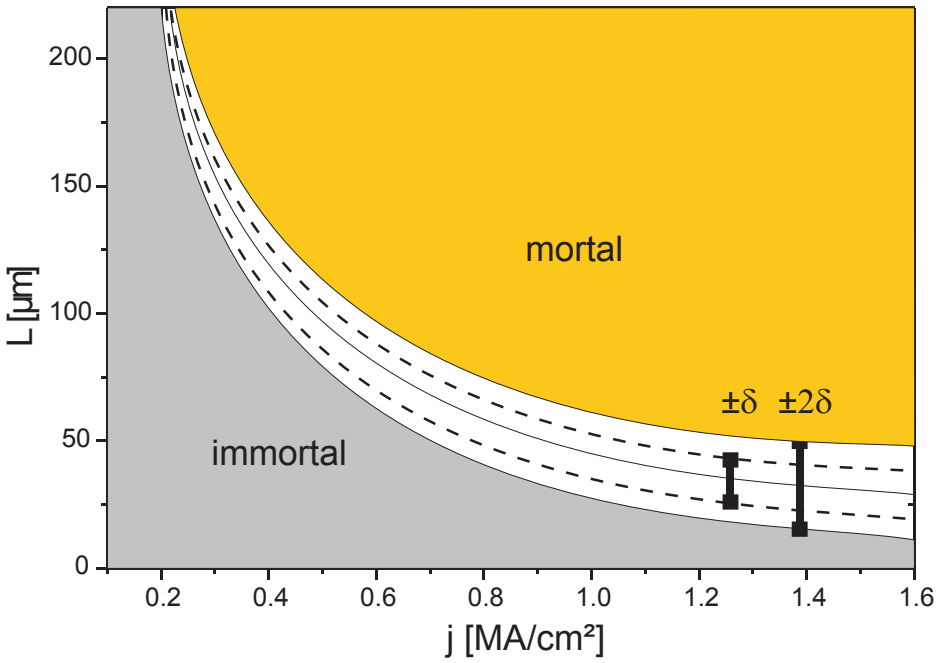

Figure 5.11: Damage map: The jL threshold divides the map into safe (immortal) segments, and segments in which damage is eventually formed. The jL=const. curves for the mean threshold, the $\pm\delta$, and for the $\pm 2\delta$ ranges demonstrate the increasing dispersion.

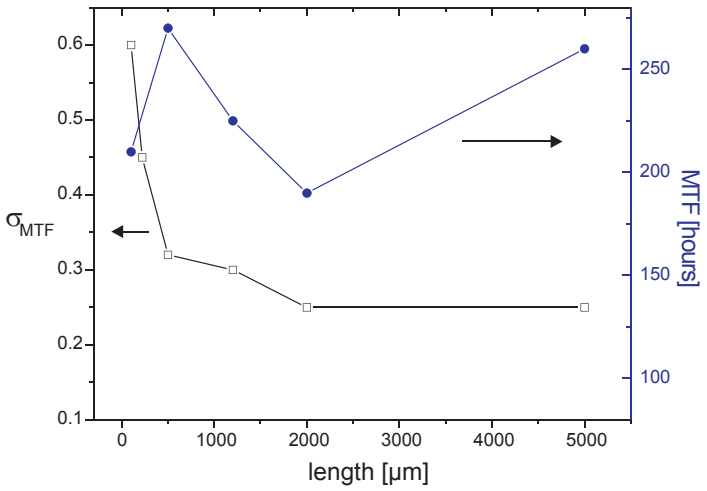

Figure 5.12: Median time to failure (MTF) and deviation in time to failure (σ_{MTF}) as a function of segment length [Oates, 1994]. The MTF is roughly constant with segment length, whereas the deviation increases significantly in shorter segments. The samples consisted of passivated, 0.6 μm wide segments on TiN barrier layers, tested at 250°C and 1.0 MA/cm^2.

5.1.3 Conclusions

- The threshold product for damage formation in Al(Cu) is increased in comparison to pure Al segments. Furthermore, it was observed that, in contrast to pure Al, hillocks formed at some distance from the anode end in Al(Cu) segments. Both observations are consistent with the model of a Cu-front that leads to an effective segment length shorter than the physical length.

- The passivation increases the threshold for void formation. This could be attributed to the suppression of hillock formation in the case of passivated segments.

- The investigation of the statistical distribution of threshold products in unpassivated, pure Al segments showed that the mean value is roughly constant as a function of segment length. The deviation was observed to increase with decreasing segment length. To explain this behavior, a model was introduced that assumes a threshold stress which depends on local microstructure and thus varies with position along the interconnect.

- Observations of the damage morphology showed that voids were located further away from the cathode end in longer segments, consistent with the idea of a distribution in threshold stresses.

5.2 Below threshold

The electromigration-induced flux generates atom motion, which generates a stress gradient in Al segments. This stress gradient generates a back-flux that counterbalances the electromigration-induced flux. As long as the stress difference is below the critical stress difference, no further Al motion or depletion takes place, which was confirmed by the EDX mapping technique. In the case of segments containing Cu, substantial redistribution of Cu takes place. For polycrystalline Al(Cu) the Cu transport is well known to occur along grain boundaries [Hu et al., 1993a, Spolenak et al., 1998b]. To investigate the impact of miniaturization on the electromigration-induced Cu transport, the Cu motion in sub-critical bamboo segments is analyzed in this section, based on the precipitation measurements presented in section 4.3.2. The section is divided into modeling, data analysis, the discussion of a nucleation barrier for precipitate formation, and the discussion of the transport mechanisms of Cu in bamboo interconnects.

5.2.1 Modeling

In the following, a model is introduced that describes Cu motion based on standard expressions for electromigration and diffusion. The model will be used to fit the precipitate size data presented in section 4.3.2. The precipitation measurements showed that the Cu redistribution upon current reversal could be divided into a saturation stage, and a constant drift stage. The Cu distribution after current reversal if no precipitate had formed at the new anode end of segments (nucleation barrier), and the Cu distribution during the back-flux experiment without current are treated separately.

The flux of Cu atoms in an Al interconnect is subject to a number of driving forces. For the sake of simplicity, only the electromigration driving force and the chemical potential gradient due to the Cu concentration gradient are considered and contributions due to stress or vacancy concentration gradients are ignored. In one dimension, the Cu flux is given by

$$J = \frac{D_{Cu}}{kT}\left(c|Z^*_{Cu}|e\rho j - kT\frac{\partial c}{\partial x}\right) , \tag{5.14}$$

where c is the Cu concentration in solution, and D_{Cu} is the effective diffusivity of Cu along the line. Flow direction is from left to right (positive x). For the Cu drift velocity due to electromigration, the following shorthand notation will be used

$$v_{Cu} = \frac{D_{Cu}}{kT}|Z^*_{Cu}|e\rho j \ . \tag{5.15}$$

Using the above equation for the Cu flux, the evolution of the Cu concentration can be calculated using Ficks 2$^{\text{nd}}$ Law

$$\frac{\partial c}{\partial t} = -\frac{\partial J}{\partial x} = D_{Cu}\frac{\partial^2 c}{\partial x^2} - v_{Cu}\frac{\partial c}{\partial x} \tag{5.16}$$

and by imposing the appropriate boundary conditions. It is assumed that interface reaction kinetics are sufficiently rapid so that the concentration of Cu directly next to a precipitate is fixed at the solubility concentration, c_s. Since the total amount of Cu in each segment is conserved, it is required that the sum of Cu atoms in solution plus those in the precipitates remain constant,

$$c_0 L = c_p \Delta L + \int_0^{L-\Delta L} c(x)\, dx \ , \tag{5.17}$$

where c_0 is the initial Cu concentration, c_p is the Cu concentration in the Θ-Al_2Cu phase, L is the segment length, and ΔL is the precipitate length.

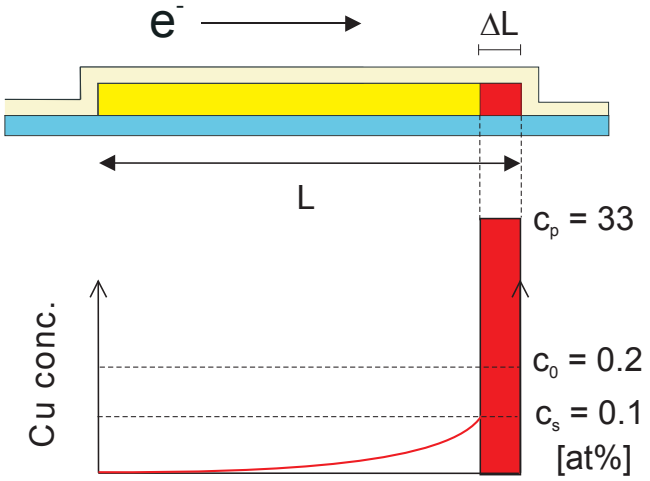

Figure 5.13: *Saturation stage.* The Cu has migrated in the direction of the electron flow. After sufficiently long times, the flux due to electromigration and the backdriving flux due the concentration gradient cancel. Only a small fraction of the total Cu content remains in solution depending on the solubility and electromigration driving force. The solubility c_S at 250°C is roughly 0.1 at%. ΔL refers to the precipitate length, and L to the segment length.

At *saturation*, the electromigration-induced flux and the concentration gradient-induced flux counterbalance each other, such that the total flux is zero. It is assumed that a precipitate is present at the anode end of the segment, as illustrated in Figure 5.13. In this case, it follows from equation 5.14 that

$$c(x) = c_S \exp\left(-\frac{|Z^*_{Cu}|e\rho j}{kT}\left(L - \Delta L - x\right)\right) , \tag{5.18}$$

where c_S is the solubility concentration. Hence, equation 5.17 can be written as

$$c_0 L = c_p \Delta L + c_S \frac{kT}{|Z^*_{Cu}|e\rho j}\left(1 - \exp\left(-\frac{|Z^*_{Cu}|e\rho j}{kT}(L - \Delta L)\right)\right) . \tag{5.19}$$

The precipitate length ΔL can be calculated from this equation.

During the *constant drift stage*, the Cu flux is constant and there are precipitates present at both ends of the segment as illustrated in Figure 5.14. Equation 5.14 then requires that $c = c_S$ everywhere between the precipitates and the Cu drift velocity is given by equation 5.15. The dissolution/growth rate of the two precipitates is then given by

$$\frac{\partial(\Delta L)}{\partial t} = \frac{c_s}{c_p}\frac{D_{Cu}}{kT}|Z^*_{Cu}|e\rho j . \tag{5.20}$$

The *back-flux* experiment is illustrated in Figure 5.15. The current was turned off after the precipitate had reached *saturation*. The only driving force acting on the Cu in solution is that due to the Cu concentration gradient. When the current is first turned off, the Cu solute distribution is described by equation 5.18, representing the

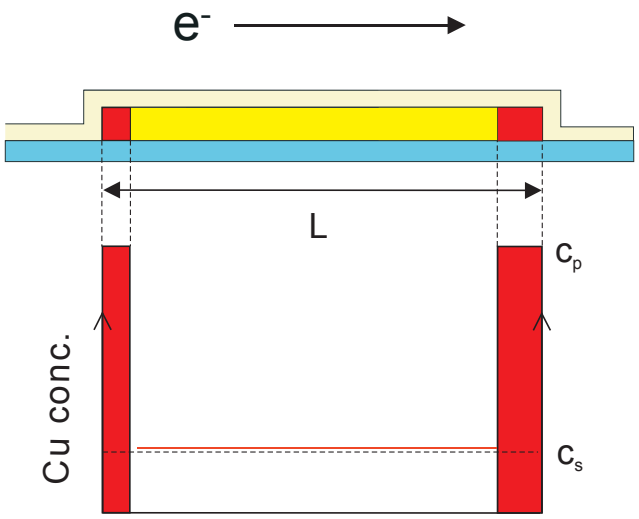

Figure 5.14: *Constant drift stage.* After a new precipitate was formed at the new anode end, both ends contain precipitates. In this case, the Cu concentration between the two precipitates is constant at the solubility concentration along the entire length of the segment.

initial Cu distribution when the diffusion experiment begins. The Cu will then diffuse back from the precipitate until the concentration c_S is reached along the entire length of the segment, resulting in dissolution of the precipitate. The rate of dissolution of the precipitate can be calculated analytically using Ficks 2$^{\text{nd}}$ Law (equation 5.16). The concentration at the precipitate is kept at the solubility $c(0,t) = c_S$, whereas the flux is blocked at the other end of the segment ($\partial c(L,t)/\partial x = 0$). This case is treated

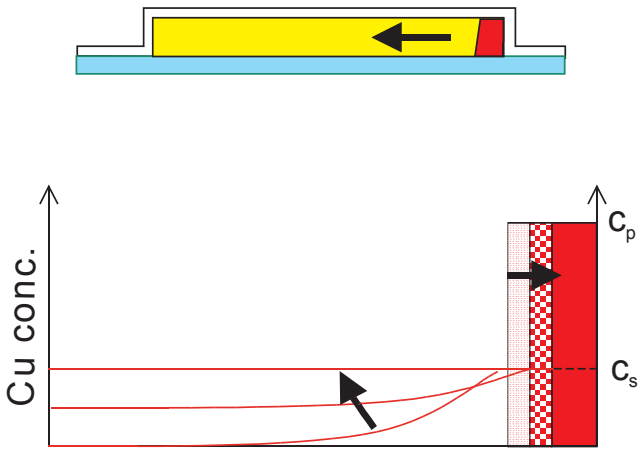

Figure 5.15: *Back-flux* of Cu at no current. Cu atoms are being driven back due to the concentration gradient. The Cu concentration along the length of the segment will reach the solubility.

in analogy to a constant heat source at $x = 0$ in a one-dimensional slab of length L, which is isolated at $x = L$. The evolution of the Cu concentration as a function of position and time is then given by [Carslaw and Jaeger, 1959, § 3.4]

$$c(x,t) = c_S + \frac{2}{L}\sum_{n=0}^{\infty} c_S \frac{2L}{m_n} e^{-\frac{D_{Cu} m_n^2 t}{4L^2}} \cos\left(\frac{m_n x}{2L}\right)\left((-1)^{(n+1)} + e^{\frac{|Z^*_{Cu}| e \rho j_o (x-L)}{kT}} \sin\left(\frac{m_n}{2}\right)\right) , \tag{5.21}$$

where $m_n = (2n+1)\pi$ and j_o is the current density used before turning the current off. The Cu distribution $c = c(x,t)$ can be used to calculate the time dependent precipitate size, using equation 5.17. It is worth mentioning that the diffusion coefficient obtained from this experiment is practically independent of Z^*_{Cu}, because only the very small fraction of the Cu that remains in solution at saturation before turning the current off depends on Z^*_{Cu}.

5.2.2 Data analysis

The data at the saturation stage (Figure 4.18) were fit using equations 5.18 and 5.19. All of the parameters were fixed, except Z^*_{Cu}, c_S,, and c_0, which were optimized using a standard fit software (Microcal Origin, version 6.0) to give the best fits to the data, which are shown as solid lines in the Figure. The precipitate sizes at saturation do not depend on D_{Cu}. The data shown in Figure 4.21 were fit using equation 5.20. The values for Z^*_{Cu}, c_S,, and c_0, from the saturation stage fit were used, whereas D_{Cu} was varied to give the best fit to the data. The resulting values of the fitting procedure are listed in Table 5.1. The best value for the effective valence is Z^*_{Cu}=(-14± 2),

ρ	$2.7\,\mu\Omega$cm	
c_p	33 at%	
T	523 K	
Z^*_{Cu}	-14	± 2
c_0	0.23 at%	± 0.01 at%
c_S	0.1 at%	± 0.01 at%
D_{Cu}	$1.5 \cdot 10^{-14}$ m^2/s	± $0.4 \cdot 10^{-14}$ m^2/s

Table 5.1: Fit parameters used. The last four values were varied to give the best fit to the model. The errors of the fitting procedure are listed in the right column.

which agrees reasonably with previously reported values (-4..-15)[Blech, 1977], (-16)[Ho and Howard, 1974], (-10..-26)[Reddy et al., 1978] but it is somewhat larger than calculated values (-4..-6)[van Eck et al., 1995, Dekker, 1997]. The best value for the equilibrium Cu solubility at 250°C is c_S=(0.1±0.01) at%, which agrees reasonably well with the value of 0.09 at% obtained from standard references [Massalski, 1990, p. 141]. The best value for the initial Cu concentration is c_0=(0.23±0.02) at%, which agrees reasonably with the Cu concentration in the films from which the segments were patterned (0.21 at%). It has recently been observed that excess Cu can be concentrated in the side-wall material of lines [Li et al., 1998]. These side-walls are generated during patterning by reactive ion etching. This excess Cu then may diffuse into the Al line during a subsequent anneal and raise the Cu concentration. Due to this fact it is best to allow c_0 to be a fit parameter.

5.2.3 Nucleation barrier for precipitation

As illustrated in Figure 4.20, precipitates were not observed to form in short segments at low current densities. In the following it is shown that this behavior is a consequence of a nucleation barrier for precipitate formation. In some segments that contained a precipitate at the cathode end due to previous current application (circles in Figure 4.20), no precipitate was observed at the new anode end. This behavior did not change even after 150 hrs of constant current stressing and the dissolution of the cathode end precipitates did not further progress. It is therefore assumed that the steady state Cu distribution had been reached in the segments. The Cu distribution in this situation is illustrated in Figure 5.16. The Cu concentration at the anode end at steady state is higher than at the cathode end. In the case of a precipitate at the new cathode

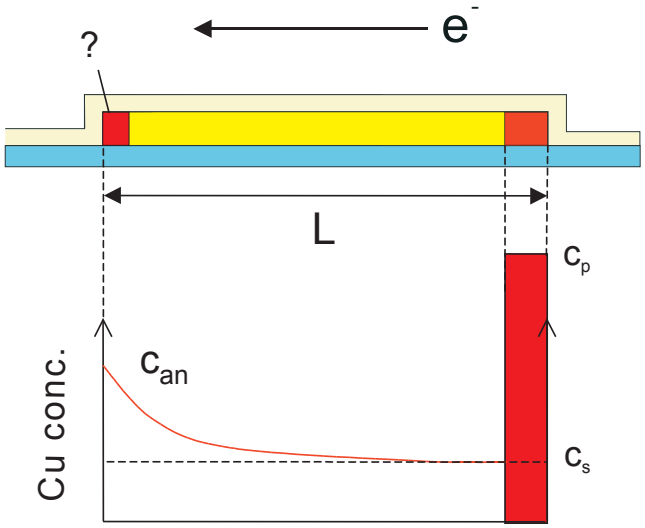

Figure 5.16: Cu distribution after current reversal and no formation of a new precipitate at the new anode end. After sufficiently long time, the Cu concentration at the new anode end is higher than the solubility.

end, and no precipitate at the new anode end, the steady-state Cu distribution along the length of the segment is given by

$$c(x) = c_S \exp\left(\frac{|Z^*_{Cu}|e\rho j}{kT}\left(L - \Delta L - x\right)\right) , \tag{5.22}$$

which is basically the same steady-state expression as equation 5.18 with the opposite sign in the exponent. The maximum Cu concentration at the anode end is therefore given by

$$c(0) = c_S \exp\left(\frac{ej|Z^*_{Cu}|\rho(L - \Delta L)}{kT}\right) . \tag{5.23}$$

Since ΔL is small compared to L, equation 5.23 can be rewritten as

$$(jL)^{ppt} = \frac{kT}{|Z^*_{Cu}|e\rho} \ln\left(\frac{c^*}{c_s}\right) , \tag{5.24}$$

where c^* is the critical Cu concentration required to nucleate a new precipitate at the anode end. Precipitates were formed if $(jL) > (jL)^{ppt}$ (Figure 4.20). Using the experimentally determined value for $(jL)^{ppt}$ of 960 A/cm, a value for c^*/c_s of 2.2 is obtained. In other words, a supersaturation of roughly two times the equilibrium solubility is required to form a precipitate.

That a supersaturation is required for precipitate nucleation is expected due to the Gibbs-Thompson effect. The required supersaturation can be estimated using a free enthalpy change of -3200 cal/g-atom [Hultgren et al., 1992, p. 153] as an approximation for the free energy change for the reaction, and using a volume change of -9% for the misfit strain energy, which was calculated from the difference in unit cell volumes between the fcc Al matrix and the Θ-Al_2Cu phase, and an interface energy of 0.5 J/m^2. The critical radius for nucleation is given by [Porter and Easterling, 1992, p. 266]

$$r_c = \frac{16\pi\gamma^3}{3(\Delta G_V - \Delta G_S)^2} \ , \tag{5.25}$$

where γ is the interface energy, ΔG_S the misfit strain energy, and ΔG_V the free energy change. From equation 5.25 one obtains roughly 3 nm as the critical nucleus radius. The solubility as a function of particle size due to the Gibbs-Thompson effect is given by [Porter and Easterling, 1992, p. 47]

$$c_S(r) = c_\infty \exp\left(\frac{2\gamma V_m}{RTr}\right) \ , \tag{5.26}$$

where V_m is the molar volume of the particle phase, R the universal gas constant, and c_∞ the solubility for a planar interface. A particle of 3 nm radius results in a required supersaturation of a factor of 4, which is not very different from the value obtained here.

The existence of a nucleation barrier implies that precipitate formation can be significantly reduced during thermal treatment of thin Al(Cu) films, in particular at low Cu concentrations. The total Cu content in the film (0.5 wt%) is roughly two times the solubility at 250°C. The required supersaturation was determined to be on the same order. Thus, the nucleation rate at 250°C is expected to be small. Precipitates were observed in contact pads after annealing at 250°C for 1300 hrs, with an areal precipitate density of 0.003/ μm^2. No precipitates were observed in 1000 μm length of the 0.5 μm wide lines after annealing. If the nucleation rate in the pad and in the lines was the same, only one observable precipitate would be expected in a line of this width and length, consistent with the observations. In thin Al(Cu) films at deposition temperatures between 100 and 400°C, a precipitation suppression at low temperatures

and low Cu concentrations has been reported [Marcus and Bower, 1997], as shown in Figure 2.4. The authors explained this behavior by solute trapping during deposition. A nucleation barrier adds to the solute trapping effect.

5.2.4 Transport mechanisms of Cu

The best value from the fit above (Figure 4.21) for the effective diffusivity of Cu at 250°C is $(1.5 \pm 0.4) \cdot 10^{-14}$ m^2/s. For comparison, a number of values were compiled from the literature, which are shown in Figure 5.17. This diffusivity is comparable to previously reported values for Cu in Al during electromigration and diffusion measurements in polycrystalline [Hu et al., 1993a, Reddy et al., 1978, Shaw et al., 1995], bamboo [Witt and Volkert, 1997] (described in section 5.3.2.1), and single crystal lines [Srikar and Thompson, 1998]. However, the value is 3-4 orders of magnitude larger than the values reported for Cu diffusion in the Al lattice in both thin films ($1.3 \cdot 10^{-17}$ m^2/s at 250°C [Chamberlain and Lehoczky, 1977]), and in bulk samples ($3 \cdot 10^{-18}$ m^2/s at 250°C [Peterson and Rothman, 1970]). This strongly suggests that some transport mechanism other than lattice diffusion, is the dominant mechanism. Since the microstructure of the interconnects is bamboo, no continuous grain boundary paths are available.

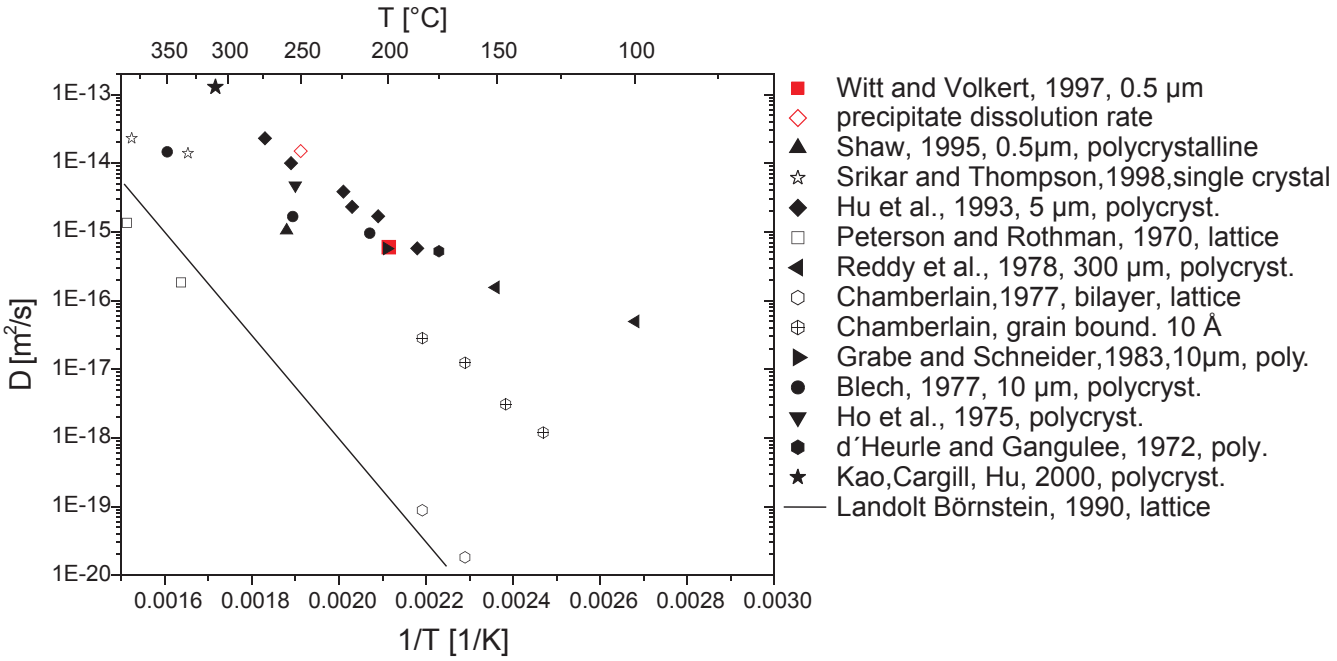

Figure 5.17: Summary of Cu diffusion coefficients in Al obtained from diffusion (open symbols) and electromigration (filled symbols) measurements in thin film and bulk samples. All samples were polycrystalline except in the studies Srikar and Thompson, and Witt and Volkert.

Other transport paths, which possibly contribute to the transport of Cu are dislocation core diffusion, and interface diffusion. Considerable dislocation core diffusion occurs for dislocation densities on the order of $10^{15}/\mathrm{m}^2$ [Hu et al., 1995, Kaur and Gust, 1990], which is much higher than what was observed by TEM ($< 10^{14}/\mathrm{m}^2$) [Rose et al., 1991, Hu et al., 1995]. The diffusion coefficient presumably represents the effective value when interface diffusion is important. Interface diffusion coefficients for Al interconnects have not been reported. The interface diffusion coefficient D_i can be approximated by

$$D_i \approx D_{Cu} \left(2\delta_i(1/w + 1/t)\right)^{-1} \ , \tag{5.27}$$

where w and t are the interconnect width and height, and δ_i the interface width. In writing this equation, it has been assumed that the different interfaces have the same diffusion coefficient and width. From the D_{Cu} value obtained from the constant drift stage, one obtains a value of $D_i \approx 3 \cdot 10^{-12}$ m^2/s, using 10 Å for δ_i.

The rate of precipitate dissolution during the *back-flux* experiment (Figure 4.22) is explained in the following by rapid interface diffusion and subsequent slow lattice diffusion. Although interface Cu concentrations can be on the order of 0.1 monolayers (at 260°C for Al(Cu)/Al_2O_3 [Copel et al., 1996]), the total number of Cu atoms that can be deposited in the interfaces is only on the order of 10^8 atoms for the 100 μm long segments. This number corresponds to a precipitate size change of roughly 0.02 μm, which is too small to explain the observed precipitate dissolution. To explain the precipitate dissolution observed, Cu must have diffused into the lattice during the experiment. So far, the diffusion was treated in a one-dimensional model, using an effective diffusion coefficient D_{Cu}. The fast transport along the interconnect interfaces with slow lattice diffusion is more complicated. The time scale of the dissolution of the precipitates in the 100 μm long segments was on the order 100 hours. The time for the Cu to diffuse out of the precipitate along the interface of the 100 μm long segment is $t \approx L^2/D_{int} \approx 3$ hours, using $3 \cdot 10^{-12}$ m^2/s for D_i. This time is too short to explain the observed behavior. By estimating the diffusion length $l = \sqrt{D_l t}$ in the Al lattice, using a standard value for the lattice diffusion coefficient $D_l \approx 3 \cdot 10^{-18}$ m^2/s [Peterson and Rothman, 1970], it becomes clear that the Cu diffused only $\sim$0.1 μm into the Al bulk on a time scale of 3 hours. In a simple picture, Cu diffuses rapidly along the interfaces and then more slowly into the lattice, as illustrated in Figure 5.18. Then, the dissolution of the precipitate is roughly rate-controlled by lattice diffusion with an effective coefficient that depends on the total interface area, and therefore on the segment length. It is assumed that the Cu flux along the interfaces and from the

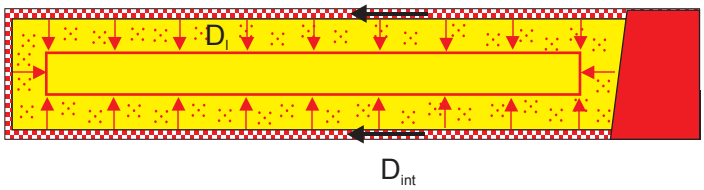

Figure 5.18: Schematic of Cu diffusion into the interconnect. Since the transport along the interfaces is rapid, the slow diffusion into the Al bulk controls the rate by which the precipitate dissolves.

interfaces into the lattice are the same, such that the amount of Cu that diffused into the lattice during the initial short period can be neglected. The effective diffusion coefficient is then given by

$$D_{Cu} = 2LD_l \left(\frac{1}{t} + \frac{1}{w}\right) . \tag{5.28}$$

This coefficient was used in equation 5.21 to fit the precipitate dissolution data for the 100, 50, and 25 μm long segments in Figure 4.22. The diffusion coefficient D_l that follows from the fit is $1 \cdot 10^{-17}\,\mathrm{m}^2/\mathrm{s}$. This agrees reasonably with the literature values for lattice diffusion, which range between $3 \cdot 10^{-18}\,\mathrm{m}^2/\mathrm{s}$, and $1.3 \cdot 10^{-17}\,\mathrm{m}^2/\mathrm{s}$ at 250°C [Peterson and Rothman, 1970, Landolt and Börnstein, 1990, Chamberlain and Lehoczky, 1977].

The solubility concentration of c_S= 0.23 wt% from the steady state fit described above was used, which is close to the value expected for the lattice solubility. This suggests that the interface solubility in these interconnects is not very different from the lattice solubility, such that segregation of Cu to the interfaces is not important in these interconnects.

5.2.5 Conclusions

- The Cu precipitation observed is consistent with a simple model based on standard expressions for electromigration and diffusion.
- The results indicate that a critical supersaturation of Cu of roughly 2.2 times the solubility is required to form a precipitate, which is expected from classical nucleation theory.
- The analysis of the precipitation kinetics showed that interface diffusion along the length of the segment is an important transport path, such that diffusion of Cu atoms into the Al lattice can become rate controlling.

5.3 Above threshold

In this section the evolution of damage in segments above the threshold is analyzed. It is divided into a discussion on the incubation time to form a void and the drift behavior after damage formation. Because of the length effect on drift, the second subsection is further divided into long and short segments, for both pure Al and Al(Cu).

5.3.1 Incubation time

From the models for electromigration it is expected that a certain time of electromigration testing is required to build up sufficiently high stresses to create damage [Shatzkes and Lloyd, 1986, Korhonen et al., 1993b]. In the case of very long segments (mathematically semi-infinite), the time to achieve a critical stress is predicted by the models to scale with the current density as $1/j^2$. A $1/j$ dependence for the time to form voids in a continuous line has been reported [Doan et al., 1999a]. This is in contrast to the theoretical predictions. These measurements were performed in passivated, polycrystalline pure Al lines by monitoring the resistance and performing concurrently direct observations by backscattered electron imaging. The resolution of 50 nm as the smallest void that could be detected is comparable to the one in this work. By using $t_{\mathrm{inc}} \sim j^{-n}$ as a more general expression to fit the incubation times measured in this work, (squares in Figure 4.25), an exponent of $n = 1.9$ is obtained, which is in good agreement with the theoretical prediction, but in contrast to the cited measurements. It is possible that in the cited measurements void growth instead of void nucleation was the rate-controlling mechanism. If nucleation is rapid and growth is slow, an exponent n close to 1 is expected. If the void nucleation rate is small and growth is rapid, an exponent close to 2 is expected. Which process dominates probably depends on details of the interconnect microstructure.

Using the Korhonen model, the stress evolution is given by equation 2.13, and the time to reach a certain stress at the cathode end is given by equation 2.15. This equation was used to fit the incubation times in the passivated segment as shown in Figure 4.25. The parameters used are listed in Table 5.2. From the fit, a critical stress σ_{cr} for void formation is obtained. The fit results in a value of $\sigma_{cr} = (160 \pm 30)\,\mathrm{MPa}$ using $Z^* = -2$ and $D = 1 \cdot 10^{-14}\ \mathrm{m^2/s}$. The values for Z^* and D were obtained from other measurements (drift velocity and back-flux) as discussed below in the next section and in section 5.3.2.3. The critical stress obtained here agrees reasonably with results from *in-situ* strain measurements (200-250 MPa) [Wang et al., 1998].

ρ	$2.7\,\mu\Omega$cm
Ω	$1.67 \cdot 10^{-29}\,\mathrm{m}^3$
B	30 GPa
T	523 K
Z^*	-2
D	$1.0 \cdot 10^{-14}\ \mathrm{m}^2/\mathrm{s}$

Table 5.2: Parameters used to fit the incubation time data.

From the incubation time measured in the unpassivated segment (circle in Figure 4.25), and using the parameters listed in Table 5.2, a critical stress of (130±30) MPa is obtained. Within the experimental uncertainty the critical stress for void formation in passivated, and unpassivated pure Al is roughly the same.

5.3.2 Drift

5.3.2.1 Long segments

Long segments are defined as those which are much longer than the critical length at a given current density. In other words, with sufficiently long segments, the stress gradient-induced back-flux (Blech-Herring model) can be neglected, and the drift velocity is proportional to the current density (equation 1.2). Because of the influence of the Cu, this section is divided into pure Al and Al(Cu). The effect of the passivation on drift is discussed in the first part on pure Al.

Pure Al

A passivation layer has a beneficial effect on the electromigration lifetime [Black, 1967, Spitzer and Schwartz, 1969]. A reduction in the self-diffusivity due to compressive stresses imposed by the passivation layer according to equation 2.26 was proposed to explain this effect [Lloyd and Smith, 1983, Ross et al., 1989]. To give an example, from equation 2.26 it is expected that D decreases by 20% for 100 MPa hydrostatic compression at 500 K. It is well known that the deposition of a passivation layer modifies the stress state of the Al [Besser, 1999]. In particular, the hydrostatic stress is increased in lines with passivation. Thus, a different drift velocity might be expected for long passivated vs. long unpassivated Al segments.

It was observed that the drift velocities in both the passivated, and unpassivated 800 μm long pure Al segments were constant with time. The drift velocity measurements (Figure 4.26) show that they are proportional to the current density, and obey

equation 1.2. The results indicate that the passivation has no large effect on the drift velocity. The effect observed in lifetime measurements is therefore probably due to the increase in the threshold for damage formation.

From the drift velocity measurements a value for the product $D\,Z^*$ can be obtained. The linear slopes shown in Figure 4.26, and using equation 1.2 result in a value of $22.4 \cdot 10^{-14}\,\mathrm{m}^2/\mathrm{s}$. Using a value for the diffusion coefficient from a back-flux experiment (discussed in section 5.3.2.3) of $D = 1 \cdot 10^{-14}\,\mathrm{m}^2/\mathrm{s}$, an effective valence of -2 for pure Al is obtained.

Al(Cu)

For polycrystalline Al(Cu), mass transport is well documented to occur in sequential stages [Grabe and Schreiber, 1983, Hu et al., 1993a, Spolenak et al., 1998b]: an incubation period (attributed to Cu depletion beyond a critical length) followed by the Al drift stage, as illustrated in Figure 5.19. Commonly, the incubation effect on the

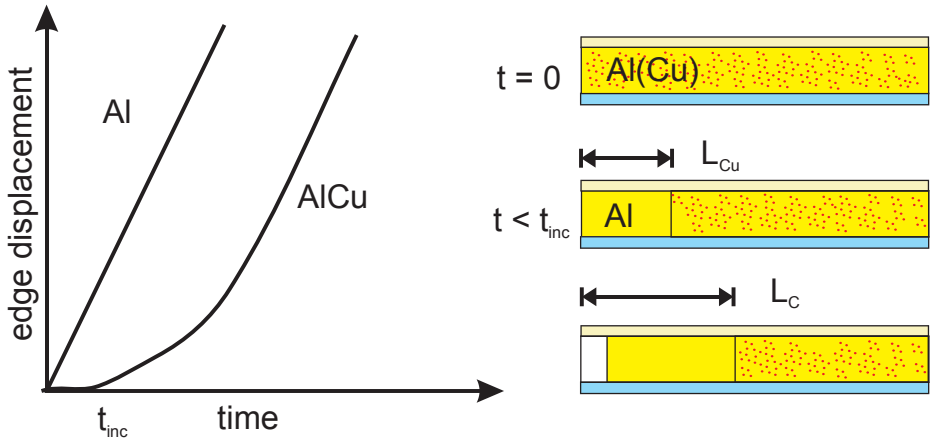

Figure 5.19: Influence of Cu on drift: Al depletion is very slow or zero as long as Cu has not been depleted over a threshold length from the cathode end of a segment. Then, the Al drift velocity increases and might reach the value of pure Al.

cathode end displacement was attributed to the retardation of Cu in grain boundaries [Rosenberg, 1972]. For bamboo Al(Cu) interconnects, the results in the literature are not consistent [Hu, 1995, Proost et al., 1998], such that it is not clear whether Cu has an impact on the Al drift.

In long Al(Cu) segments it was observed that the drift velocity is not constant with time, such that it cannot be simply described by equation 1.2. Instead, if Cu drifts

more quickly than pure Al, the drift velocity can be written as [Hu et al., 1993a]

$$v_d = v_{Al} + v_{Al(Cu)} \ , \tag{5.29}$$

where $v_{Al} = 0$ as long as the Cu depleted length $L_{Cu} < L_C$ and

$$v_{Al} = v_{Al}^o(1 - L_C/L_{Cu}) \tag{5.30}$$

once the Cu depleted length is longer than the threshold length ($L_{Cu} > L_C$). The length L_{Cu} is given by $v_{Cu}t$ where v_{Cu} is the drift velocity of Cu in Al(Cu), which is given by equation 5.15. v_{Al}^o is the drift velocity of pure Al, and $v_{Al(Cu)}$ is the drift velocity of the alloy. In writing these equations, it has been assumed that the Al diffusivity abruptly increases to the pure Al value once the Cu is depleted and that the back-flux due to stress gradients follows the steady state form proposed by Blech [Blech, 1976].

The best fit from applying this model to the edge displacement data for the unpassivated, 0.5 μm wide, and 50 μm long Al(Cu) segments (Figure 4.27) is shown in Figure 5.20. A value of 15 μm for L_C was used, because the longest segments that were

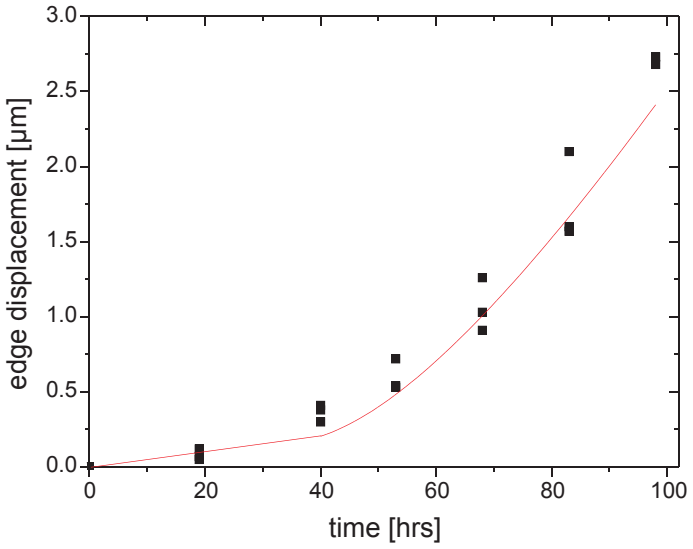

Figure 5.20: Edge displacement in unpassivated, 50 μm long Al(Cu) segments. The drift velocities used to fit the data were $v_{Al(Cu)} = 5$ nm/hr for the alloy, $v_{Al}^o = 59$ nm/hr for pure Al, and $v_{Cu} = 375$ nm/hr for the Cu.

not damaged were 10 μm long, and the shortest damaged segments were 20 μm long. The fit yields values for v_{Al}^o, $v_{Al(Cu)}$ and v_{Cu}, which are listed in the Figure caption. Using the value from the fit for v_{Cu} and a value of -14 for Z_{Cu}^* (section 5.2.2), the predicted Cu diffusivity at 200°C is $D_{Cu} = 6 \cdot 10^{-16}$ m^2/s. For comparison this value

was included in Figure 5.17. Standard values for the diffusivity for lattice diffusion are roughly 3 orders of magnitude smaller. This is consistent with the result obtained above from the precipitation measurements at 250°C. The fact that an increase in the drift rate was also observed in the present samples suggests that Cu plays the same role in inhibiting or slowing Al drift in bamboo lines as it does in polycrystalline lines.

5.3.2.2 Transport mechanisms of Al

Pure Al

In polycrystalline Al lines at a homologous temperature of $T/T_m = 0.5$, the dominant mass transport path is along the grain boundaries [Frost and Ashby, 1982, p. 26]. Since no continuous grain boundary network is present in bamboo interconnects, other transport paths must be important. To compare the drift velocities obtained in this work, a number of drift velocities were compiled from the literature as shown in 5.21. The drift velocities measured in passivated and unpassivated pure Al are comparable to drift velocities reported for polycrystalline interconnects. Furthermore, the pure Al diffusivity of $1.0 \cdot 10^{-14}\,\mathrm{m}^2/\mathrm{s}$ at 250°C obtained from the back-flux experiment (discussed below) is comparable to recent measurements in polycrystalline lines ($8 \cdot 10^{-15}\,\mathrm{m}^2/\mathrm{s}$ at 260°C) [Wang et al., 1998]. This suggests that for the pure Al segments, a fast transport mechanism is important. As discussed for the transport mechanism of Cu, dislocation pipe diffusion is unlikely to contribute significantly to Al transport. Hence, the drift velocities obtained here presumably represent the effective values when interface diffusion is important.

Al(Cu)

The fast drift velocity in unpassivated Al(Cu), after the Cu has been depleted as described in the previous section (denoted as AlCu (fast) in Figure 5.21), is also comparable to polycrystalline interconnects. This indicates that interface diffusion is important, as in the case of pure Al segments. However, the drift velocity obtained for these segments during the early slow motion stage (denoted as AlCu (slow) in Figure 5.21) compares well with the values reported in the literature for bamboo lines. It should be noted that in all studies on bamboo lines, Al(0.5-1 wt% Cu) alloys were used. The diffusion coefficient for Al(Cu) can be estimated using equations 5.29 and 1.2 to be $3 \cdot 10^{-17}\,\mathrm{m}^2/\mathrm{s}$ at 200°C, using $Z^* = -2$. This is not very different from standard values for the diffusion coefficient for the Al lattice (between $2 \cdot 10^{-19}\,\mathrm{m}^2/\mathrm{s}$

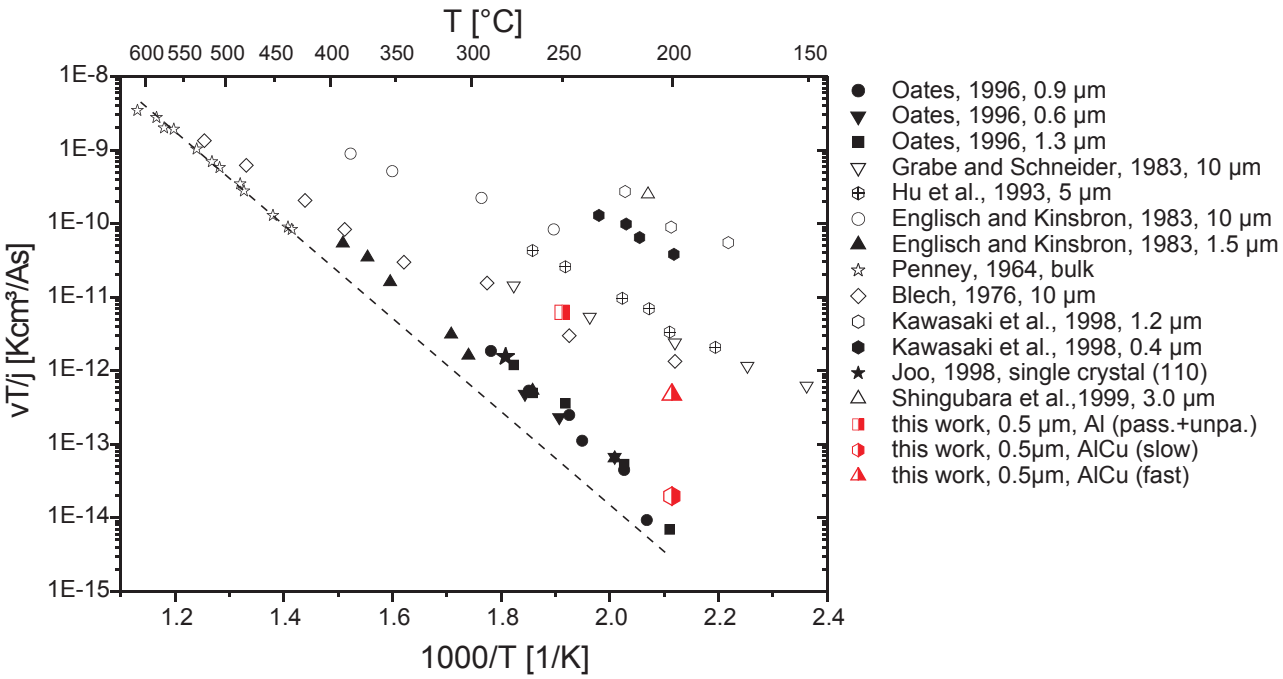

Figure 5.21: Normalized electromigration drift velocities. The thin film data include bamboo (filled symbols) and polycrystalline (open symbols) values. The drift velocities obtained in this work are indicated by half filled symbols. In all bamboo cases, Al(Cu) alloys were used (table 2.1). The dashed line indicates the extrapolation from bulk measurements.

and $7 \cdot 10^{-18}\,\mathrm{m}^2/\mathrm{s}$ [Peterson and Rothman, 1970, Frost and Ashby, 1982]). For comparison, the extrapolation to lower temperatures from bulk measurements is included in Figure 5.21 as dashed line. The temperature dependence of the bamboo data shows an activation energy, which is similar to the value for lattice diffusion (1.26 eV). This suggests that in bamboo Al(Cu) lines, transport occurs predominantly via the Al lattice, indicating that the Cu slows Al drift significantly in the interfaces in bamboo interconnects.

5.3.2.3 Short segments

Short segments are defined as those for which the back-flux due to the stress gradient substantially modifies the drift behavior, such that saturation is observed. Depletion in unpassivated segments only slows down when the length approaches the critical length at the given current density. In short, passivated segments, depletion saturates after relatively small amounts of Al are displaced, as long as the passivation is not damaged.

This is a result of the stress gradient-induced back-flux. Depletion in passivated Al and Al(Cu) segments is discussed in this section to show the effect of the back-flux and the effect of the Cu. It is divided into the evolution of voids while current is applied and after the current is turned off, and void sizes at saturation.

Void evolution in pure Al

Application of a super-critical current leads after sufficient time to the formation of a void at the cathode end of a passivated segment. The void growth eventually saturates. When the current is turned off after the void grew to saturation, a back-flux occurs such that the void closes up somewhat. This behavior is schematically shown in Figure 5.22. At saturation, the electromigration-induced flux and the stress

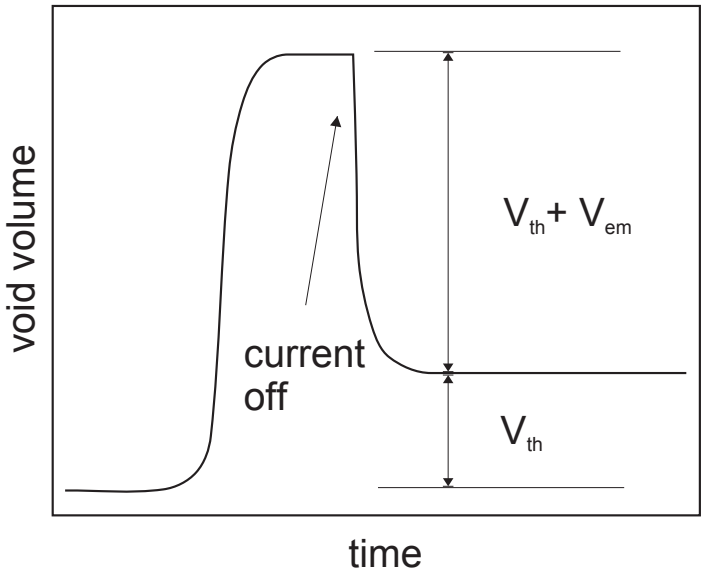

Figure 5.22: Schematic diagram of void evolution in a passivated segment. Application of current leads to formation of a void, which grows to saturation. When the current is turned off, the void closes up somewhat.

gradient-induced back-flux balance each other. When the current is turned off, the stress gradient remains, leading to the observed back-flux. This motion continues until the stress gradient is completely relaxed. The void size at saturation is, according to the Korhonen model, the sum of the volume due to electromigration (V_{em}), and the strain associated with the relaxation of the tensile thermal stresses (V_{th}). The residual volume after the back-flux occurred is then only the volume due to thermal stresses. The back-flux phenomenon was reported once in the literature [Blech, 1976]. Blech analyzed the back-flux to obtain values for the effective diffusivity and effective valence in polycrystalline, pure Al interconnects. In the following, the back-flux is analyzed to obtain these values for the present bamboo lines.

After the current is turned off, the flux of Al atoms is only subject to stress gradient-induced diffusion. The stress evolution is then described by the following differential equation:

$$\frac{\partial\sigma(x,t)}{\partial t} = \frac{D\Omega B}{kT}\frac{\partial^2\sigma(x,t)}{\partial x^2} \ . \tag{5.31}$$

For the sake of simplicity, the atomic diffusivity was taken to be stress independent. Ω is the atomic volume and B the effective modulus in the same notation as in the Korhonen model. It is assumed that the stress at the void surface is zero. The flux at the anode end is blocked. With these boundary conditions

$$\sigma(0,t) = 0 \tag{5.32}$$

$$\frac{\partial\sigma(L,t)}{\partial x} = 0, \tag{5.33}$$

a solution to equation 5.31 can be obtained by the method of Laplace transformation [Carslaw and Jaeger, 1959, § 3.4]:

$$\sigma(x,t) = \frac{2}{L}\sum_{n=0}^{\infty} e^{-\frac{Dm_n^2 t}{4L^2}}\cos(\frac{m_n x}{2L})f_1 \ , \tag{5.34}$$

where $m_n = (2n+1)\pi$. f_1 is determined by the initial stress distribution $\sigma(x,0)$ through

$$f_1 = \int_0^L \sigma(x',0)\cos(\frac{m_n x'}{2L})dx' \ . \tag{5.35}$$

The initial stress distribution is the stress profile just before turning the current off at $t = 0$. The stress distribution along the length of the segment at saturation (steady-state) is expected to be linear. A linear stress distribution is therefore used as initial distribution. The linear stress distribution can then be written as

$$\sigma(x,0) = \sigma_m - \frac{\sigma_m}{L}x \ , \tag{5.36}$$

where σ_m is the maximum stress at the anode end. The stress increment due to a relative density change dC/C in a confined metal line is given by equation 2.11:

$$\frac{dC}{C} = -\frac{d\sigma}{B} \ , \tag{5.37}$$

where B is an applicable modulus. The void volume can be calculated by integrating the volume strain as

$$V = \frac{1}{B}\int_0^L \sigma(x,0)dx \ . \tag{5.38}$$

The maximum stress σ_m can then be calculated from the measured initial void size $V(t=0)$. As mentioned, is this the sum of an electromigration induced and a stress induced volume. Hence, this initial volume needs to be corrected for the thermal fraction, in order to obtain the maximum stress σ_m correctly. The initial volume is given by

$$V(t=0) = V_{th}(\sigma_T) + V_{em}(\sigma_m) \ , \tag{5.39}$$

where σ_T is the thermal stress level before opening any void. The stress distribution $\sigma = \sigma(x,t)$ is used to calculate the time dependent void size, using equation 5.38 with $\sigma(x,t)$ in place of $\sigma(x,0)$.

The Al displacement under electromigration stressing was calculated in [Korhonen et al., 1993a]. Equation 2.22 describes the void size as a function of time with current on. This and the equations derived above were used to fit the void size while stressing and relaxing, as shown in Figure 4.28, for the case of pure Al. The parameters used for this fit are given in Table 5.3. As a result of this experiment,

ρ	$2.7\,\mu\Omega$cm
Ω	$1.67 \cdot 10^{-29}\,\mathrm{m}^3$
B	30 GPa
T	523 K
Z^*	-2
D	$1.0 \cdot 10^{-14}\ \mathrm{m}^2/\mathrm{s}$
σ_T	44 MPa

Table 5.3: Parameters used to fit the void growth and back-flux in the passivated, pure Al segment as shown in Figure 4.28.

a value for the effective diffusion coefficient D is obtained. From the value for the product DZ^* from the drift velocity measurements (section 5.3.2.1), a value for the effective valence is obtained to be -2. It is worth noting that Z^* is not well known and there has been some dispute about the magnitude of this parameter in the literature. Blech concluded from his measurements that it is on the order of -1 to -2 for pure polycrystalline Al [Blech, 1976], whereas other references give numbers of -5 to -10 [Tu, 1992]. Recent measurements of relaxation of a electromigration-induced stain gradient by X-ray microdiffraction indicate that $Z^* \approx -1.6$ [Wang et al., 1998], which agrees reasonably with the value obtained in this work for pure Al bamboo lines.

Void evolution in Al(Cu)

The Korhonen model was modified in order to understand the void evolution in passivated, Al(Cu) segments. Based on the analysis presented in section 5.2.1, predictions

for the Cu redistribution during electromigration can be made. The Cu redistribution occurs in two stages: first, any precipitates present at the beginning of the experiment have to dissolve, and then the Cu in solution migrates towards the anode, where an electromigration induced precipitate eventually is formed. Considerable Al motion and therefore damage in the Al occurs only, after the was depleted over a sufficiently long distance from the cathode end.

An upper limit for the first stage can be estimated by imagining that all precipitated Cu is present in two equally large precipitates at the ends of the segment. Due to electromigration, the cathode end precipitate dissolves whereas the other grows. This case corresponds to the *constant drift stage* as illustrated in Figure 5.14. The time to dissolve the cathode side precipitate can be estimated, using equation 5.20, to be roughly 5-7 hrs at 2 MA/cm^2 and 250°C.

In the second stage, the cathode end precipitate is dissolved, and the Cu in solution is redistributed. The Cu concentration as a function of time and position, the model described in section 5.2.1 can be used. Figure 5.23 shows the Cu concentration profiles after 0.1, 10, 20, and so forth hours of electromigration testing. By asking where the position of a certain concentration c_c is located as a function of time, the motion of the associated "Cu-front" can be calculated. This position represents the effective length

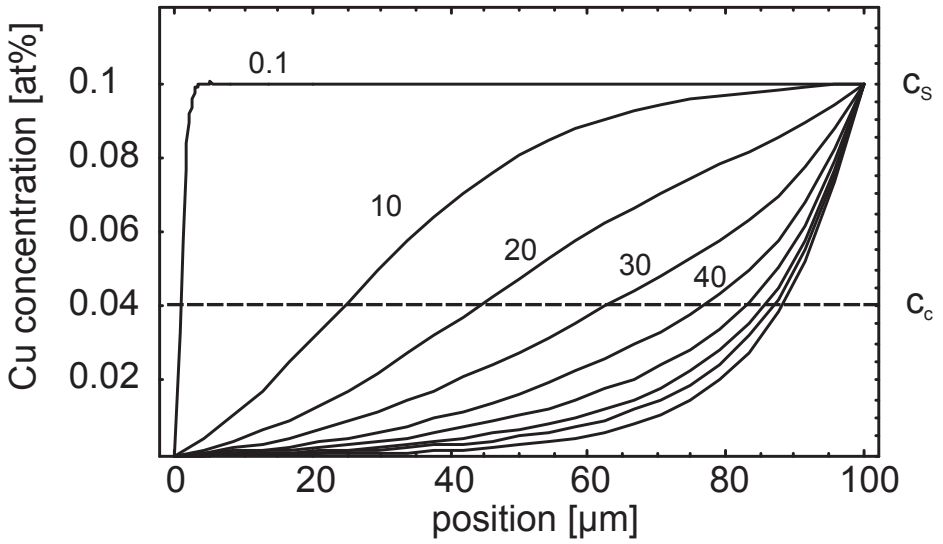

Figure 5.23: Cu concentration profiles during electromigration in a 100 μm long Al(Cu) segment at 250°C and 2.0 MA/cm^2. The anode end is kept at the solubility c_s (0.1 at%) (precipitate is present), whereas the flux is blocked at the cathode. The different profiles correspond to 0.1, 10, 20, ... , 80 hrs of electromigration.

$L_{\text{eff}}(t)$, in which the Al is allowed to move rapidly (compare Figure 5.2). Next, $L_{\text{eff}}(t)$ is used instead of the physical length L for the Korhonen model (equation 2.22). The time dependent void growth for the Al(Cu) system is obtained as shown in Figure 5.24. The curve for pure Al shown in Figure 5.24 is based on the measurement in passivated

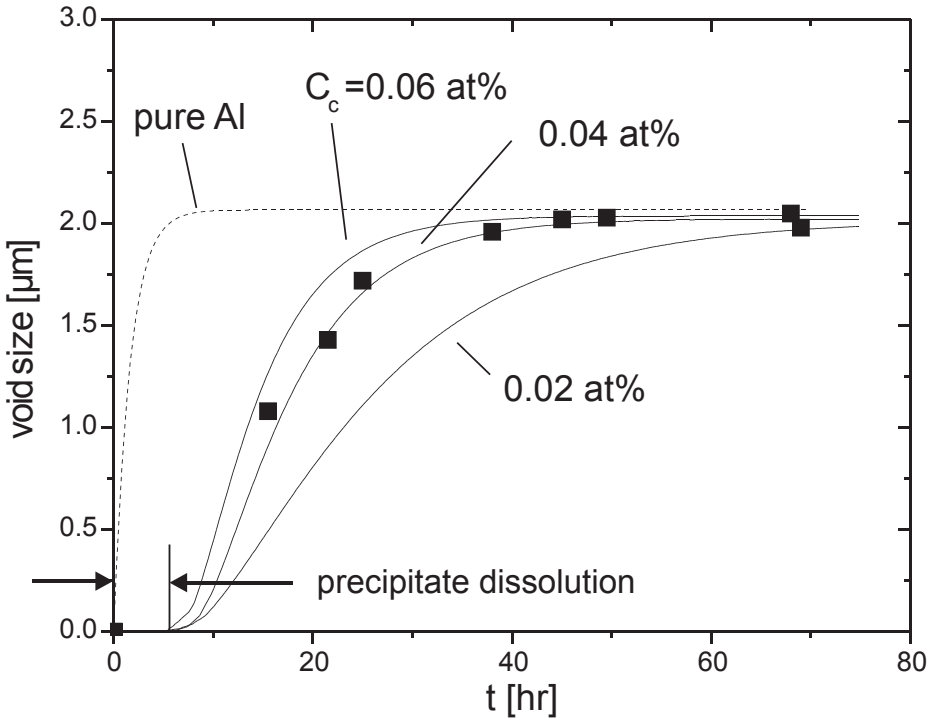

Figure 5.24: Void evolution in passivated, Al(Cu) segments during testing at 250°C and 2 MA/cm^2. For comparison, the behavior of pure Al was also plotted, calculated for current density 2 MA/cm^2.

pure Al, which was scaled to the higher current density 2.0 MA/cm^2. The incubation time for pure Al is not shown, because it is on the order of less than 1 hr. From the fit shown, a value of $c_c = 0.04$ at% for the critical Cu concentration is obtained, which is consistent with the threshold product measurements, and with the measured hillock positions. Fits for values for c_c of 0.02 and 0.06 at% were significantly worse than the fit shown.

Void size at saturation

Figure 5.25 shows the map of void sizes for passivated Al and Al(Cu) segments for various current densities. The left diagram shows the measured void sizes together with the expected sizes from the Korhonen model (equation 2.25). Obviously, the

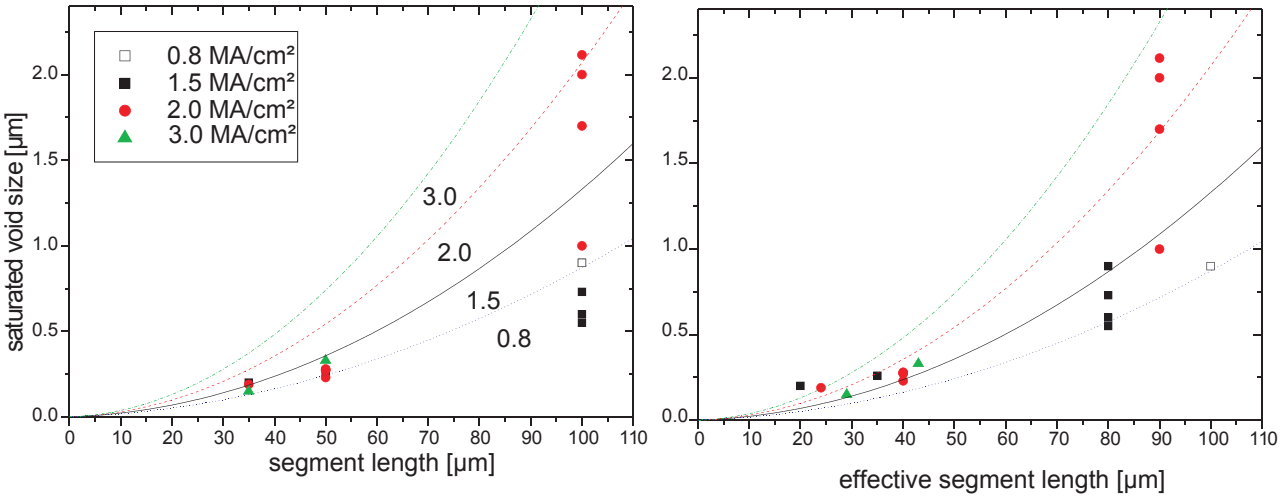

Figure 5.25: Comparison of saturated void sizes as a function of physical (left diagram) and effective (right diagram) segment length. For the modeled curves Z^*_{Al} = -2, B = 30 GPa, σ_T = 40 MPa and c_c = 0.04 at% have been used.

model predicts much larger voids than measured, although very moderate values for Z^* and the thermal stress σ_T were used. The only exception is the data point for pure Al, which agrees well with the predicted value. In order to explain the void sizes in passivated Al(Cu), the shortened effective length L_{eff} is used, as described above. The right diagram in Figure 5.25 shows the same map, but using L_{eff} instead of L. The effective lengths were calculated using equation 5.2 with c_c = 0.04 at%, and Z^*_{Cu} = -14. The agreement between measured and predicted void sizes improved. This value is consistent with the measurement of void evolution in passivated Al(Cu), the increase in threshold product, and the positions of hillocks (see section 5.1.1).

5.3.3 Conclusions

- The current density dependence of the time to form a void (incubation time) was found to obey a $1/j^2$ dependence. This is in good agreement with predictions from models of electromigration, e.g. the Korhonen model [Korhonen et al., 1993b], but in contrast to another measurement found in the literature [Doan et al., 1999a].

- From the incubation time, values for the critical stress for void formation of 160 MPa for passivated pure Al, and 130 MPa for unpassivated pure Al were obtained.

- The drift velocity in long, pure Al segments was constant with time, and proportional to the current density. This is in agreement with equation 1.2. The passivation had no effect on the drift velocity.

- In the case of long Al(Cu) segments, an increasing drift velocity was observed. The early slow motion period was attributed to the selective depletion of Cu over a critical length. The results indicate that Cu slows Al electromigration in interfaces in a similar manner as in grain boundaries in polycrystalline interconnects.

- Void sizes measured in passivated, pure Al segments are in agreement with the Korhonen model. However in the Al(Cu) samples, the reduction in Al mobility at the anode end of the interconnect, where the Cu concentration was highest, had to be included to obtain reasonable agreement between model and the data. From the analysis of the void sizes (evolution and at saturation) it was concluded that the Al mobility decreases abruptly above a critical Cu concentration of roughly 0.5 times the solubility. This picture is consistent with the finding of an increased threshold product of Al(Cu), and with the observation that hillock formation occurred at some distance from the anode end.

- A back-flux occurs in passivated segments after the current is turned off. From the analysis of this data, a value of -2 for the effective valence for pure Al, and $1 \cdot 10^{-14}\,\mathrm{m}^2/\mathrm{s}$ for the effective diffusivity of Al at 250°C were obtained.

6

Summary

In the present work, electromigration-induced damage in bamboo Al interconnects was quantitatively investigated in an attempt to better understand the effect of passivation layers and the addition of Cu. Experiments were performed on 0.5 μm wide Blech-type segments made from pure Al and from Al(0.5 wt% Cu), both passivated and unpassivated. The interconnects consisted of bamboo Al and Al(Cu) segments of lengths varying between 30 and 800 μm patterned on continuous TiN stripes. Electromigration testing was performed for current densities between 0.04 and 5 MA/cm^2 at temperatures of 200 and 250°C and electromigration-induced damage, such as voids, hillocks and passivation cracking were observed *in-situ* in an SEM.

First, the threshold values of the product of the current density and segment length, above which damage occurs, were measured for the different sample types. The results showed that the addition of Cu increases the threshold product for the case of passivated segments. In addition, hillocks formed directly at the anode end of pure Al segments, whereas they formed at some distance from the end of Al(Cu) segments. Both observations are consistent with the model of a Cu-front that leads to an effective segment length shorter than the physical length. It was also observed that the passivation increases the threshold product, which could be attributed to the suppression of hillocks.

For the first time, the statistical distribution of threshold products vs. segment length was investigated. The measurements were performed on a set of unpassivated, pure Al segments. The results of this effort showed that the *mean* threshold product is not significantly dependent on the segment length, but that the *deviation* of the threshold product increases with decreasing length. A modification of the well known

concept of a threshold stress, above which damage occurs (Blech-Herring model), was suggested to explain this behavior. The model introduces the idea that the threshold stress for damage formation does not have a single value, but depends on local microstructure and thus scatters around a mean value along the length of the interconnect. Since the threshold stress gradient is shallower in longer segments, there are more sites with a threshold stress comparable to the electromigration-induced stress. Therefore, the chance of damage formation is larger, and the dispersion in the measured value is smaller. Observations of the damage morphology showed that voids were located further away from the cathode end in longer segments, consistent with the idea of a distribution in threshold stresses.

Below the threshold, no voids or hillocks were observed. However, in the case of Al(Cu), substantial Cu motion occurred, which was studied in detail by measuring precipitate sizes as a function of time and current density. In order to minimize sample to sample variation, all measurements were performed on one particular set of Al(Cu) segments. The precipitates were reversibly formed and dissolved by cycling the current. Precipitate sizes at steady state as well as during growth and dissolution were investigated. The results indicated that a critical supersaturation of Cu of roughly 2 times the solubility is required to form a precipitate. The analysis of the precipitation kinetics showed that interface diffusion along the length of the segment is an important transport path, but that diffusion of Cu atoms into the Al lattice is also important. The value obtained for the effective valence for Cu of -14 falls in the range of previously reported values (-4..-15)[Blech, 1977].

Above the threshold, damage evolution was divided into the three stages: incubation period, constant drift, and saturation. First, the incubation time was characterized. In order to minimize sample to sample variation, a single passivated pure Al segment was used to measure the incubation time to nucleate a particular void. By cycling the current, the void was reversibly formed and closed, and the incubation time could be measured as a function of current density. According to models for electromigration, the time to nucleate a void is attributed to the time to develop a critical tensile stress in the interconnect. Good agreement was obtained between the measured current density dependence and the predicted dependence from the Korhonen model. Additionally, a value for the critical stress for void nucleation was obtained, which was roughly 160 MPa. This is comparable to values from direct stress measurements reported in the literature [Wang et al., 1998].

Drift velocity measurements were performed on both passivated and unpassivated Al segments to elucidate the effect of passivation. Long segments connected on one end to a large reservoir (contact pad) were used, in order to minimize the influence of the segment length. The drift velocities of the passivated and unpassivated segments were found to be the same for current densities varying between 0.01 and 0.3 MA/cm^2. This result suggests that differences reported in reliability between passivated and unpassivated interconnects are not due to different drift velocities, but rather due to a change in the threshold product.

In contrast to long segments of pure Al, Al(Cu) did not have a constant drift velocity. Instead, the drift velocity increased with time, hence it was concluded that Cu slows Al drift in the bamboo lines investigated. The early slow motion period was attributed to the selective depletion of Cu over a critical length. The Cu drift velocity obtained from the measurements is consistent with values reported in the literature [Hu et al., 1993a].

Depletion in passivated segments eventually reaches saturation, which is due to the back-driving force of a compressive stress gradient. Whereas depletion in unpassivated segments only slows down when the length approaches the critical length at the given current density, depletion in passivated segments saturates after relatively small amounts of Al displacement. In the passivated pure Al samples the drift kinetics and final void size were in agreement with predictions from the Korhonen model. However in the Al(Cu) samples, the reduction in Al mobility at the anode end of the interconnect, where the Cu concentration was highest, had to be included to obtain reasonable agreement between model and the data. From the analysis it was concluded that the Al mobility decreases abruptly above a critical Cu concentration of roughly 0.5 times the solubility. This picture is consistent with the finding of an increased threshold product of Al(Cu) and the observation that passivation cracking occurred at some distance from the anode end.

In addition, passivated segments showed a back-flux due to the stress gradient when the current was turned off. From the analysis of this data, a value -2 for the effective valence for pure Al, and $1 \cdot 10^{-14}\,m^2/s$ for the effective diffusivity at 250°C were obtained. As in the case of Cu, it is concluded that the interfaces provide a fast diffusion path for the Al.

7

References

[AEI, EM7] AEI (EM7). High voltage electron microscope.

[Ainslie et al., 1972] Ainslie, N. G., d'Heurle, F. M., and Wells, O. C. (1972). Coating, mechanical constraints, and pressure effects on electromigration. *Appl. Phys. Lett.*, 20 (4)(February 15, 1972):173–174.

[Alexander and Slifkin, 1970] Alexander, W. B. and Slifkin, L. M. (1970). Diffusion of solutes in aluminum and dilute aluminum alloys. *Phys. Rev. B*, 1(8):3274–3282.

[Ames et al., 1970] Ames, I., d'Heurle, F. M., and Horstmann, R. E. (1970). Reduction of electromigration in aluminum films by copper doping. *IBM J. Res. Dev.*, 14(July):461–463.

[Andleigh et al., 1999] Andleigh, V. K., Park, J. Y., and Thompson, C. V. (1999). Interconnect failure mechanism maps for different metallization materials and processes. In *MRS symposium proceedings*, volume 563, pages 59–64.

[Arzt et al., 1994] Arzt, E., Kraft, O., Nix, W. D., and Sanchez, J. E. (1994). Electromigration failure by shape change of voids in bamboo lines. *J. Appl. Phys.*, 76(3):1563–1571.

[Arzt and Nix, 1991] Arzt, E. and Nix, W. D. (1991). A model for the effect of line width and mechanical strength on electromigration failure of interconnects with "near-bamboo" grain structures. *J. Mater. Res.*, 6:731–.

[Arzt and Nix, 1992] Arzt, E. and Nix, W. D. (1992). On void nucleation and growth in metal interconnect lines under electromigration conditions. *Metallurgical Transactions A*, 23 A(7):2007–2013.

[Attardo et al., 1971] Attardo, M. J., Rutledge, R., and Jack, R. C. (1971). Statistical metallurgical model for electromigration failure in aluminum thin film conductors. *J. Appl. Phys.*, 42:4343–4349.

[Besser et al., 1997] Besser, P., Sanchez, J. E., and Kraft, O. (1997). Symposium J Tutorial. In *MRS*, pages 88–126.

[Besser, 1999] Besser, P. R. (1999). Mechanical constraints and stresses in aluminum and copper interconnect lines for 0.18 μm logic technologies. In Kraft, O., editor, *Stress induced phenomena in metallization*, volume 491, pages 229–239, Stuttgart.

[Black, 1967] Black, J. R. (1967). Mass transport of aluminum by momentum exchange with conducting electrons. In *IRPS*, volume 6th, pages 148–159. IEEE.

[Blech, 1976] Blech, I. A. (1976). Electromigration in thin aluminum films on titanium nitride. *J. Appl. Phys.*, 47(4):1203–1208.

[Blech, 1977] Blech, I. A. (1977). Copper electromigration in aluminum. *J. Appl. Phys.*, 48(2):473.

[Blech and Kinsbron, 1975] Blech, I. A. and Kinsbron, E. (1975). Electromigration in thin gold films on molybdenum surfaces. *Thin Solid Films*, 25:327–334.

[Blech and Tai, 1977] Blech, I. A. and Tai, K. L. (1977). Measurement of stress gradients generated by electromigration. *Appl. Phys. Lett.*, 30(8):387–389.

[Camscan, 1993] Camscan (1993). Model CS44. equipped with a ISIS EDX system.

[Carslaw and Jaeger, 1959] Carslaw, H. S. and Jaeger, J. C. (1959). *Conduction of heat in solids*. Oxford university press, 2 edition.

[Chamberlain and Lehoczky, 1977] Chamberlain, M. B. and Lehoczky, S. L. (1977). Lattice and grain boundary diffusion of copper in thin aluminum films. *Thin Solid Films*, 45:189–194.

[Clemens et al., 1997] Clemens, B. M., Nix, W. D., and Gleixner, R. J. (1997). Void nucleation on contaminant patch. *J. Mat. Res*, 12:2038.

[Clement, 1992] Clement, J. J. (1992). Vacancy supersaturation model for electromigration failure under DC and pulsed DC stress. *J. Appl. Phys.*, 71(9):4264–4268.

[Clement and Thompson, 1995] Clement, J. J. and Thompson, C. V. (1995). Modeling electromigration-induced stress evolution in confined metal lines. *J. Appl. Phys.*, 78(2):900–904.

[Colgan and Rodbell, 1994] Colgan, E. G. and Rodbell, K. P. (1994). The role of Cu distribution and Al_2Cu precipiation on the electromigration reliability of submicrometer Al(Cu) lines. *J. Appl. Phys.*, 75(7):3423–3433.

[Copel et al., 1996] Copel, M., Rodbell, K. P., and Tromp, R. M. (1996). Cu segregation at the Al(Cu)/Al_2 O_3 interface. *Appl. Phys. Lett.*, 68(12):1625–1627.

[Dekker, 1997] Dekker, J. P. (1997). *Substitutional electromigration in metals.* Phd, Vrije Universiteit.

[Dekker and Gumbsch, 2000] Dekker, J. P. and Gumbsch, P. (2000). A kinetic model for electromigration in face-centered cubic alloys. *J. Phys. Condens. Matter*, 12:3281–3292.

[d'Heurle and Ames, 1970] d'Heurle, F. and Ames, I. (1970). Electromigration in single-crystal aluminum films. *Appl. Phys. Lett.*, 16:80.

[Doan et al., 1999a] Doan, J. C., Bravman, J. C., Flinn, P. A., and Marieb, T. N. (1999a). Direct measurement of nucleation times and growth rates of electromigration induced voids. In Kraft, O., editor, *Stress induced phenomena in metallization*, volume 491, pages 15–26, Stuttgart.

[Doan et al., 1999b] Doan, J. C., Lee, S. H., Bravman, J. C., Flinn, P. A., and Marieb, T. N. (1999b). Void nucleation on intentionally added defects in Al interconnects. *Appl.Phys.Let.*, 75(5):633–635.

[Doan and Bocquet, 1975] Doan, N. V. and Bocquet, J. L. (1975). *Thin Solid Films*, 25:15.

[Drouin and Hovington, 1997] Drouin, D. and Hovington, P. (1997). Casino, montecarlo simulation of electron trajectory in solids.

[Dwyer et al., 1996] Dwyer, V. M., Kearny, M. J., and Bressloff, P. C. (1996). An integral equation approach to electromigration under arbritrary time-dependent stress. *J. Appl. Phys.*, 80(7):3792–3792.

[Dwyer et al., 1994] Dwyer, V. M., Wang, F. S., and Donaldson, P. (1994). Electromigration failure in a finite conductor with single blocking boundary. *J. Appl. Phys.*, 76(11):7305–7310.

[English and Kinsbron, 1983] English, A. T. and Kinsbron, E. (1983). Electromigration induced failure edge displacement in fine-line aluminum 0.5 wt% copper thin film conductors. *J. Appl. Phys.*, 54(1):268–274.

[Eurotherm, 1998] Eurotherm (1998). Model 2416.

[FEI, 1998] FEI (1998). Model xP 200 with automated grain size analysis.

[Fiks, 1959] Fiks, V. B. (1959). On the mechanism of the mobility of ions in metals. *Sov. Physics Solid State*, 1:14.

[Frost and Ashby, 1982] Frost, H. J. and Ashby, M. F. (1982). *Deformation-mechanism maps*, volume 9.

[Gall, 1998] Gall, M. (1998). Critical length and resistance saturation effects in Al(Cu) interconnects. In *MRS symposium proceedings*, volume 516, pages 231–236.

[Gleixner et al., 1997] Gleixner, R. J., Clemens, B. M., and Nix, W. D. (1997). Void nucleation in passivated interconnect lines: Effects of site geometries, interfaces, and interface flaws. *J.Mater. Res.*, 12(8):2081–2090.

[Gleixner and Nix, 1998] Gleixner, R. J. and Nix, W. D. (1998). Effect of bamboo grain boundaries on the maximum electromigration-induced stress in microelectronic interconnect lines. *J.Appl.Phys.*, 83(7):3595–3599.

[Glickman et al., 1998] Glickman, E., Osipov, N., Ivanov, A., and Nathan, M. (1998). Diffusional creep as a stress relaxation mechanism in electromigration. *J. Appl. Phys.*, 83(1):100–107.

[Grabe and Schreiber, 1983] Grabe, B. and Schreiber, H. U. (1983). Lifetime and drift velocity analysis for electromigration in sputtered al films, multilayers and alloys. *Solid-State Electron.*, 26(10):1023–1032.

[Hemmert and Costa, 1991] Hemmert, R. S. and Costa, M. (1991). Electromigration-induced compressive stresses in encapsulated thin-film conductors. In *IRPS*, pages 64–69. IEEE.

[Herring, 1950] Herring, C. (1950). Diffusional viscosity of a polycrystalline solid. *J. Appl. Phys.*, 21:437.

[Ho and Howard, 1974] Ho, P. S. and Howard, J. K. (1974). Grain-boundary solute electromigration in polycristalline films. *J.Appl.Phys.*, 45(8):3229.

[Hu, 1995] Hu, C. K. (1995). Electromigration failure mechanisms in bamboo-grained Al(Cu) interconnections. *Thin solid films*, 260:124–134.

[Hu et al., 1996] Hu, C. K., Lee, K. Y., Lee, K. L., Cabral, C., Colgan, E. G., and Stanis, C. (1996). Electromigration drift velocity in Al-alloy and Cu-alloy lines. *J. Electrochem. Soc.*, 143(3):1001–1006.

[Hu et al., 1995] Hu, C. K., Rodbell, K. P., Sullivan, T. D., Lee, K. Y., and Bouldin, D. P. (1995). Electromigration and stress-induced voiding in fine Al and Al-alloy thin film lines. *IBM J. Res. Dev.*, 39(4):465–497.

[Hu et al., 1993a] Hu, C. K., Small, M. B., and Ho, P. S. (1993a). Electromigration in Al(Cu) two-level structures: Effect of Cu and kinetics of damage formation. *J. Appl. Phys.*, 74(2):969–978.

[Hu et al., 1993b] Hu, C. K., Small, M. B., Rodbell, K. P., Stanis, C., Blauner, P., and Ho, P. S. (1993b). *Appl. Phys. Lett.*, 62:1023.

[Hultgren et al., 1992] Hultgren, R., Orr, R. L., and Kelley, K. K. (1992). *Selected values of thermodynamic properties of metals and alloys*, volume 2. ASM, Ohio.

[Hummel, 1977] Hummel, R. E. (1977). *Electro- and Thermotransport in Metals and Alloys*. AIME, New York.

[Huntington and Grone, 1961] Huntington, H. B. and Grone, A. R. (1961). Current-induced marker motion in gold wires. *J. Phys. Chem. Solids*, 20:76.

[JEOL35, 1970] JEOL35 (1970). Model 35 c. equipped with Robinson backscatter detector.

[JEOL6400, 1994] JEOL6400 (1994). Model 6400. equipped with a PGT EDX system.

[Joo et al., 1998] Joo, Y. C., Baker, S., and Arzt, E. (1998). Electromigration in single-crystal aluminum lines with fast diffusion paths made by nanoindentation. *Acta. mater.*, 46(6):1969.

[Joo and Thompson, 1997] Joo, Y. C. and Thompson, C. V. (1997). Electromigration-induced transgranular failure mechanisms in single-crystal aluminum interconnects. *J. Appl. Phys.*, 81:6062.

[Kahn and Thompson, 1991] Kahn, H. and Thompson, C. V. (1991). Effect of applied mechanical stress on the electromigration failure times of aluminum interconnects. *Appl. Phys. Lett.*, 59:1308.

[Kang et al., 1996] Kang, S. H., Kim, C., Morris, J. W., and Genin, F. Y. (1996). Effect of post-pattern annealing on the grain structure and reliability of Al-based interconnects. *J.Appl.Phys.*, 79(11):8330–8335.

[Kao et al., 2000] Kao, H. K., Cargill, G. S., and Hu, C. K. (2000). Concentration and stress evolution during electromigration in passivated Al(0.25 at% Cu) conductor lines. In *MRS symposium proceedings*.

[Kaur and Gust, 1990] Kaur, I. and Gust, W. (1990). *Diffusion in solid metals and alloys*, volume III/26 of *Landolt-Börnstein*. Springer.

[Kaur et al., 1989] Kaur, I., Gust, W., and Kozma, L. (1989). *Handbook of grain boundary and interphase boundary diffusion data*. Ziegler, Stuttgart.

[Kawasaki et al., 1998] Kawasaki, H., Gall, M., Jawarani, D., Hernandez, R., and Capasso, C. (1998). Electromigration failure model: its application to W plug and Al-filled vias. *Thin Solid Films*, 320:4551.

[Kim and Morris, 1993] Kim, C. and Morris, J. W. (1993). The mechanism of electromigration failure of narrow Al-2Cu-1Si thin film interconnects. *J. Appl. Phys.*, 73(10):4885–4893.

[Kim et al., 1997] Kim, C. U., Morris, J. W., and Lee, H. M. (1997). Kinetics of electromigration-induced edge drift in Al-Cu thin-film interconnects. *J. Appl. Phys.*, 82(4):1592–1598.

[Korhonen et al., 1993a] Korhonen, M. A., Borgesen, P., Brown, D. D., and Li, C. Y. (1993a). Microstructure based statistical model of electromigration damage in confined line metallizations in the presence of thermally induced stresses. *J. Appl. Phys.*, 74(8):4995–5004.

[Korhonen et al., 1993b] Korhonen, M. A., Borgesen, P., Tu, K. N., and Li, C. Y. (1993b). Stress evolution due to electromigration in confined metal lines. *J. Appl. Phys.*, 73(8):3790–3799.

[Kraft and Arzt, 1998] Kraft, O. and Arzt, E. (1998). Current density and line width effects in electromigration: A new damage based lifetime model. *Acta. mater.*, 46(11):3733–3743.

[Landolt and Börnstein, 1990] Landolt and Börnstein (1990). *Diffusion in Solid Metals and Alloys*, volume III/26. Springer.

[Lemo Elektronik, 1998] Lemo Elektronik, M. (1998). Vakuumdurchführung.

[Li et al., 1998] Li, H., Maex, K., Brijs, B., Conard, T., Vandervorst, W., Baklanov, M., Boullart, W., and Froyen, L. (1998). Segregation of Cu on etched and non-etched Al(Cu) surface. In *MRS symposium proceedings*, volume 516, pages 77–82.

[Liu et al., 1999] Liu, X. Y., Liu, C. L., and Borucki, L. J. (1999). A new investigation of coppers role in enhancing AlCu interconnect electromigration resistance from an atomistic view. *Acta. Mat.*, 47(11):3227–3231.

[Lloyd, 1997] Lloyd, J. R. (1997). Electromigration in thin film conductors. *Semicond. Sci. Technol.*, 12:11771185.

[Lloyd and Kitchin, 1994] Lloyd, J. R. and Kitchin, J. (1994). The finite electromigration boundary value problem. *J. Mater. Res.*, 9(3):563.

[Lloyd and Nakahara, 1977] Lloyd, J. R. and Nakahara, S. (1977). *J. Vac. Sci. and Technol.*, 14(1):655–659.

[Lloyd and Smith, 1983] Lloyd, J. R. and Smith, P. M. (1983). The effect of passivation thickness on the electromigration lifetimes of Al/Cu thin film conductors. *J. Vac. Sci. Tech. A*, 1 (2)(April-June):455–458.

[Marcus and Bower, 1997] Marcus, M. A. and Bower, J. E. (1997). Precipitation of Al_2Cu in blanket Al-Cu films. *J.Appl.Phys.*, 82(8):3821–3827.

[Marieb et al., 1995] Marieb, T., Flinn, P. A., Gardner, D., and Maddan, M. (1995). Observations of electromigration induced void nucleation and growth in polycrystalline and near-bamboo passivated Al lines. *J. Appl. Phys.*, 78(2):1026–1032.

[Massalski, 1990] Massalski, T. B. (1990). *Binary alloy phase diagrams*, volume 1. ASM, 2 edition.

[Microinstruments, 1995] Microinstruments (1995). EM testing system.

[Oates, 1994] Oates, A. S. (1994). Early electromigration failure in submicron width, multilayer Al alloy conductors: sensitivity to stripe length. In *MRS Symposium Proceedings*, volume 338, pages 453–458.

[Oates, 1996a] Oates, A. S. (1996a). Electromigration failure of contacts and vias in sub-micron integrated circuit metallizations. *Microelectron. Reliab.*, 36(8):925–953.

[Oates, 1996b] Oates, A. S. (1996b). Electromigration transport mechanisms in Al thin-film conductors. *J. Appl. Phys.*, 79(1):163–169.

[Penney, 1964] Penney, R. V. (1964). *J. Phys. Chem. Solids*, 25:335.

[Peterson and Rothman, 1970] Peterson, N. L. and Rothman, S. J. (1970). Impurity diffusion in aluminum. *Phys.Rev. B*, 1(8):3264–3273.

[Porter and Easterling, 1992] Porter, D. A. and Easterling, K. E. (1992). *Phase Transformation in metals and alloys.* Chapman & Hall, London, 2 edition.

[Pramanik and Saxena, 1983] Pramanik, D. and Saxena, A. N. (1983). VLSI metallization using aluminum and its alloys. *Solid State Technology*, jan:127.

[Proost et al., 1998] Proost, J., Li, H., Brijs, B., Witvrouw, A., and Maex, K. (1998). Electromigration behaviour of 0.3 μm damascene vs. plasma-etched interconnects: A lifetime and drift analysis. In *IEEE 98 International Interconnect Technology Conference*, pages 110–12, San Francisco. IEEE.

[Proost et al., 2000] Proost, J., Maex, K., and Delaey, L. (2000). Electromigration-induced drift in damascene and plasma-etched AlCu. II. mass transport mechanisms in bamboo interconnects. *J. Appl. Phys.*, 87(1):99–109.

[Reddy et al., 1978] Reddy, K. V., Beniere, F., and Kostopoulos, D. (1978). Electromigration and diffusion of copper in aluminum thin films. *J.Appl.Phys.*, 50(4):2783–2786.

[Riege et al., 1996] Riege, S. P., Prybyla, J. A., and Hunt, A. W. (1996). Influence of microstructure on electromigration dynamics in submicron Al interconnects: Real-time imaging. *Appl. Phys. Lett.*, 69(16):2367–2369.

[Rose et al., 1991] Rose, J. H., Lloyd, J. R., Shepela, A., and Riel, N. (1991). Microstructure of Al-Cu thin film interconnect. In *Annual Meeting, Electron Microscope Society of America*, page 820. EMSA.

[Rosenberg, 1972] Rosenberg, R. (1972). Inhibition of electromigration damage in thin films. *J. Vac. Sci. Technol.*, 9(1):263–270.

[Ross et al., 1989] Ross, C. A., Drewery, J. S., Somekh, R. E., and Evetts, J. E. (1989). The effect of anodiztion on the electromigration drift velocity in aluminum films. *J. Appl. Phys.*, 66(6):2349–2355.

[Schmidt et al., 2000] Schmidt, C., Dekker, J. P., Gumbsch, P., and Arzt, E. (2000). An atomistic mechanism for the retardation of electromigration in Al-Cu conductor lines. *to be published*.

[Shatzkes and Lloyd, 1986] Shatzkes, M. and Lloyd, J. R. (1986). A model for conductor failure considering diffusion concurrently with electromigration resulting in a current exponent of 2. *J. Appl. Phys.*, 59 (11)(June 1, 1986):3890–3893.

[Shaw et al., 1995] Shaw, T. M., Hu, C. K., Lee, K. Y., and Rosenberg, R. (1995). The microstructural stability of Al(Cu) lines during electromigration. *Appl. Phys. Lett.*, 67(16):2296–2298.

[Shaw et al., 1996] Shaw, T. M., Hu, C. K., Lee, K. Y., and Rosenberg, R. (1996). Copper migration and precipitate dissolution in aluminium/copper lines during electromigration testing. In *MRS symposium proceedings*, volume 428, pages 187–199.

[Shih and Greer, 1995] Shih, W. C. and Greer, A. L. (1995). In *MRS symposium proceedings*, volume 356, page 417.

[Shine and d'Heurle, 1971] Shine, M. C. and d'Heurle, F. (1971). Activation energy for electromigration in aluminum films alloyed with copper. *IBM J. Res. Dev.*, 15:378–383.

[Sorbello et al., 1982] Sorbello, R. S., Lodder, A., and Hoving, S. J. (1982). Finite-cluster description of electromigration. *Phys. Rev. B*, 25(10):6178–87.

[Spitzer and Schwartz, 1969] Spitzer, S. and Schwartz, S. (1969). The effects of dielectric overcoating on electromigration in aluminum interconnctions. *IEEE Trans. E.D.*, ED-16(4):348–350.

[Spolenak et al., 1998a] Spolenak, R., Heiland, B., Witt, C., Keller, R. M., Müllner, P., and Arzt, E. (1998a). Zielpräparation von TEM-proben mit fokussierten ionenstrahl (FIB). In Petzow, G., editor, *Internationale Metallographie Tagung*, volume 10 of *Fortschritte in der Metallographie*, pages 229–237, Leoben.

[Spolenak et al., 1998b] Spolenak, R., Kraft, O., and Arzt, E. (1998b). Effects of alloying elements on electromigration. *Microelectronics and Reliability*, 38(6-8):1015–1020.

[Spolenak et al., 1997] Spolenak, R., Kraft, O., Nix, W. D., and Arzt, E. (1997). Alloying effects in electromigration: Modeling and experiments. In *Stress induced Phenomena in Metallization*, volume 418, page 147. Americ. Inst. Phys.

[Srikar and Thompson, 1998] Srikar, V. T. and Thompson, C. V. (1998). Diffusion and electromigration of Cu in single crystal Al interconnects. In *MRS symposium proceedings*, volume 516, pages 71–75.

[Straub, 2000] Straub, A. (2000). *Factors influencing the critical product in electromigration.* Phd.

[Theiss and Prybyla, 1996] Theiss, S. K. and Prybyla, J. A. (1996). In situ study of Al_2Cu precipitate evolution during electromigration in submicron Al interconnects. In *MRS symposium proceedings*, volume 428, pages 207–212.

[Todorov et al., 2000] Todorov, T. N., Hoekstra, J., and Sutton, A. P. (2000). Current-induced forces in atomic-sclae conductors. *Phil. Mag.*, 80(3):421–455.

[Tomizuka and Emerick, 1965] Tomizuka, T. and Emerick, R. M. (1965). *Physics of solids at high pressures.* Academic, New York.

[Tu, 1992] Tu, K. N. (1992). Electromigration in stressed thin films. *Physical Review B*, 45(3):1409–1413.

[van Eck et al., 1995] van Eck, J., Dekker, J. P., and Lodder, A. (1995). Electromigration of substitutional impurities in metals: Theory and application in Al and Cu. *Phys. Rev. B*, 12:8794–8800.

[van Eck and Lodder, 1994] van Eck, J. and Lodder, A. (1994). *Def. Diff. Forum*, 115:1.

[Volin and Balluffi, 1968] Volin, T. E. and Balluffi, S. J. (1968). *Phys. Status Solidi*, 25:163.

[Walton et al., 1992] Walton, D. T., Frost, H. J., and V., T. C. (1992). Development of near-bamboo and bamboo microstructures in thin-film strips. *Appl. Phys. Lett.*, 61:40.

[Wang et al., 1998] Wang, P. C., Cargill, G. S., Noyan, I. C., and Hu, C. K. (1998). Electromigration-induced stress in aluminum conductor lines measured by x-ray microdiffraction. *Appl. Phys. Lett.*, 72(11):1296.

[Witt and Volkert, 1997] Witt, C. and Volkert, C. A. (1997). Quanitative measure of EM-induced drift in sub-micron Al lines. In *MRS symposium proceedings*, volume 516, pages 33–38.

[Wolfram, 1999] Wolfram (1999). Mathematica, version 4.

Appendix A

Electromigration test stage

A.1 Chip carrier

After dicing test chips (8×8 mm) from the wafer, they were glued into a chip carrier by using a one component silver paint (Plano). This suspension was metal powder filled, hence electrically conducting and of high thermal conductivity. It delivered the required mechanical support for the samples, even after a several thermal cycles between room temperature and the testing temperature (250°C). In addition, the sample could be removed without breaking it. After the solvent is evaporated, the paint was vacuum compatible.

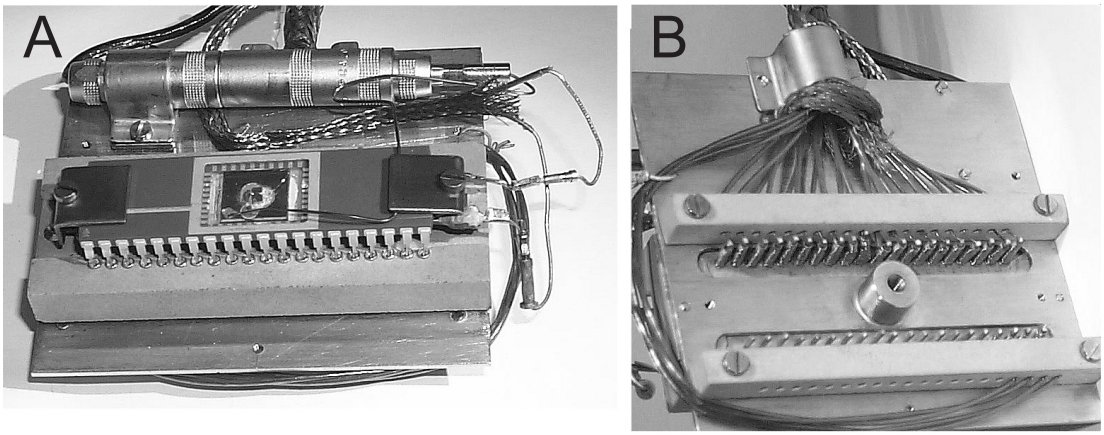

Figure A.1: Testing stage. The top view shows the chip carrier with a sample plugged into the ceramic socket (A). The rear view shows the wiring of the 40 leads (B).

The chip carrier used was a ceramic 40 lead side braze package (DIL format) which

was high temperature and vacuum compatible (see Figure A.1). The number of leads was sufficient to connect 16 test structures (four point measurement), if they are connected in series in 2 circuits. The package had no pins at the bottom face, so that a heating plate could be mounted under it. The chip cavity size (13.3 mm by 10.2 mm) was sufficient to accommodate the sample. The gold plated bottom of the cavity was connected to ground, in order to avoid sample charging effects.

To accommodate the 40 lead chip carrier mechanically, a machinable ceramic (Stenan, Hoechst) was chosen, because its high temperature stability and vacuum compatibility. After machining, the ceramic socket needed to be sintered at 1320°C, in order to make it high vacuum compatible and to achieve the final strength. After the sintering process the material has a tensile strength of 40 MPa making it suitable for this application. The ceramic socket rests on two stand-offs, which were machined into the ceramic. This was to minimize the contact area to the underlying metallic stage in order to maximize thermal isolation.

A.2 Temperature control

The heating element was constructed to fit between the chip carrier and the ceramic socket. It was assembled from two thin stainless steel plates, between which the heating wire is embedded (see drawing in Figure A.3). Stainless steel can be heated up to at least 400°C without compromising the vacuum. This design was chosen in order to keep the height of the heating element below 2 mm while obtaining sufficient heating wire length (160 mm). At a resistance of 12.5 Ω/m, the element had a maximum power of 15-20 W, sufficient to achieve a temperature of 400°C. The element is directly attached to the chip carrier by means of two clamps. Additionally, a small amount of silver paint is put between the chip carrier and the heater to maximize thermal contact. The heater is not in mechanical contact with the socket, again to maximize thermal isolation. The heating wire itself is a shielded high resistance wire (Philips) with a ceramic isolation between the wire and the shielding. The two steel plates of the heater have semi spherical-shaped grooves to fit the wire into them. This delivers best thermal contact to the plates. The two ends of the heater wire were stripped of their shielding and isolation and connected to crimp connectors by spot welding. Cu wires of 0.6 mm diameter were welded onto pins, which fit into the crimps, so that the connection could be unplugged. This solution provides cold ends for the heating wire in order to localize the heat generation to the heating plate.

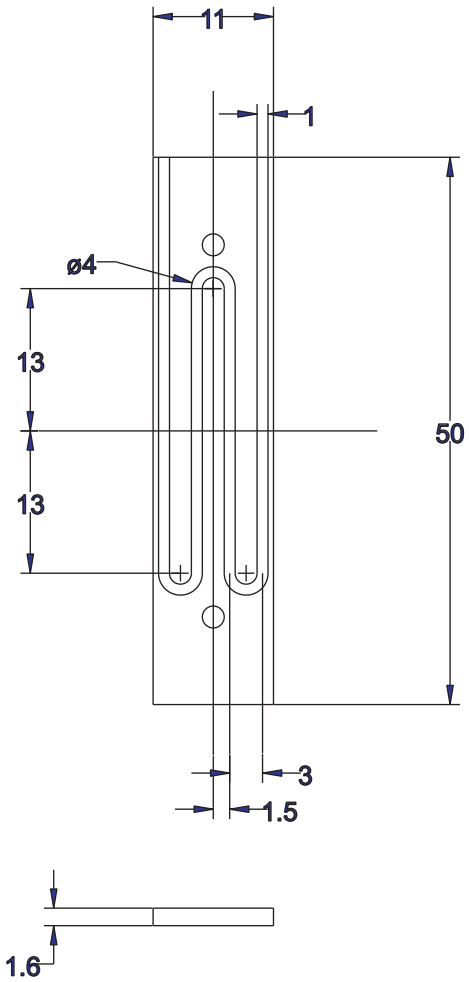

Figure A.2: Top view of the heating element. The heating wire is embedded between two steel plates.

The Temperature was measured by a shielded K-type NiCr thermocouple of 0.5 mm diameter. Shielding is favorable to protect the temperature control circuit from effects of electromagnetic noise and it provides a good mechanical support. The thermocouple wires were electrically isolated from the shielding. The tip of the thermocouple (the final 20 mm) is thinned to a diameter of 0.25 mm, which was attached to the sample. The diameter was chosen in order to make the thermocouple as small a heat sink as possible. The location of temperature measurement is also important. Typically, the temperature of the hot plate underneath a sample is measured. With this stage, it is measured *directly on the chip surface*, next to the testing structures to avoid effects of temperature gradients. If the chip sample was heated by Joule heating (due to the

testing current), it could be detected with this arrangement. The thermocouple was connected to plugs for quick sample change.

The thermocouple is connected to the input of a temperature controller [Eurotherm, 1998], which delivers as output a continuous controlling voltage between 0-10 V. The advantage of a continuous output versus an on/off mode output, where the controller basically switches a relay, is better temperature stability and less electromagnetic noise. This output voltage controls a DC power supply. The use of DC for the heater is preferable compared to AC, because AC fields can generate deflection of the electron beam in the SEM, which would deteriorate the image. The maximum output power of the power supply (100 %) was limited to 20 W, which was sufficient to heat the sample within 10 min up to 300°C. The power required for holding the sample at a testing temperature of 250°C was measured to be 10-12 W.

Above the chip carrier is a metallic radiation shield. One purpose is the protection of sensitive parts of the microscope, in particular the detectors, against heating. Another purpose is an additional electromagnetic shielding of the sample. The construction as a whole was found to meet the requirements of thermal isolation: after a test run at 250°C for several days, all parts inside the microscope chamber had a temperature of less than roughly 40-50°C immediately after turning the heater off and venting the chamber. The socket, the plug for the thermocouple, and the measurement cables were mounted on a steel plate of (70 x 70) mm^2, as shown in the drawing A.3.

A.3 Wiring

Electrical connections between bonding pads on the sample and the gold plated contacts of the package were established by wire bonding. Two possible types of wire bonding were considered: ball bonding and wedge bonding. For ball bonding a fine (20 - 60 μm diameter) gold wire is led through a ceramic capillary. The end of the wire is melted by a electrical discharge forming a ball (roughly 100 - 200 μm diameter) by surface tension. The ball is pressed onto the bonding area and simultaneously ultrasound is transmitted into the capillary tip. The resulting adhesion depends on the surface condition of the sample as well as on the duration of ultrasonic energy transmission and mechanical force. Ball bonding is improved by heating the sample to 150-200°C. After the first bond, the tip was retracted, with the wire still inserted. When the position for the second bond was reached, the wire with the tip was pressed

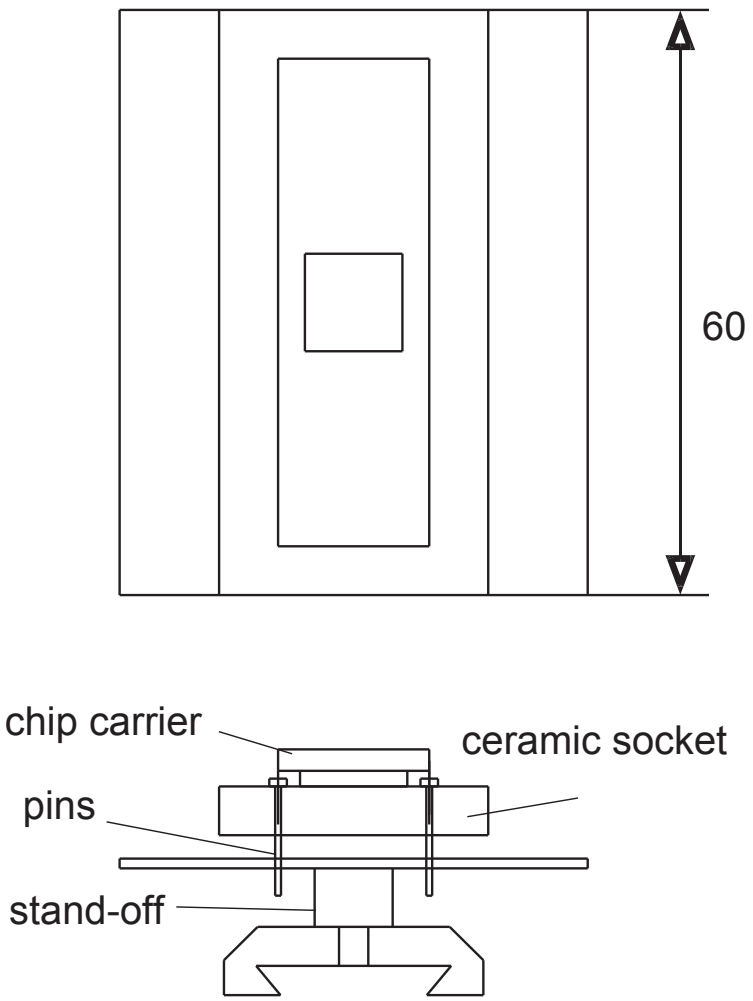

Figure A.3: Side and top view of the electromigration testing stage including the chip carrier and the pins connecting to the carrier.

on the second contact area (without ball) and ultrasonic energy is released again.

The principle of wedge bonding is quite similar, but the wire is guided through a pinhole of a metallic tip. The end of the tip has a wedge form, by which the wire is pressed onto the contact area. Again, ultrasound is used to deliver the required energy to generate good adhesion. Wedge bonding is performed at room temperature and can use various wire materials. Al, Au, and Pd wires have been used successfully on the films investigated. It was found that Pd wires have the best adhesion and require the lowest amount of mechanical force and ultrasonic energy.

The ball wire bonder (Kulicke and Soffa) does not produce consistent results. For example, often a ball is not formed at all. The height to where the wire is pulled after the first bond (loop), could not be adjusted, which is important when crossing wires. Therefore, a Al wire wedge bonder has been used. Using Al wire is advantageous when bonding to samples without diffusion barriers, because in this case contamination from the bonding wire is avoided.

In the socket for the chip carrier, gold coated pins were used, which have a square cross-section at the lower end. Contact to these pins was made using wire wrapping. This was performed manually using 0.3 mm Cu-wire. The wrapped wire was then spot welded onto the pins, in order to supply a good electrical contact and a mechanical support for the pins in the vertical direction. In this way, no glue had to be used to hold the pins to the socket, which is desirable to maintain a good vacuum. Next, the first 20 cm of the wires were protected additionally with capton tubes (0.6 mm diameter). The purpose was to protect the cables mechanically and to provide electrical isolation. Adjacent wires were then combined in pairs and twisted together. This suppresses magnetic induction very effectively, because the loop area is largely reduced. These twisted pairs were used to measure the voltages of the testing structures. To feed the current into the test circuit a separate twisted pair was used. All wires were bundled together and covered by a braided shielding made from stainless steel.

All wiring is fed out to the airside of the chamber by removable feedtroughs [Lemo Elektronik, 1998], which are screwed into a custom made flange and sealed by O-rings. On the airside, twisted pair cables were used as well with metallic shielding. The cables terminate in a metallic (HF-shielding) box, where every twisted pair is connected to a single 2-pole plug, which allowed the connection scheme for each experiment to be selected.

A.4 Measurement set-up

For measuring the voltages, a precision multimeter (Keithley 2001) was used, which was equipped with a 10-channel multiplexer board. This multiplexer is relay-based, therefore the 10 channels can be scanned within roughly a second. There are also higher speed (solid state) multiplexer boards available, but they have factor 5 -10 higher contact potentials than the relay switched systems. For long term measurements, as in the present application, this speed is sufficiently high. The voltmeter possessed a resolution of 1 μV when operated in the 20 V range.

The power supply used was a high precision constant current source (Keithley 2400). This source could be programmed in minimum current steps of 50 pA at an accuracy of 0.035 %. Such high accuracy is particular important when testing submicron wide lines at very small absolute testing currents. As an example, in a half micron wide line made from a 400 nm thick film, a current of only 0.2 mA gives a current density of $1 \cdot 10^5\,\mathrm{A/cm^2}$. The current was measured using an internal meter of the power supply.

A common problem in measuring DC voltage, is AC noise, which can lead to serious errors in the measurement. The AC part in the signal should therefore be suppressed whenever possible. First, all wiring was shielded carefully as described above in order to minimize electromagnetic field-induced noise. Care was taken to avoid any ground loops with the shielding, because ground loops could produce large noise levels in the measurement circuitry. The signal was monitored with an oscilloscope after setting up the shield connections to make sure that no parasitic oscillations were present. Another source of noise is the power supply itself, which was measured to be 10 mV peak to peak. Finally, the DC voltage measurement was smoothed by using a filter. A hardware averaging filter was used, which performs and averages 20 single shot measurements (within roughly 500 ms).

Another threat to accurate voltage/resistance measurements is a DC-offset, which is generated by thermo-potentials at the intersections of different metals in the electrical path. There are different ways to handle such parasitic voltages: since any thermovoltage has a certain sign, whereas the sign of the voltage drop across a resistance depends on the current direction, the thermovoltage can be filtered out by switching the current direction from forward to backwards and averaging the two measured values. This operation is not suitable for constant current electromigration tests where a fixed current direction is required. Instead, the offset voltage was measured without any applied current, which was then subtracted from the measured value during the electromigration test.

Appendix B

Computer simulations

B.1 Simulation of failure site distribution

In real interconnects, the failure sites are statistically distributed both in their position and critical stress. In order to simulate damage in large sample distributions, a large number of damage sites are required for input into the model. Although obtaining this data experimentally would provide the most realistic failure site distributions, such work is time consuming. Therefore, the damage site distribution was simulated numerically. The simulation is limited to a one dimensional distribution of damage sites, which is applicable to deep sub-micron lines, where only one failure (void or hillock) occurs over the cross-section of the line.

The model line considered here consists of a one dimensional row of points x_i having a separation distance d_i. The spacings d_i were either assumed to be constant, or were from a lognormal distribution with a median spacing of μ_x and a standard deviation δ_x. The geometry of the model is schematically shown in Figure B.1.

Each point x_i was then attributed with a critical stress $\sigma_i(x_i)$. These critical stresses are obtained by sampling a normal distribution with a median threshold stress $\bar{\sigma}_C$ and a standard deviation of δ_σ. The total length of the simulated line was equal to half the physical segment length, since tensile stresses are only present in half of the segment.

After setting up the critical stresses at each point x_i, the threshold stress $\sigma_i(x_i)$ was compared to the actual (electromigration-induced) stress profile along the length of the segment $\sigma(x)$, which was assumed to be linear (equation 5.5). The number of points N, which had a lower threshold stress than the electromigration-induced stress was determined. Since these points represent a subset of the population of all

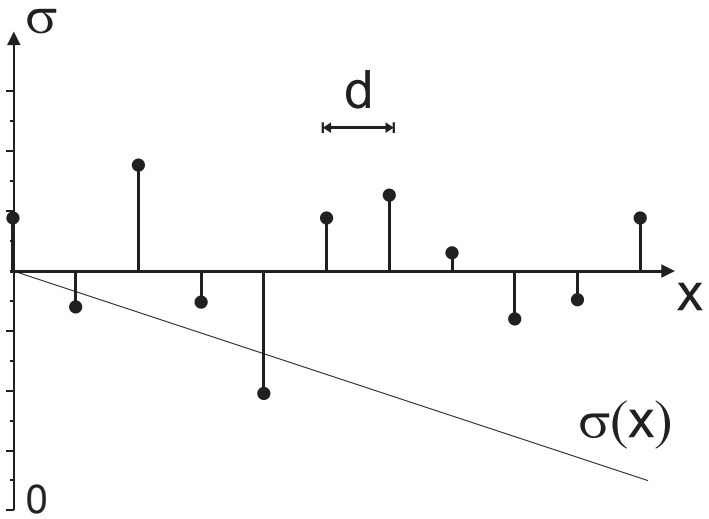

Figure B.1: Geometry for simulation: The spacings d_i are either constant, or obtained by sampling a lognormal distribution. The threshold stresses are obtained by sampling a normal distribution.

threshold stresses, the deviation can be calculated by

$$\delta = \frac{\delta_\sigma}{\sqrt{N}} \, . \tag{B.1}$$

This procedure was performed for 1000 segments of each length between 20 and 220 μm in steps of 20 μm. The resultant mean relative deviations ($\delta/\bar{\sigma}_C$ in %) determined from these simulations are shown in Figure B.2 as a function of segment length.

The plot shows that the simulation agrees well with the analytical solution (equation 5.8) for the case of constant spacing $d_i = 0.6\,\mu$m. For comparison, the simulation result for the case of lognormally distributed spacings is also shown. For segment lengths longer than roughly 40 μm an increased deviation for variable spacing was found. With variable spacings from the lognormal distribution the number of larger spacings than the mean spacing μ_x is increased, therefore the total number of possible failure sites in decreased, which leads to the increased deviation.

In summary, the introduction of a distribution of critical stresses, instead of a fixed threshold stress as in the classical Blech-Herring formulation, generates a segment length dependent distribution of threshold stresses and subsequently critical products. The introduction of variable distances between failure sites does not alter the result significantly.

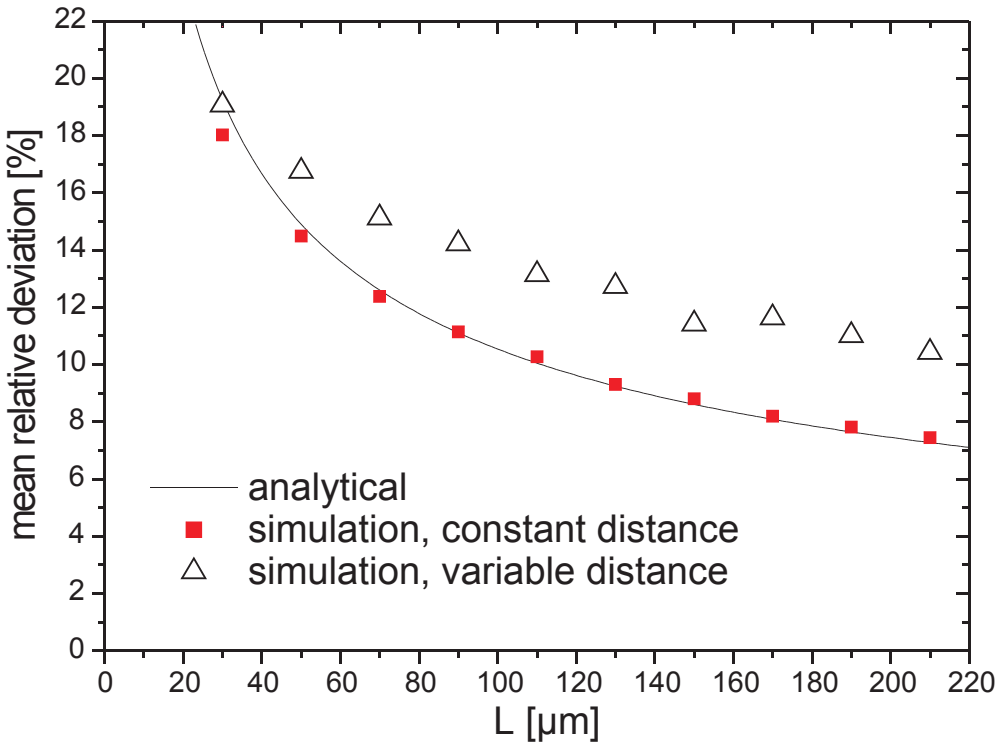

Figure B.2: Result of simulations: The case of constant spacing agrees well with the analytical solution (eq. 5.8), whereas the case of variable spacing differs increasingly with increasing segment length. The spacing was either constant $\mu_x = 0.6\,\mu$m or sampled from the lognormal distribution with a median spacing of $0.6\,\mu$m and a standard deviation of $\delta_x = 0.5$. $\bar{\sigma}_C = 200\,$MPa and $\delta_\sigma = 20\,$MPa.

B.2 Gleixner/Nix model of stresses in bamboo segments

The geometry of the Gleixner/Nix model is illustrated in Figure B.3. An important feature of this model is that it accounts for the 2D structure of lines, such that sidewall and grain boundary diffusion is allowed to take place and matter is allowed to be deposited along interfaces and grain boundaries. An effective stiffness for grain boundaries was introduced that can be used to connect the average thickening of each boundary (grains are treated as linear elastic) with the steady state stress distribution. By assuming mass conservation, the authors obtained a set of equations, which permit the calculation of steady state stress distribution for a given line geometry and grain structure. For more details see reference [Gleixner and Nix, 1998].

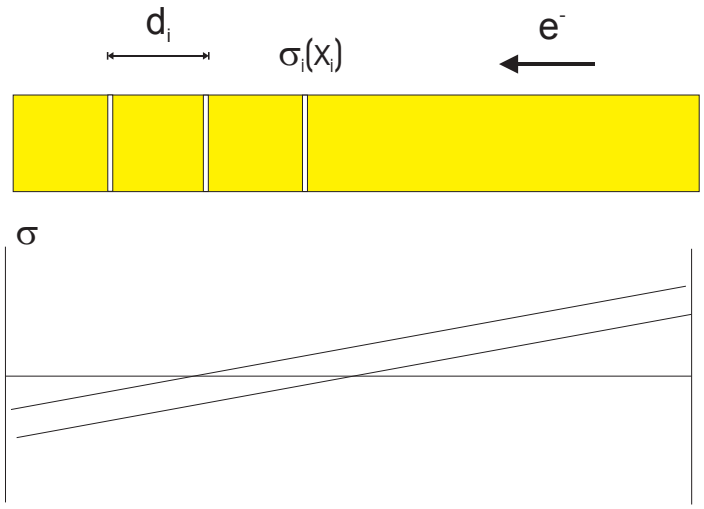

Figure B.3: Gleixner/Nix model describing steady state mechanical stresses in bamboo segments. Due to an asymmetric distribution of grain boundaries the maximum stress in the segment is increased.

The authors used this model to simulate the variation in maximum stress as a function of line length and found it to increase as the length decreases. The range of investigated geometries did not match our segments, therefore their simulation was performed again for our sample geometries. For each length, 1000 interconnect microstructures were generated and the set of equations was solved for each. Grain sizes were obtained from sampling a log-normal distribution using a pseudo-random generator [Wolfram, 1999]. The result is shown in Figure B.4. Essentially, the expected variation due to asymmetric grain boundary distribution along an interconnect segment of length L is not significant in the L range that was investigated experimentally.

It is worth mentioning that for the simulation, a grain size of $1\,\mu$m was used. Gleixner showed that the variation in maximum stress is only weakly dependent on the median grain size as well as the width of grain size distribution. Even increasing the simulated grain size to $10\,\mu$m did not alter much the resulting stress variation. Also, using a bimodal grain size distribution did not modify the result significantly.

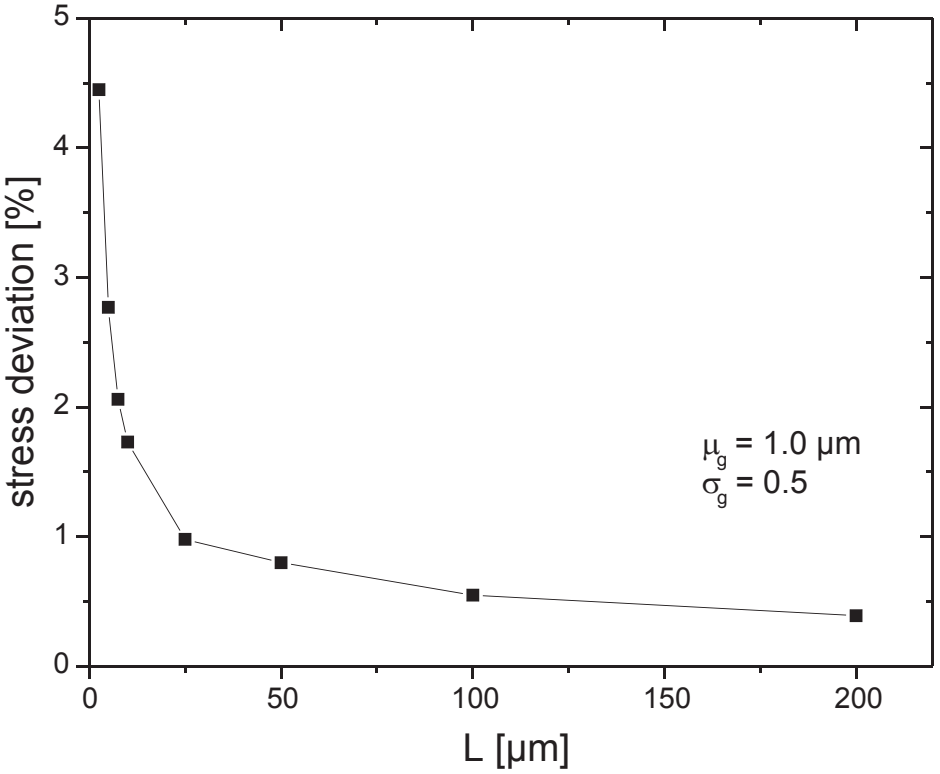

Figure B.4: Variation of maximum steady state stress as a function of segment length. A median grain size of 1.0 μm with a lognormal standard deviation of 0.5 was used for this simulation.

Appendix C

List of symbols and abbreviations

F	electromigration driving force
Z^*	effective charge number Al
Z^*_{Cu}	effective charge number Cu
j	current density
j_c	critical current density
ρ	resistivity
R	resistance
n	current density exponent
γ	electromigration-induced stress gradient
G	average threshold stress gradient
k	Boltzmanns constant
T	absolute temperature
E_a	activation energy
γ_{Al}	free surface energy Al
e	electron charge
A	constant
J	atomic flux
J	Cu flux
J_v	vacancy flux
v	drift velocity
v_0	drift velocity before turning current off
v^0_{Al}	drift velocity pure Al
$v_{Al(Cu)}$	drift velocity alloy
v_{Cu}	drift velocity Cu
c	atomic concentration
c	copper concentration
c_v	vacancy concentration
c_s	solubility concentration
c_c	critical concentration

c_0 ..... initial Cu concentration
c_p ..... precipitate Cu concentration
D ..... effective diffusivity Al
D_{Cu} ..... effective diffusivity Cu
D_l ..... lattice diffusivity Al
D_s ..... metal/sidewall interface diffusivity
D_i ..... metal/shunt layer interface diffusivity
D_{GB} ..... Grain boundary diffusivity
$\bar{D}$ ..... effective diffusivity
D_d ..... dislocation pipe diffusivity
D_a ..... diffusivity at zero stress
κ ... normalized diffusivity in Korhonen model
δ_i ..... interface thickness
ρ_d ..... dislocation density
A_d ..... dislocation cross-section area
σ_h ..... hydrostatic stress
σ ..... hydrostatic stress
σ_c ..... critical stress
$\bar{\sigma}_c$ ..... mean critical stress
σ_L ..... lower bound of critical stress window
σ_{em} ..... stress due to electromigration
σ_T ..... stress due to thermal mismatch
σ^* ..... critical stress for void nucleation
B ..... effective modulus
N ..... number of potential failure sites
P ..... failure probability
Ω_A ..... activation volume
Ω ..... atomic volume
V ..... void volume
V_{em} ..... void volume due to electromigration
V_T void volume due to thermal stress relaxation
L ..... segment length
L_{eff} ..... effective segment length
l ..... diffusion length
ΔL ..... precipitate length
L_{Cu} ..... Cu depleted length
L_c ..... critical length
$(jL)_c$ ..... threshold product
$(jL)^{ppt}$ ... critical product for precipitate nucleation
Δt ..... change in thickness
x ..... position along length of segment
d ..... failure site distance

δ	standard deviation threshold stress
R	radius
Θ_c	wetting angle
t	time
t_{50}	median time to failure
t_{inc}	incubation time
EM	electromigration
TTF	time to failure
FIB	focused ion beam
TEM	transmission electro microscope
SEM	scanning electron microscope
EDX	energy dispersive analysis of X-rays
AR	aspect ratio